Title	All-optical signal processing using semiconductor optical amplifiers for next generation optical networks
Authors	Power, Mark J.
Publication date	2014
Original Citation	Power, M. J. 2014. All-optical signal processing using semiconductor optical amplifiers for next generation optical networks. PhD Thesis, University College Cork.
Type of publication	Doctoral thesis
Rights	© 2014, Mark J. Power. - http://creativecommons.org/licenses/by-nc-nd/3.0/
Download date	2025-08-26 21:00:43
Item downloaded from	https://hdl.handle.net/10468/1796

All-Optical Signal Processing using Semiconductor Optical Amplifiers for Next Generation Optical Networks

Mark John Power
BEEE

National University of Ireland, Cork

Department of Electrical & Electronic Engineering

Tyndall National Institute

Thesis submitted for the degree of Doctor of Philosophy

July 2014

Supervisors: Dr. Robert Manning
Dr. William Wright
Head of Department: Professor Nabeel A. Riza

Table of Contents

I, Mark John Power, certify that work contained within this thesis is my own and that I have not obtained a degree in this university or elsewhere based on the work submitted in this thesis.

_____

Mark J. Power

Acknowledgements

First and foremost I would like to thank my supervisor Dr. Robert Manning for providing me with endless tutelage, support and mentoring throughout the course of my PhD. I could not have asked for a more patient and experienced leader and I wish him well in his coming retirement. I would also like to thank my co-supervisor Dr. William Wright for his helpful feedback and support during the course of this work.

I must extend my sincerest gratitude to Dr. Roderick Webb who provided me with excellent assistance; in understanding the theoretical aspects of this work, in devising methods for overcoming experimental hurdles, for developing the SOA numerical model used in this thesis, and for contributing simulation results.

I would also like to thank Dr. Fatima Garcia-Gunning for her enormous support, advice, and also her contribution to the work documented in this thesis.

Among my colleagues, past and present, I would like to extend special thanks to Dr. James Dailey for his guidance, advice, and for his contribution to the research presented in this thesis. I would also like to thank the various former and current members of the Photonics Systems Group. This includes but is not limited to: Martina Connolly, Dr. Naoise MacSuibhne, Dr. Cleitus Anthony, Dr. Ciaran Cleary, Simon Schneider, Dr. Stylianos Sygletos, and Professor Paul Townsend for their assistance, advice, and collaboration.

Abstract

This thesis details an experimental and simulation investigation of some novel all-optical signal processing techniques for future optical communication networks. These all-optical techniques include modulation format conversion, phase discrimination and clock recovery. The methods detailed in this thesis use the nonlinearities associated with semiconductor optical amplifiers (SOA) to manipulate signals in the optical domain.

Chapter 1 provides an introduction into the work detailed in this thesis, discusses the increased demand for capacity in today's optical fibre networks and finally explains why all-optical signal processing may be of interest for future optical networks. Chapter 2 discusses the relevant background information required to fully understand the all-optical techniques demonstrated in this thesis. Chapter 3 details some pump-probe measurement techniques used to calculate the gain and phase recovery times of a long SOA. A remarkably fast gain recovery is observed and the wavelength dependent nature of this recovery is investigated. Chapter 4 discusses the experimental demonstration of an all-optical modulation conversion technique which can convert on-off- keyed data into either duobinary or alternative mark inversion. In Chapter 5 a novel phase sensitive frequency conversion scheme capable of extracting the two orthogonal components of a quadrature phase modulated signal into two separate frequencies is demonstrated. Chapter 6 investigates a novel all-optical clock recovery technique for phase modulated optical orthogonal frequency division multiplexing superchannels and finally Chapter 7 provides a brief conclusion.

List of Abbreviations

3R	Reshaping, Retiming, and Reamplification
ADC	Analogue-to-Digital Converter
AM	Amplitude Modulation
AMI	Alternate Mark Inversion
AMZI	Asymmetrical Mach-Zehnder Interferometer
ASE	Amplified Spontaneous Emission
BER	Bit Error Rate
BPF	Band Pass Filter
BPSK	Binary Phase Shift Keying
CIP	Centre Integrated Photonics
CMOS	Complementary Metal–Oxide–Semiconductor
CW	Continuous Wave
DB	Duobinary
DBPSK	Differential Binary Phase Shift Keying
DBS	De Bruijn Sequence
DC	Direct Current
DI	Delay Interferometer
DOWC	Dual Output Wavelength Converter
DPSK	Differential Phase Shift Keying
DSO	Digital Sampling Oscilloscope
DSP	Digital Signal Processing
E/O	Electronic-to-Optical
EDFA	Erbium-Doped Fibre Amplifier
FSR	Free Spectral Range
FWM	Four-Wave Mixing
GVD	Group Velocity Dispersion
I	In-Phase
IQ	In-Phase / Quadrature
ITU	International Telegraph Union
MQW	Multiple Quantum Well
MZI	Mach-Zehnder Interferometer

MZM	Mach-Zehnder Modulator
NL	Non-Linear
NRZ	Non Return-to-Zero
O/E	Optical-to-Electronic
OEO	Optical-Electronic-Optical
OFDM	Orthogonal Frequency Division Multiplexing
OOK	On-Off Keying
OSA	Optical Spectrum Analyser
OSNR	Optical Signal-to-Noise Ratio
OSO	Optical Sampling Oscilloscope
PBS	Polarisation Beam Splitter
PC	Polarisation Controller
PM	Phase Modulation
PMD	Polarisation Mode Dispersion
PN	P-type / N-type
PON	Passive Optical Network
PRBS	Pseudo-Random Binary Sequence
PRZ	Pseudo Return-to-Zero
PSK	Phase Shift Keying
Q	Quadrature
QAM	Quadrature Amplitude Modulation
QD	Quantum Dot
QPSK	Quadrature Phase Shift Keying
RF	Radio Frequency
RMS	Root Mean Square
RZ	Return-to-Zero
SGM	Self-Gain Modulation
SMF	Single-Mode Fibre
SMSR	Side Mode Suppression Ratio
SNR	Signal-to-Noise Ratio
SOA	Semiconductor Optical Amplifier
SPM	Self-Phase Modulation
TE	Transverse Electric
TM	Transverse Magnetic

UNI	Ultrafast Nonlinear Interferometer
VOA	Variable Optical Attenuator
WDM	Wavelength Division Multiplexing
WGN	White Gaussian Noise
WSS	Wavelength Selective Switch
XGM	Cross-Gain Modulation
XOR	Exclusive OR
XPM	Cross-Phase Modulation

1.

Introduction

A communication system transmits information from one place to the other using some form of carrier such as an electromagnetic wave. Optical communication where light is used to transmit information has been used for centuries, if we consider it in the broader sense, such as the use of beacon bonfires and smoke signals. Communication has always been an integral part of human civilisation and in recent decades it has had a greater influence, particularly with the rise of long distance communication and the birth of the internet. Modern optical communication system, commonly use electromagnetic waves with high carrier frequencies ($\sim$ 100 THz) that have been encoded with digital information and is then guided by an optical waveguide, to transmit information [1]. These fibre-optic systems have come to dominate the communication industry due to many important factors including the development of low cost optical sources such as semiconductor lasers, the creation of the erbium-doped fibre amplifier (EDFA) which provide a means of amplifying multiple optical channels simultaneously [2], and the reduction in optical fibre loss allowing for greater reach before amplification is required. Since the deployment of these fibre-optic communication systems through the 1980s they have revolutionised the telecommunications field and also led to the "information age" which occurred during the 1990s [1].

1.1 Capacity

The amount of information that a system can transmit for a given bandwidth is referred to as the capacity of the system and was first defined by Claude Shannon as [3]:

$$C = B \log \left(1 + \frac{S}{N} \right) \qquad (1\text{-}1)$$

where C is the capacity measured in bits/s, B is the bandwidth in Hz, S is the signal noise in watts, and N is the noise power in watts. As can be seen the capacity network is dependent on the bandwidth available as well as the signal-to-noise ratio of the transmitted signal.

One advantage of fibre-optic communication systems over wireless or coaxial communication networks is the greater capacity and reach. Fibre optical communication systems can transmit information at Tbits/s of information on a single channel due to their high carrier frequency and large transmission bandwidth [4], and extend thousands of kilometres due to the relatively low loss of fibre . In recent years the rise of videos streaming and the increase in the number of mobile communication devices has led to a continued exponential increase in capacity demand of the world's fibre-optical networks. This can be seen in Fig. 1.1 below where the global IP traffic per month is shown for the past year and includes a growth forecast until 2018.
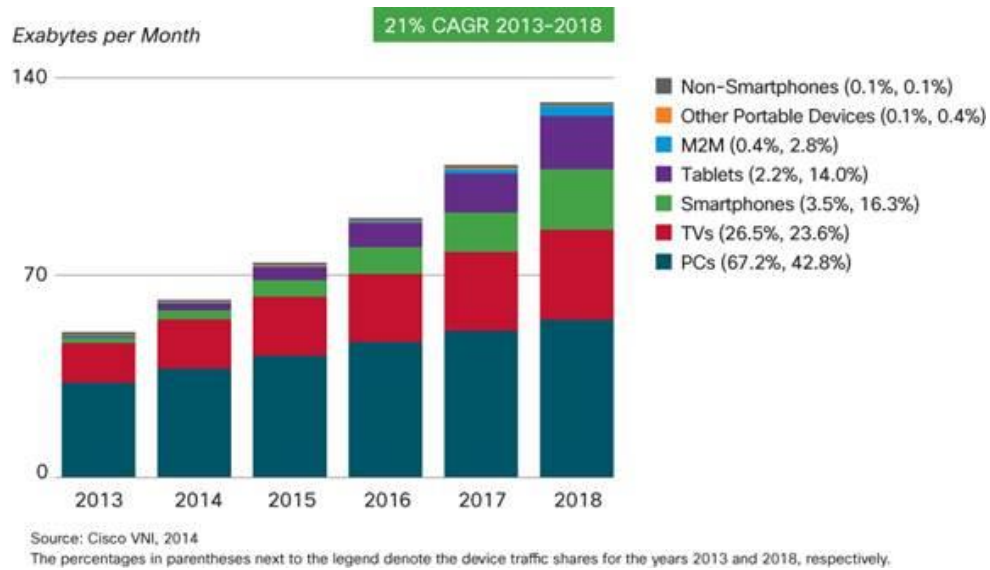
Fig. 1.1 - Cisco global IP traffic growth [5].

Although large the bandwidth of optical fibre is limited, so increasing the bandwidth continuously to provide more capacity is not possible. Many pieces of equipment vital to optical communications, such as EDFAs, also have wavelength limitations which further limit the available bandwidth. As such increasing the capacity of optical fibre by other means has been a key area of research and there have been many avenues explored over the past decade. A common approach has been to use higher order modulation formats such as quadrature phase shift keying (QPSK) and quadrature amplitude modulation (QAM) [6-8]. These modulation formats increase the spectral efficiency (density) of the channel, thus increasing the information throughput, but require more complex transmitters and receivers. In particular, coherent receivers are generally required in conjunction with the use of digital signal processing (DSP) to decode the received optical signal. Using DSP has the added advantage of being able to reconstruct signal at the receiver by removing linear fibre transmission impairments, and also recovering the clock of the transmitted signal. Since higher order modulation formats introduce more complexity they also introduce extra costs both due to equipment implementation and also due to higher power consumption. In particular when DSP is used in high bitrate systems it can require large computational power which in turn is very power hungry.

Fig. 1.2 demonstrates the increase in information spectral density that coherent detection and higher order modulation formats can provide when compared with direct detection. This graph also demonstrates that simply increasing the signal power indefinitely to increase capacity also has limitations as nonlinear effects occur in fibre, which distort the transmitted optical signal, when the input power reaches a certain power spectral density.
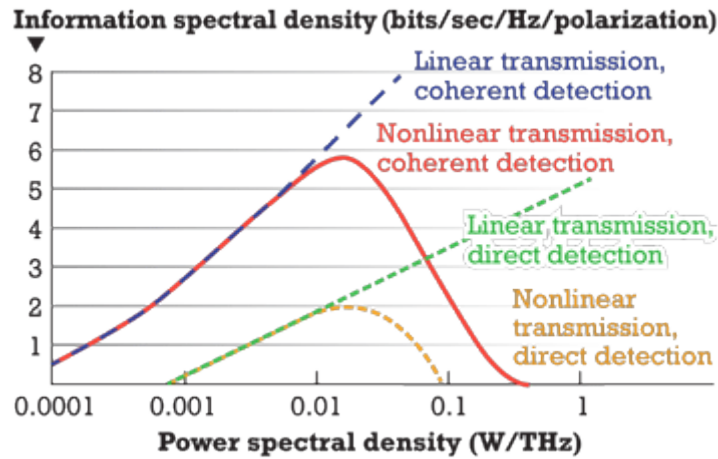
Fig. 1.2 - Information spectral density vs. Power spectral density for various transmission schemes [9].

1.2 Network Architecture

Optical networks are generally divided into three sections; core, metro, and access. Fig. 1.3 shows the most common network topology. The core/backbone network is the long haul communications link used to connect different regions or countries together. These optical links have a long reaches (up to 10,000 km) and require very large capacities as they commonly contain the aggregated telecommunication information for entire countries. The metro networks commonly have reaches of several hundred kilometres and connect networks such as the central offices, mobile tower sites and industrial users and groups of residential homes (access) to the core network. Finally the access networks are considered the "last mile" connecting each homes an optical node in the metro network. A typical access reach is between 40 km and 100 km in the latest passive optical network (PON) architectures.

Fig. 1.3 - Network architecture [10].

1.3 Optical Signal Processing

As the this capacity demand continues to grow and higher order modulation formats become more common, processing these modulation formats in the intermediate optical nodes of an optical network becomes more complex. These optical nodes a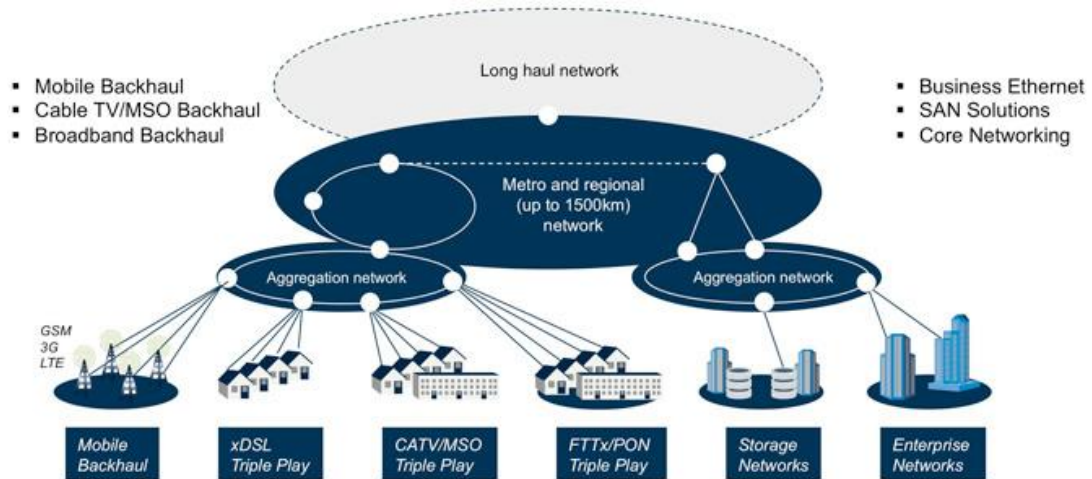re the connections between each of the core, metro, and access networks. Currently most optical networks process the information of the optical signals in the electrical domain. When transmitting between a single transmitter and receiver this approach is acceptable, however, it becomes impractical when used in an optical network where multiple optical nodes exist [1]. One of the basic tasks in an optical node is routing different signals down different optical paths. We consider a wavelength division multiplexed (WDM) signal where one channel may be required to switch to different carrier frequency. An electric-domain implementation would require the demodulation of the optical channel to an RF signal before a laser with the correct optical frequency is then modulated by this electrical signal. If that particular optical channel is also modulated with a high order modulation format such as QAM a coherent receiver and DSP would also be required to demodulate the signal, compounding the complexity required in the optical node. However, in an all-optical approach the channel could be wavelength converted using a continuous wave (CW) laser source and a nonlinear optical device such as a semiconductor optical amplifier (SOA). This all-optical wavelength conversion technique reproduces the data content of the WDM channel on the new carrier frequency.
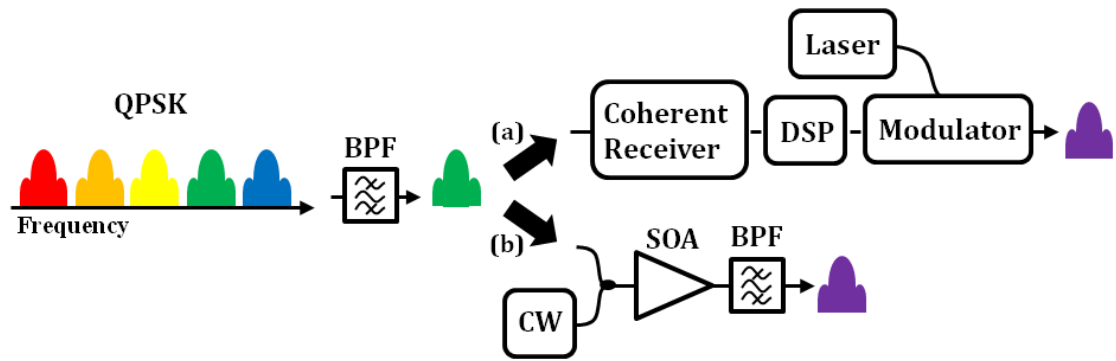
Fig. 1.4 - (a) Electro-optic-electro approach vs. (b) All-optical approach.
Dashed lines = electrical, solid lines = optical, BPF = Band-pass filter

Fig. 1.4 shows a comparison between the two approaches and demonstrates how all-optical signal processing can simplify the optical network and possibly reduce costs either due to equipment or to a reduction in power consumption. In general, this type of processing is referred to as all-optical signal processing due to the signal manipulation occurring in the optical domain only, with no conversion to the electrical domain required. All-optical signal processing is a key area of research for future optical communication networks. For certain applications, particularly in optical nodes, optical signal processing may provide benefits by simplifying the implementation and reducing the power consumption, especially for higher order modulation formats which require complex coherent receivers and DSP.

Optical signal processing is not just limited to wavelength conversion techniques like the example discussed above. In recent years many areas of optical signal processing have been of interest including phase sensitive amplification, all-optical packet switching, and all-optical regeneration. This thesis investigates three all-optical signal processing techniques: an all-optical modulation conversion technique capable of converting an on-off keyed (OOK) signal into either an alternate mark inversion (AMI) or duobinary (DB) modulated signal [11, 12], an all-optical phase discriminator which can separate a QPSK signal into two binary phase shift keyed (BPSK) signals each at different wavelengths [13, 14], and an all-optical clock recovery technique which recovers the clock a from BPSK modulated orthogonal frequency-division multiplexing (OFDM) superchannel [15, 16].

1.4 Nonlinear Devices

Optical signal processing relies on nonlinear elements which have an intensity dependent refractive index, an intensity dependent gain or a combination of both. The two most common nonlinear media are SOAs and highly nonlinear fibre (HNLF). Increasing the optical power injected into either of these devices will alter their refractive index and as a result the phase of any other optical signal transmitted simultaneously through the device, with the SOA also undergoing a change in gain. This forms the basis for most optical signal processing techniques, where a signal's phase, amplitude or wavelength can be manipulated using other optical signal propagated through the same nonlinear medium. SOAs were the nonlinear element of choice for the work carried out in this thesis due to their compact size, sub-milliwatt input power requirements, ease of integration, and their ability to provide gain.

1.5 Thesis Layout

The aim of this thesis is to investigate various all-optical signal processing techniques for next generation optical networks. Chapter 2 of this thesis details any important background information relative to his work including SOAs and their nonlinear effects. Chapter 3 then investigates some important properties of SOAs for all-optical applications, in particular the wavelength dependent nature of the gain and phase recovery in long, nonlinear SOAs. Chapter 4 details an all-optical modulation conversion technique which converts OOK data to either AMI or DB. An all-optical phase sensitive frequency conversion method is demonstrated in Chapter 5. Chapter 6 discusses an all-optical clock recovery method for BPSK modulated all-optical superchannels and finally Chapter 7 provides a conclusion to this work.

2.

Fundamentals

This chapter discusses the background information important to the work covered in this thesis. In particular this chapter aims to highlight the relevant aspects of semiconductor optical amplifiers (SOAs) which are of importance for all-optical applications. This includes the nonlinearities associated with SOAs and their advantages and disadvantages. Other components such as Mach-Zehnder modulators (MZM) and delay interferometers (DI) are discussed in detail as they are crucial to the experimental work covered later in this thesis.

2.1 Modulation

In any communication system a means of encoding information onto a carrier is required and this is known as modulation. Electromagnetic waves are the most common form of carrier signal used, and in the case of optical communications an optical signal, commonly produced from a laser source is used. This light is then modulated and propagated through a medium such as silica fibre, which confines the light and guides it from to the receiver where the signal is detected and decoded.
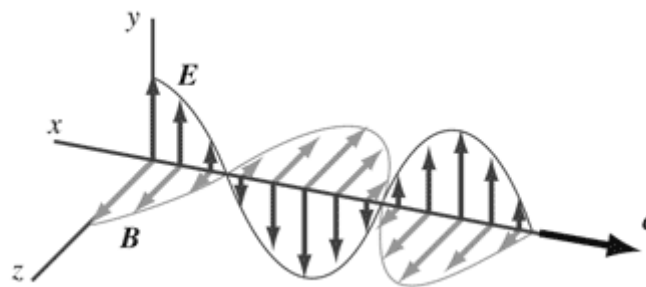

Fig. 2.1 – Electromagnetic wave propagation. E = electric field and B = magnetic field. [17]

An optical carrier signal can be described by the following equation:

$$E(t) = \hat{\mathbf{e}} E_0 \cos(\omega_0 t - \varphi) \tag{2-1}$$

where $E(t)$ is the carrier electric field vector, $\hat{\mathbf{e}}$ is the polarisation unit vector, E_0 is the amplitude, ω_0 is the carrier (angular) frequency, t is the time and φ is the carrier phase. It is possible to convey information by varying any one or a combination of the amplitude, frequency, phase and polarisation of the carrier. Traditionally the frequency of the optical carrier is not modulated; instead multiple optical signals with different frequencies are used as carriers, each capable of carrying different information and thus capable of increasing the information throughput. One particular format of interest in this thesis is called Orthogonal Frequency Division multiplexing [15, 16, 18] and is discussed in greater detail in Chapter 6. For the purpose of this thesis only amplitude and phase modulated formats are of interest.

2.1.1   Amplitude Modulated Formats

A typical modulation format used in optical communication systems is called on-off Keying (OOK) where the information is conveyed using the intensity or amplitude of the optical carrier. In this format a binary '1' is represented by a pulse of light and '0' is represented by no light being present. The most common types of OOK modulation are return-to-zero (RZ) and non-return-to-zero (NRZ). In RZ-OOK the carrier's intensity returns to zero in each bit slot regardless of whether it was a '1' or a '0'. In comparison, NRZ does not reset to zero within each bit slot as can be observed in Fig. 2.2.
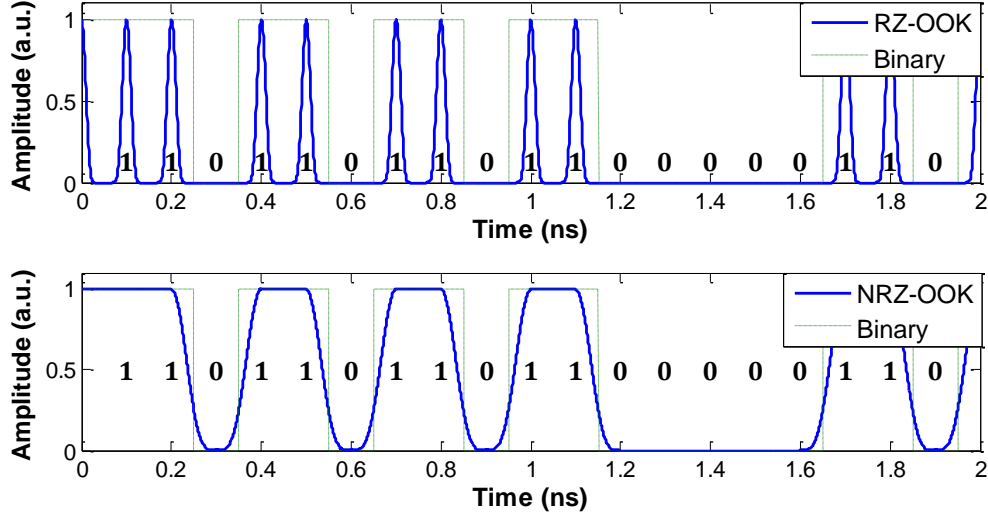
Fig. 2.2 – Comparison of RZ-OOK and NRZ-OOK modulation formats.

Some variations of OOK modulation, such as duobinary (DB) and alternate mark inversion (AMI) include an auxiliary phase modulation. This phase modulation does not contain any information but is included to increase the signals tolerance to dispersion from propagation through fibre. These modulation formats are discussed in more detail in Chapter 4.

2.1.2 Phase Modulated Formats

Phase modulated formats, such as binary phase shift keying (BPSK) and quadrature phase shift keying (QPSK) have become increasingly common in today's optical networks. These modulation formats can provide increased tolerance to transmission impairments [19], higher spectral efficiencies [20, 21], and increased receiver sensitivity [22, 23], when compared to OOK modulation formats. Spectral efficiency is a measure of the capacity of a given modulation format defined over a certain bandwidth. It is measured in bits/s/Hz and provides a means of comparing modulation formats.

In the BPSK modulation format the optical carrier switches between two phase states, 0 and π, representing a binary '0' and '1' respectively. As with the two OOK modulation formats mentioned above each symbol represents either a '0' or a '1'. However, in QPSK modulation each bit slot, or symbol, the optical carrier can have one of four phase states, 0, π/2, π, 3 π/2, each of which represents '00', '01', '11', and '10' respectively. Due to the absence an optical phase reference in these formats, differential encoding is commonly used for

optical transmission. In differential encoding each bit acts as the phase reference for the subsequent bit. Differential phase-shift keying (DPSK) or differential BPSK (DBPSK) differs from BPSK in that a '1' is represented by a change in phase by a transition from either 0 to π or π to 0, where as a '0' is represented by no change in phase from one bit to the next.

Constellation diagrams are used to describe phase modulated signals since they plot both the phase and intensity of a signal. The constellation diagrams for BPSK and QPSK are shown in Fig. 2.3 (a) and (b). Here we can observe the greater number of constellation points that QPSK has compared to BPSK. Fig. 2.3(c) demonstrates the quadrature amplitude modulation (QAM) modulation format, which combines amplitude and phase modulation to increase the number states per symbol resulting in an increased spectral efficiency.

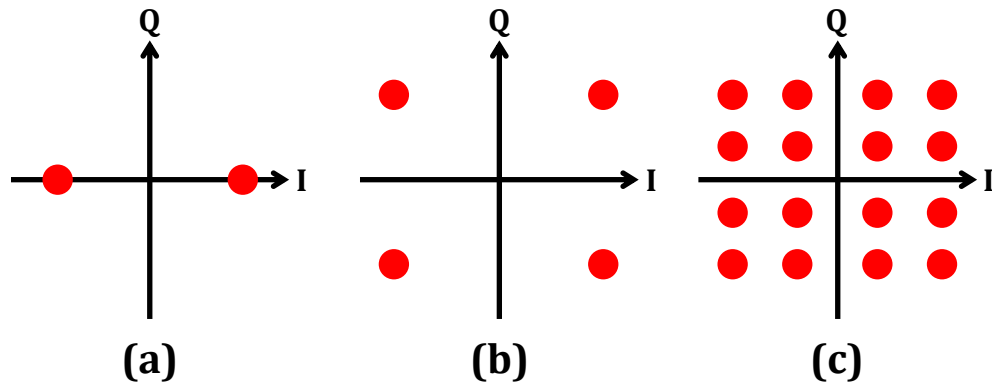

(a)   **(b)**   **(c)**

Fig. 2.3 – Constellation diagrams (a) BPSK (b) QPSK (c) QAM

An important factor to consider when implementing phase modulated formats is the phase noise sensitivity associated with them. Since the information is encoded onto the phase of the optical signal any noise added to the phase of the signal will degrade signal recovered at the receiver. This can be observed on the constellation diagrams. A smaller phase noise represents tighter constellation points, meaning they are further from each other and the chance of interference between them is reduced. Phase noise can arise during transmission and the modulation process. The laser linewidth is the width of the optical spectrum of the laser. It can also be thought of as a probability distribution of the photons emerging from the laser source. During the modulation process the laser linewidth determines the initial phase noise of the

modulated optical signal before transmission. By minimising the linewidth of the laser at the transmitter the signal at the receiver can be improved.

A major disadvantage of phase modulated signals when compared with OOK data is the increased complexity in demodulating the optical signal. OOK formats can be decoded using simple square law detectors (photodiodes) and a decision circuit; however, photodiodes are insensitive to the phase of the optical signal and can only detect intensity variations. Phase modulation formats can be decoded using various schemes including delay interferometers (DI) [24] (which are discussed later in this chapter) and coherent receivers [21, 25]. A novel all-optical method of demodulating QPSK signals is demonstrated in Chapter 5 of this thesis.

2.2 Semiconductor Optical Amplifiers

Semiconductor optical amplifiers (SOAs) were originally developed as potential amplifiers in optical systems but are rarely used now for fibre loss compensation due to the development of Raman amplifiers and the erbium-doped fibre amplifier (EDFA) in the 1980's [2]. These devices have low noise figures (3-5 dB), can amplify many wavelength division multiplexed (WDM) channels without crosstalk, and can run in saturation without patterning, none of which can be said of SOAs. However, SOAs exhibit many nonlinearities which are useful for a wide variety of applications including wavelength conversion, all-optical switching, and all-optical signal processing. This coupled with their compactness and integration potential has made them an interesting research topic.
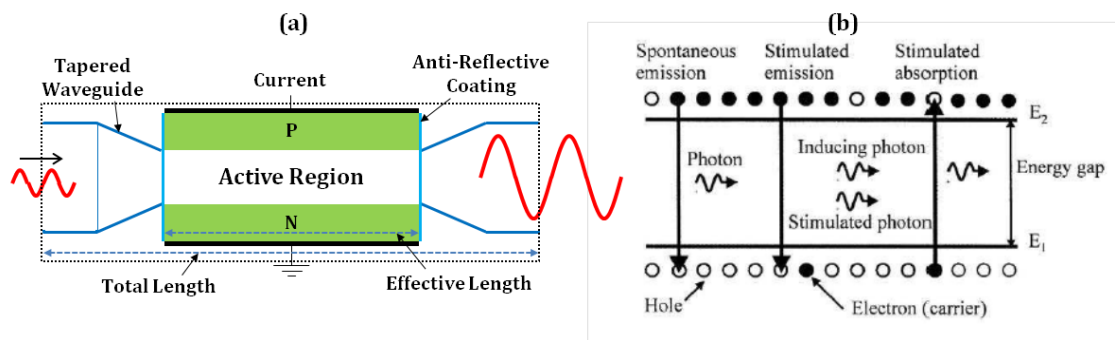

Fig. 2.4 – (a) SOA diagram side view. (b) Spontaneous and stimulated emission process. [26]

SOAs are similar to semiconductor lasers in that they have a gain region which is electrically pumped to provide electrons to the active region. Most SOAs are designed to be single-pass devices such that any signal injected into them will only pass through the active region once before being emitted from the device. This differs from semiconductor lasers where a Fabry–Pérot cavity is formed to produce an optical resonator around the active region. In SOAs, an anti-reflective coating is used at each facet and this in conjunction with a tilted stripe design minimises reflections [26-28]. When light is then injected into one facet of the device, it travels the length of the SOA and is amplified due to stimulated emission before exiting at the second facet as shown in Fig. 2.4. A tapered waveguide is commonly used to guide light into and out of the SOA active region. As such, there are two lengths associated with the device: the total length including the waveguide and the effective length which is the length of the active region. The effective length is more commonly referred to as this is the length over which amplification occurs due to stimulated emission. In Chapter 3 the characteristics of an SOA with a long effective length are investigated. In the subsequent chapters devices with shorter effective lengths are utilised.

The gain bandwidth of these devices is determined by the material used to produce the SOA (e.g. InGaAs) as well as other factors such as strain, etc. An example gain spectrum for a SOA driven with 400 mA of current is shown in Fig. 2.5. It is possible for the 3-dB bandwidth of these devices to reach 100 nm.
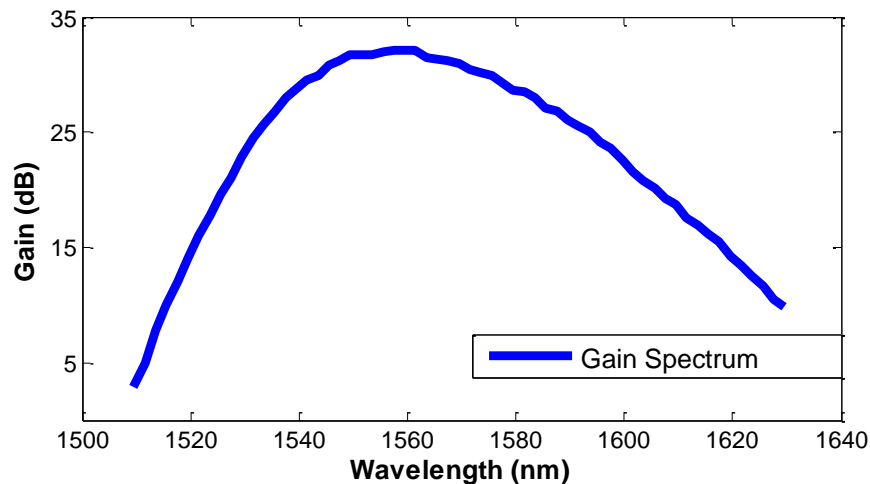

Fig. 2.5 – SOA gain spectrum.

Spontaneous emission is another process present in SOAs and is the main source of noise in these devices. Carriers will randomly transition from the conduction band to the valence band with the energy difference emitted as a photon. Spontaneous emission occurs along the full length of the SOA producing photons which can travel in either direction along the length of the device. Stimulated emission will amplify these photons giving rise to what is called amplified spontaneous emission (ASE). Due to the random nature of this process the noise will be spread over many wavelengths or frequencies defined by the gain spectrum of the material. This can be seen in Fig. 2.6 where a plot of measured ASE vs. wavelength can be observed for a SOA driven by 200 mA and with no optical signal injected into either facet.
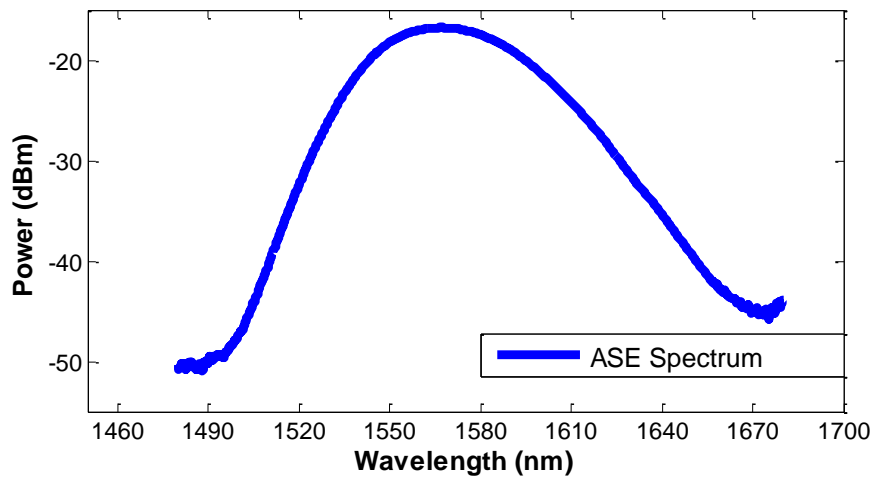

Fig. 2.6 – SOA ASE spectrum.

When an optical signal is injected into a SOA it will reduce the number of carriers due to amplification by stimulated emission. This will reduce the amount of ASE produced by the device, however, some ASE is always present. Both the gain of the device and the ASE produced are proportional to the current injected into the gain material. As the drive current increases there is a greater number of carriers available for both stimulated and spontaneous emission which the gain and the ASE are dependent upon.

2.2.1   Optical gain and saturation

If a continuous wave (CW) optical signal is launched into the SOA it will be amplified exponentially by the single pass gain, G, as long as the gain remains unsaturated.

$$G = \exp(gL) \tag{2-2}$$

where g is the gain coefficient and L is the effective length of the device. The modal gain coefficient, g is related to the electron, or carrier, density, N by:

$$g(N) = \Gamma\sigma_g(N - N_0) \tag{2-3}$$

where Γ is the confinement factor (the fraction of the propagating signal field mode power confined to the active region), σ_g is the gain cross section and N_0 is electron density for which the SOA is transparent. These parameters are determined by the design of the SOA such as the gain material, etc.

The widely used rate equation which describes the change in carrier density as a function of time is:

$$\frac{dN}{dt} = \frac{I}{qV} - \frac{N}{\tau_c} - \frac{\sigma_g(N - N_0)}{\sigma_m h v}P \tag{2-4}$$

where I is the drive current, V is the volume of the active region, q is the electron charge, τ_c is the carrier lifetime, σ_m is the effective area of the waveguide mode, h is Planck's constant, v is the optical frequency and P is the power of the signal input to the device.

If a CW signal or a pulsed signal with pulses much longer than the carrier lifetime, τ_c, is input to the SOA the steady state value of N can be found by setting $dN/dt = 0$.

When this value is the substituted into Eq. (2-3) the optical gain is found to saturate as:

$$g = \frac{g_0}{1 + \dfrac{P}{P_s}} \tag{2-5}$$

where the small signal gain g_0 is given by:

$$g_0 = \Gamma\sigma_g\left[\frac{I\tau_c}{qV} - N_0\right] \tag{2-6}$$

and the saturated power P_s is defined as:

$$P_s = \frac{\sigma_m h v}{\sigma_g \tau_c} \tag{2-7}$$

This optical saturation can be observed in Fig. 2.7(a) where a plot is shown of gain versus input power. As the input power increases the gain decreases which is expected from Eq. (2-5). The gain vs. the output power for this input power sweep is also shown in Fig. 2.7(b) demonstrating the output power saturation that occurs once a sufficiently large input is injected into the device.
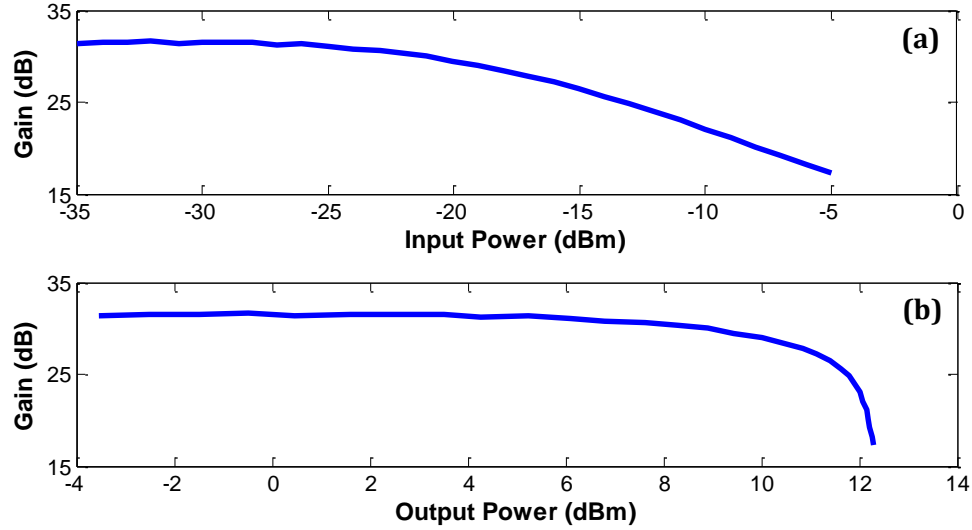

Fig. 2.7 – (a) Gain vs. input power (b) Gain vs. output power.

2.2.2 Carrier Dynamics

For future high-speed optical communication networks ultrafast switches are required for a variety of applications. SOAs, in particular, have been the focus of much research as active switching devices [29, 30]. Their limiting factors, however, are their gain and phase recovery times, as these determine how quickly the device can switch. As a signal is amplified through a SOA it saturates the gain and reduces the carrier density by stimulated emission. This reduction in carrier density not only affects the optical gain but also changes the refractive index of the material. As the refractive index changes, it alters the phase of any signal passing through the SOA. The recovery times are the times taken for the gain and phase to recover as a result of the carriers replenishing. This relationship between gain and phase can be described using the Kramers-Kronig relation and it can be shown that the ratio between the change in refractive index and the change in gain with respect to the carrier density N, is governed by the alpha factor α [31, 32]:

$$\alpha = -\frac{4}{\lambda}\frac{\delta n_r/\delta N}{\delta g/\delta N} \simeq -\frac{4}{\lambda}\frac{\Delta n_r}{\Delta g} \qquad (2\text{-}8)$$

where Δn_r is the variation in the real part of the effective refractive index n, Δg is the variation in the net modal gain g, and λ is the wavelength.

In general, the recovery rates can be characterised by an ultrafast component which is dependent on intraband effects such as spectral hole burning, carrier heating and subsequent carrier cooling and also a slower, interband, band-filling process [33-35]. In the band-filling process, carriers are replenished due to electrical pumping. This takes the order of several hundred picoseconds and is ultimately determined by the current injection. Spectral-hole burning occurs when stimulated emission burns a hole in the carrier distribution in energy space, which causes a deviation from the Fermi distribution. The time associated with this process is the time required to restore the Fermi distribution (carrier-carrier scattering time) and is in the order of several tens of femtoseconds [33]. Carrier heating is the removal of carriers from low energy levels by stimulated emission or by transferring to higher energy levels by free-carrier absorption. The time constant associated with the carriers to cool down (due to carrier-phonon scattering) is typically in the order of several hundreds of femtoseconds [33]. Despite ultrafast processes in the carrier recovery, the full gain recovery in most SOAs is limited by the slow band-filling process [36].

If a CW signal is launched into a SOA the device quickly reaches a steady state, as mentioned previously. However, if a pulsed signal passes through a SOA the period between pulses must be longer than the recovery time, otherwise pattering results. Patterning occurs when a pulse enters a SOA and saturates it, removing most of the available carriers. If the next pulse enters before the gain can recover, it will experience less amplification and will exit the SOA with less power. With a string of pulses the effect is compounded and this results in a degradation of the extinction ratio of the Eye diagram and a reduction in the Optical Signal to Noise Ratio (OSNR).
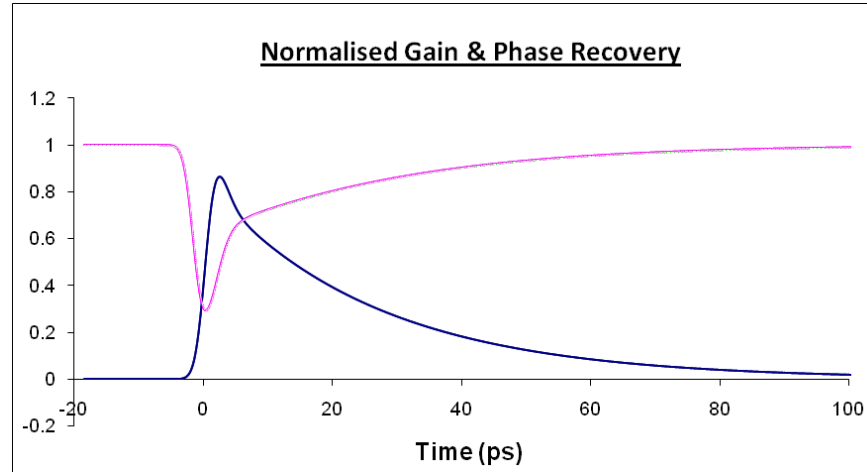
Fig. 2.8 – Normalised SOA gain (pink) and phase (blue) recovery.

An example of a gain and phase recovery curve for a SOA can be seen in Fig. 2.8. Both the gain and phase are fully recovered after ~100ps which is typical for a bulk type SOA. This effectively limits the operation of this device to repetition rates of <10 GHz. There are multiple techniques which can either reduce the carrier lifetime or mitigate its effects including narrow bandpass filtering, the use of a holding beam or employing two SOAs in either a Turbo-Switch arrangement or a "push-pull" interferometer [13, 32, 37-41]. Chapter 3 of this thesis details a method of improving the response of a SOA based on wavelength selection of the input signals and Chapter 4 employs a SOA based logic gates, which use "push-pull" interferometers to operate at higher bit rates.

2.2.3 Nonlinear Effects

As mentioned in the previously any optical signal injected into a SOA will induce a change in the carrier density of the device. These carrier density fluctuations will produce nonlinear effects in SOAs. The four main types of nonlinearities in SOAs are: Cross gain modulation (XGM), self-phase modulation (SPM), cross phase modulation (XPM) and four-wave mixing (FWM).

2.2.4 Cross Gain Modulation

If an amplitude modulated signal, in this example a pulsed pump, is injected into a SOA, it will cause a modulation of the carrier density of the SOA due to amplification by stimulated emission. As each pulse is amplified it will reduce the available gain in the SOA before recovering. Any other signal, travelling

through the device at the same time will observe this gain fluctuation and be modulated by it. An example of this can be seen in Fig. 2.9 where a pulsed pump and a CW probe are injected in to the SOA. At the output both pump and probe will have the same amplitude modulation, i.e. the signal has been wavelength converted.
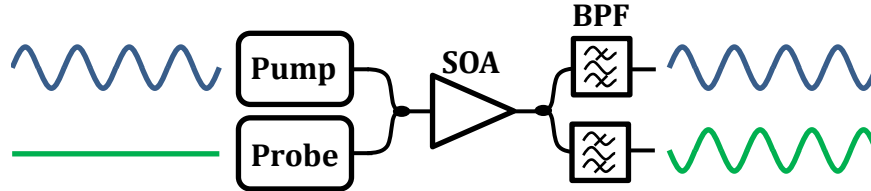

Fig. 2.9 – Wavelength conversion due to XGM. Bandpass filter = BPF.

2.2.5   Self-Phase and Cross Phase Modulation

As mentioned previously, the refractive index of the SOA is not a constant but is related to the carrier density of the material, and consequently the gain via the Kramers-Kronig relationship. Any variation in gain will cause a change in the refractive index which will in turn alter the phase of any signal passing through the SOA. When a signal pulse injected into the SOA it causes a change in the carrier density and a corresponding change in gain and phase. Due to the finite carrier lifetime, the leading edge of the pulse will experience a different gain and phase shift to the trailing edge. The phase shift experienced by the pulse as a consequence of its effect on the refractive index is known as self-phase modulation (SPM), and the combination of gain and phase changes, will change the pulse shape and its spectrum. However, if more than one signal is injected into the device there will be cross-phase modulation (XPM) between the signals. XPM can be used for wavelength conversion by placing the SOA in an interferometric configuration which converts the signal phase changes to a variation in intensity. One common interferometric design is a Mach-Zehnder interferometer (MZI) which is discussed in more detail later in this chapter. SOA-based MZIs used to all-optically convert modulation formats are discussed in more detail in Chapter 4.

2.2.6 Four-Wave Mixing

Another nonlinear process, present in SOAs, is four-wave mixing (FWM). FWM occurs when two or more signals, propagating through a SOA at different frequencies (f_1 and f_2), beat together to produce adjacent frequency components at multiples of their frequency separation, Δf ($= f_2 - f_1$), as shown in Fig. 2.10.
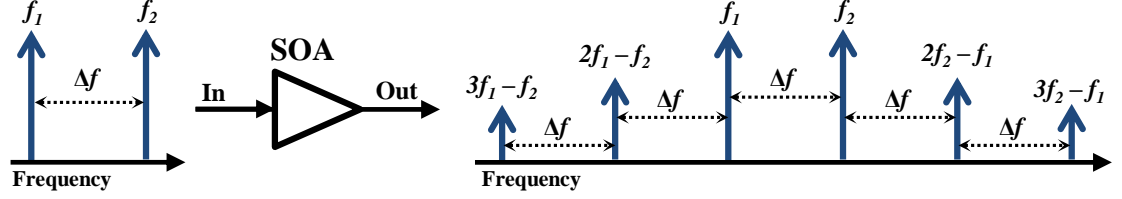

Fig. 2.10 – Example of FWM in SOA.

If we consider two CW signals with frequencies, f_1 and f_2, such that their fields E1 and E2 are given by:

$$E1(t) = E_0 e^{i2\pi f_1 t}$$

$$E2(t) = E_0 e^{i2\pi f_2 t}$$

(2-9)

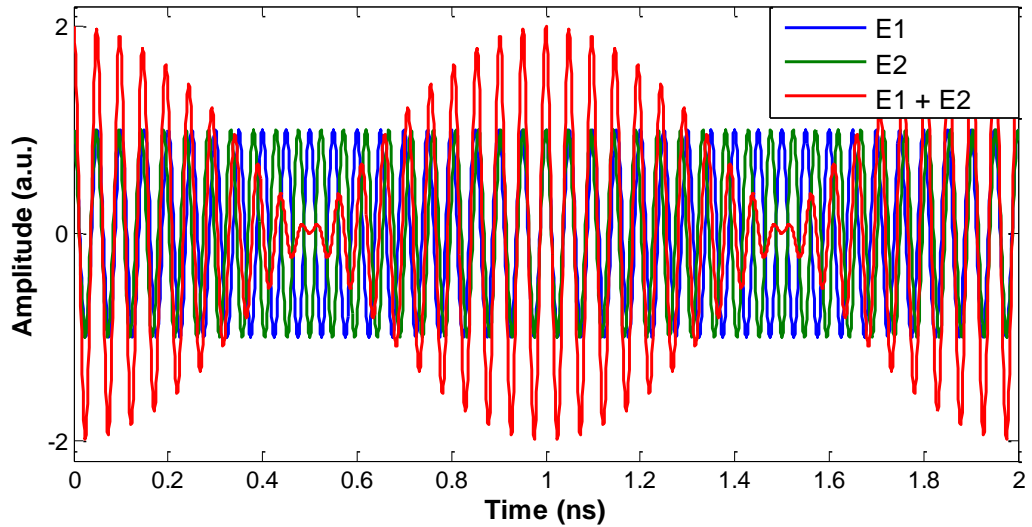a plot of the two fields and their superposition is shown in Fig. 2.11.

Fig. 2.11 – Two CW signals, E1 (blue) and E2 (green) and their superposition (red). Low frequencies for E1 and E2 (~20 GHz) are chosen so that their carriers are visible. In a real system the carriers would in of the order of THz.

If these two signals travel through a SOA they will beat at the difference frequency between them, given by:

$$\Delta f = f_2 - f_1$$

(2-10)

This is an intensity beating given by the envelope of the square of the sum of the two fields, E1 and E2, as shown in Fig. 2.12.
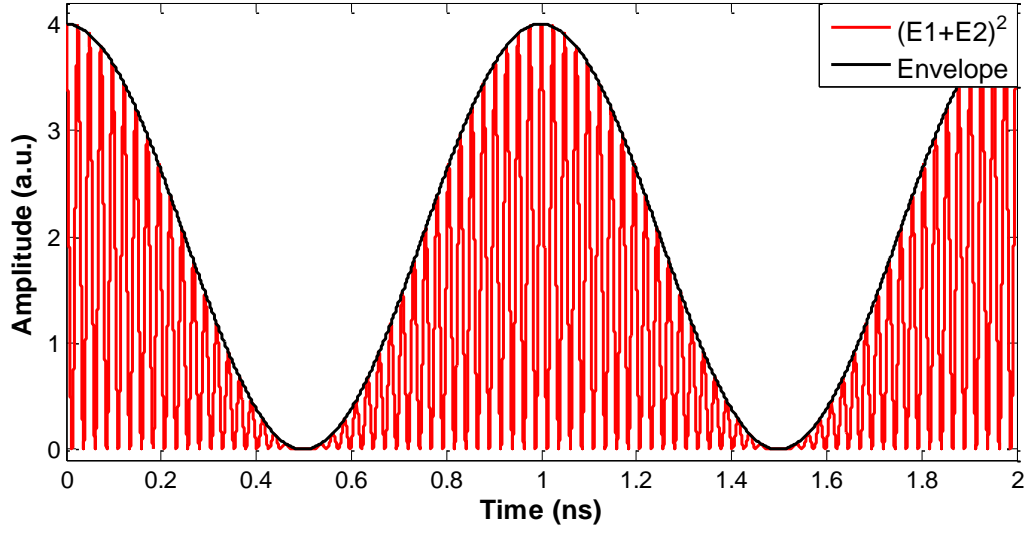

Fig. 2.12 - Square of the sum of the two fields (red). Envelope of beating (black).

This beating, at Δ*f*, modulates the carrier density of the SOA which in turn modulates the gain and the refractive index. All signals passing through the device are thus amplitude and phase modulated at Δ*f*. When a signal is modulated it produces sidebands at multiples of the modulation frequency and this is the process by which FWM produces new frequency components.

Amplitude modulation (AM) will produce two sidebands, one either side of the original carrier and separated by the modulation frequency, Δ*f*. This can be demonstrated by considering a carrier signal:

$$E(t) = E_0 \cos(\omega t) \qquad (2\text{-}11)$$

where E_0 is the amplitude, ω, is the angular frequency such that, $\omega = 2\pi f$, and t is the time. If this carrier is then amplitude modulated with a depth (or index), *m*, and frequency, Δ*f*, it becomes:

$$E = E_0 \cos(\omega t)[1 + m \sin(\Delta f t)] \qquad (2\text{-}12)$$

By using the well-known trigonometric identity for cosA*sinB we can obtain:

$$E = E_0 \left\{ \cos(\omega t) + \frac{m}{2} [\sin(\omega + \Delta f)t - \sin(\omega - \Delta f)t] \right\} \qquad (2\text{-}13)$$

2. Fundamentals

demonstrating that two sidebands are produced at $\omega + \Delta f$ and $\omega - \Delta f$ as expected. If this signal is phase modulated, however, with frequency Δf and modulation index β it adds a time dependent phase as follows:

$$E = E_0 \cos(\omega t + \beta \sin(\Delta f t)) \tag{2-14}$$

Since β is small:

$$E = E_0[\cos(\omega t) - \beta \sin(\omega t) \sin(\Delta f t)] \tag{2-15}$$

Using the trigonometric identity for sinA*sinB gives:

$$E = E_0 \left\{ \cos(\omega t) + \frac{\beta}{2} [\cos(\omega + \Delta f)t - \cos(\omega - \Delta f)t] \right\} \tag{2-16}$$

This is a simplified derivation of the phase modulation (PM) as it only produces two sidebands at $\omega + \Delta f$ and $\omega - \Delta f$. For a simple analysis of FWM this derivation is enough, however, in most applications the higher order sidebands produced by FWM are also of importance. As such, the proper expression for PM is described by a series of Bessel functions which produces multiple sidebands at multiples of the modulation frequency, Δf. Consider the carrier:

$$E(t) = E_0 e^{i\omega t} \tag{2-17}$$

which is then phase modulated by a sinusoidal signal:

$$E = E_0 e^{i(\omega t + \beta \cos(\Delta f t))} \tag{2-18}$$

Eq. (2-18) can be expanded using the identity:

$$e^{iz \cos \varphi} = \sum_{k=-\infty}^{\infty} i^k J_k(z) e^{ik\varphi} \tag{2-19}$$

with Bessel functions of the first kind $J_k(\beta)$:

$$E = E_0 e^{i\omega t} \sum_{k=-\infty}^{\infty} i^k J_k(\beta) e^{ik\Delta f t} \tag{2-20}$$

This gives an infinite series of Bessel functions with $k = 0$ representing the carrier oscillating at the input field frequency ω, $k > 0$ the upper sidebands and

$k < 0$ the lower sidebands. In reality, the Bessel functions decrease with increasing order, k, and Eq. (2-20) can be rewritten as:

$$E = E_0 e^{i\omega t}\left(J_0(\beta) + \sum_{k=1}^{order} J_k(\beta)e^{ik\Delta ft} + \sum_{k=1}^{order}(-1)^k J_k(\beta)e^{-ik\Delta ft}\right) \quad (2\text{-}21)$$

where *order* represents the highest order sideband required. In this equation the carrier, the upper sidebands, and lower sidebands are represented separately.

The spectra for amplitude and phase modulation of a CW signal can be seen in Fig. 2.13(a) and (b).
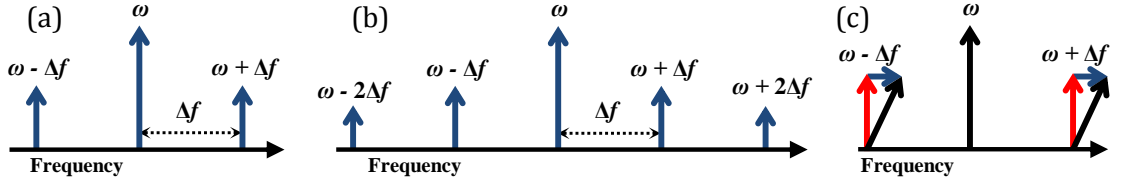

Fig. 2.13 – (a) Amplitude modulation (b) Phase modulation (c) Phasor diagram of first two sidebands due to AM (blue) and PM (red)

If the amplitude and phase modulation are generated from the same source, in this case the beating between signals, the sidebands produced due to phase modulation will lead the amplitude modulation sidebands by π/2 radians. This can be observed in the phasor diagram in Fig. 2.13(c). In SOAs, the alpha factor, α, given by Eq. (2-8) in Section 2.2.2 determines the relative size of the AM and PM modulation indexes, i.e.

$$\beta = \alpha m \quad (2\text{-}22)$$

Typically SOAs have alpha factors > 5, meaning that the phase modulation will have a much larger contribution to the FWM process. An example of the breakdown of the components produced due to both AM and PM in FWM is shown in Fig. 2.14. Both Fig. 2.13(c) and Fig. 2.14 also demonstrate that the sidebands produced are from a combination of the both amplitude and phase
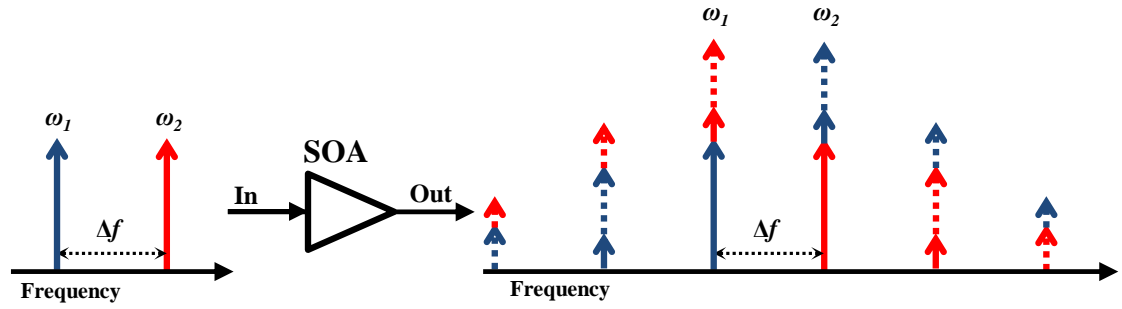
modulation.

Fig. 2.14 – Breakdown of FWM in SOA. Solid sidebands = AM, dashed lines = PM. Please note these are not phasor diagrams.

At relatively small frequency separations (or detunings), << 1 GHz, the carrier density fluctuation will track the beating between the input signals. However if the frequency separation is increased the carrier density modulation will lag behind the beating driving it. This is due to carrier recovery time associated with SOAs discussed previously in Section 2.2.2. The AM and PM will consequently lag behind the beating and result in a power shift between components on the output spectrum of a SOA, as shown in Fig. 2.15. For this example two equal power (-10 dBm) CW signals, separated by ~50 GHz were injected into the device.
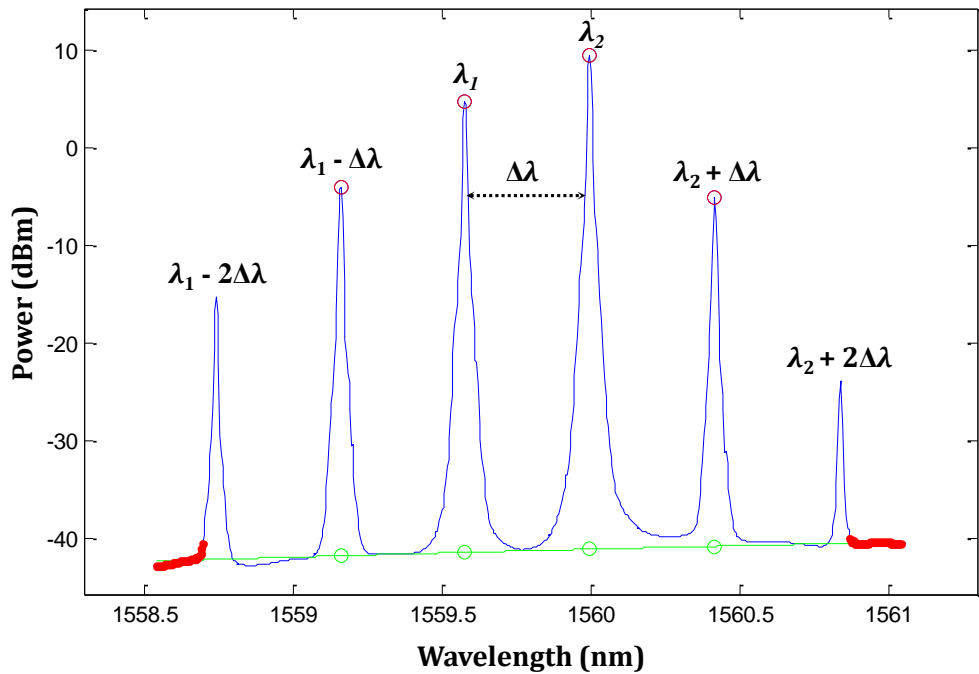

Fig. 2.15 – Measured SOA output spectrum with two equal power CW inputs (λ_1 and λ_2). Red line used to estimate the ASE. Green dots are ASE approximations.

Even though λ_1 and λ_2 were equal in power at the input of the SOA, λ_2 is larger at the output of the device. This can be explained by the phasor diagrams in Fig. 2.16.
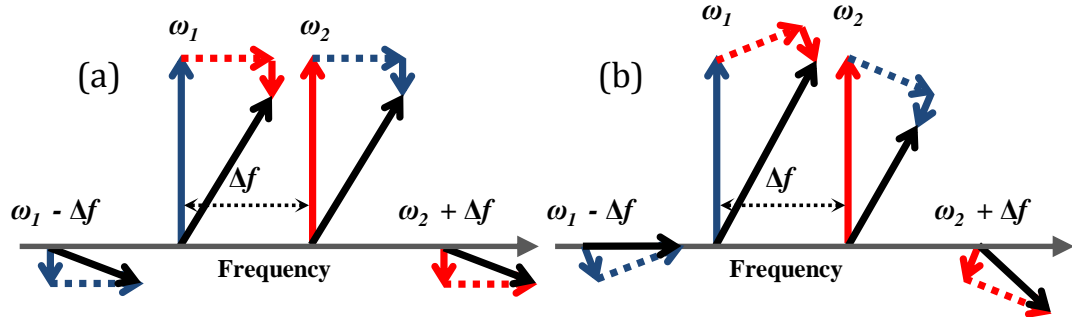

Fig. 2.16 – SOA output phasor diagrams. (a) Small detunings (<< 1 GHz)
(b) Large detunings (>1 GHz)

In Fig. 2.16(a) we can see the output phasor diagram from small detunings and Fig. 2.16(b) shows the output phasor diagram for large detunings. The modulation lag causes power to be transferred from the high frequency, ω_2, (short wavelength, λ_1 in Fig. 2.15) CW tone to the low frequency, ω_1, (long wavelength, λ_2 in Fig. 2.15) tone. The phase lag has little effect on the power of the sidebands produced in Fig. 2.16(b), however, when more terms of the Bessel expansion are included their output power will also change and this can be observed in Fig. 2.15.

The fixed phase relationship in Fig. 2.16 represents a special case when only two inputs are present and the phase of the beat waveform is linked directly to the phase of the two signals. In a multi-channel system, the phase relationship between the beat waveform and any pair of inputs may be arbitrary, resulting in a range of possible amplitudes and phase for each frequency component.

2.3 Mach-Zehnder Interferometer

The Mach-Zehnder interferometer (MZI) has many uses in many different fields. In optical communications the main use of these interferometers is for the filtering, modulation, and demodulation of optical signals. The basic MZI architecture is shown in Fig. 2.17 where an optical signal, $E(t)$, is injected into one of the input ports.
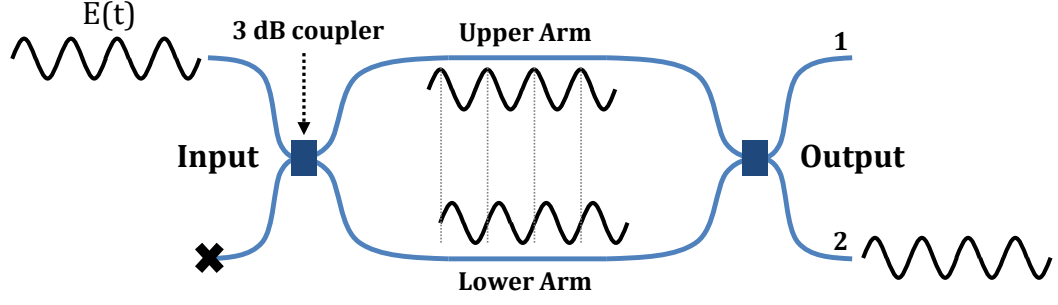
Fig. 2.17 – Mach-Zehnder interferometer architecture. Blue lines represent waveguides.

Couplers commonly have two input and two output ports and when a signal is injected the power is split between the various output ports. The part of the signal that does not cross the coupler (upper arm of Fig 2.17) will only experience a change in electric field amplitude, which is determined by the splitting ratio. In MZIs, 3 dB (50:50) splitters are used which produces two equal power signals. The other part of the signal which crosses the coupler (lower arm of Fig 2.17) will experience not only a change in power but also a phase change of $\pi/2$ radians. If we consider a signal, $E(t) = E_0 e^{i\omega t}$, which has been injected into the MZI, the coupler will thus produce a signal:

$$\frac{E_0}{\sqrt{2}} e^{i\omega t} \tag{2-23}$$

in the upper arm and:

$$\frac{E_0}{\sqrt{2}} e^{i(\omega t + \pi/2)} \tag{2-24}$$

in the lower arm. Eqs. (2-23) and (2-24) demonstrate the equal division (50:50) of power between both arms, introducing a $1/\sqrt{2}$ term to the signal fields, and also phase shift of $\pi/2$ radians in the lower arm. Both signals traverse the equal length arms of the MZI before recombining in the second 3 dB coupler. These signals will then interfere and produce:

$$\frac{1}{\sqrt{2}} \left(\frac{E_0}{\sqrt{2}} e^{i\omega t} + \frac{E_0}{\sqrt{2}} e^{i(\omega t + \pi)} \right) = 0 \tag{2-25}$$

at output port 1. The upper arm signal destructively interferes with the phase shifted signal from the lower arm to produce no output at this port. The second output port, port 2, is given by:

$$\frac{1}{\sqrt{2}}\left(\frac{E_0}{\sqrt{2}}e^{i(\omega t+\pi/2)} + \frac{E_0}{\sqrt{2}}e^{i(\omega t+\pi/2)}\right) = E_0 e^{i(\omega t+\pi/2)} \qquad (2\text{-}26)$$

The signal coming from the upper arm to output port 2 experiences a phase shift, due to the coupler, and constructively interferes with the lower arm signal to produce the original signal injected into the MZI, albeit with a phase delay.

Commonly an adjustable phase control is introduced into one arm of the MZI, whilst maintaining matched arm lengths. This provides control over the interference conditions at the output coupler and can adjust power ratio between output ports, as shown in Fig. 2.18.
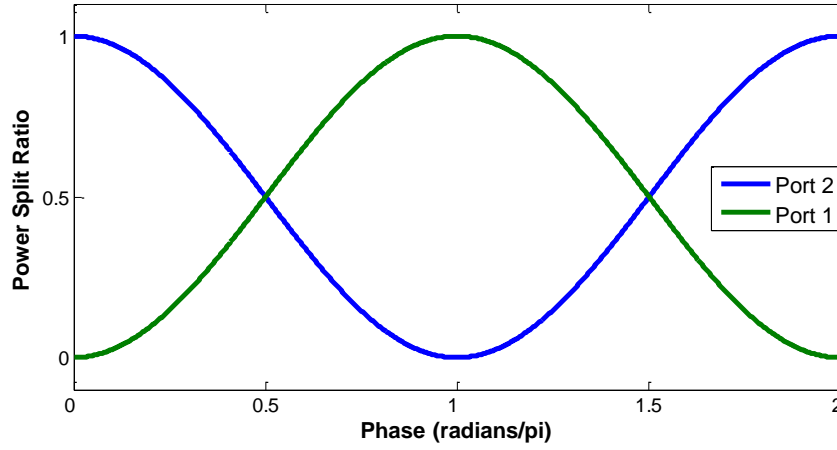

Fig. 2.18 – Phase control over splitting ratio.

Without a phase delay, ($\varphi = 0$), the entire signal is transferred to output port two, as described by Eqs. (2-25) and (2-26). A π phase shift in one of the arms will transfer the entire signal power to the other output port, port 1. This setup is commonly used as a variable power splitter in integrated optical devices.

2.3.1   Delay Interferometer

A delay interferometer (DI), also known as an asymmetric Mach-Zehnder interferometer (AMZI), is a particular type of MZI where one arm of the interferometer is longer than the other, introducing a time delay. This produces a sinusoidal filter which is commonly used to filter channels from WDM systems and to demodulate phase encoded data, such as BPSK data.
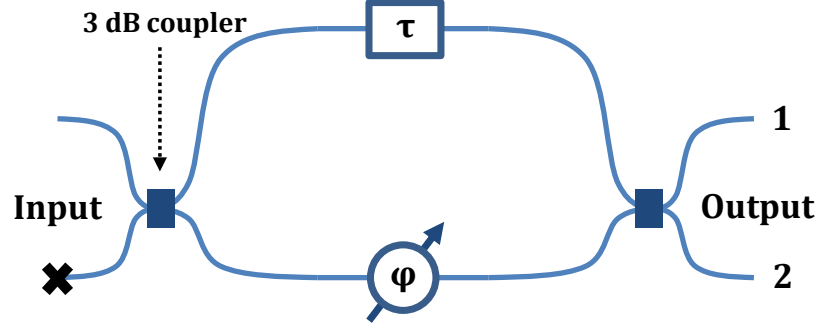
Fig. 2.19 – Delay Interferometer architecture.

A delay, τ, is added to one arm of the MZI by increasing the length of waveguide in that arm. The free spectra range (FSR) is the spacing in frequency between successive intensity maxima or minima of an interferometer and is determined by the time delay, where FSR = 1/ τ. Commonly only one input port of the DI is available and by injecting white Gaussian noise (WGN) the sinusoidal filter shape may be observed. This is demonstrated in Fig. 2.20 where the nulls of the sinusoidal filter, due to the log plot, are visible. A delay of τ = 10 ps was chosen for this example giving a visible FSR of 100 GHz.
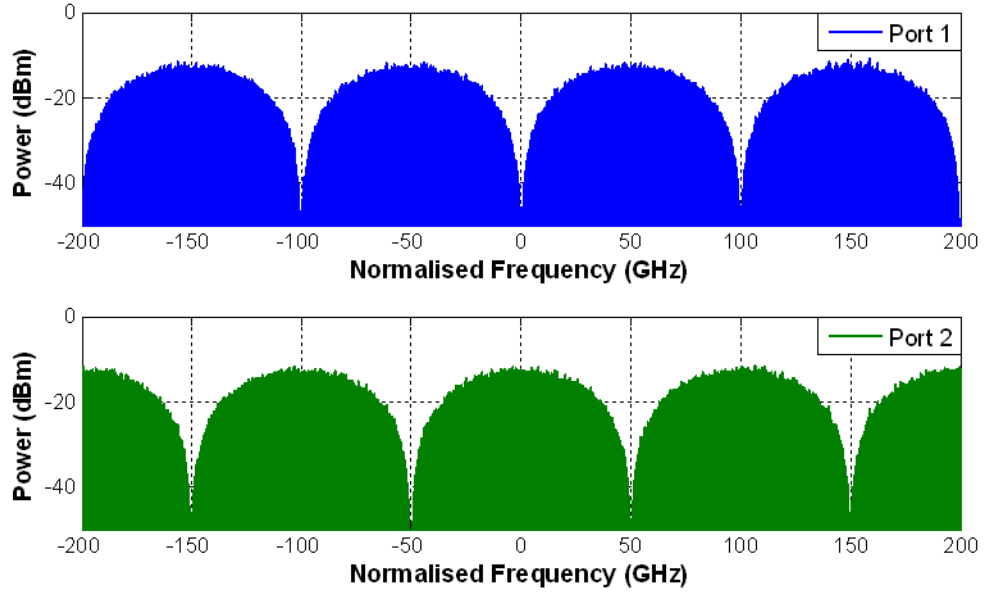

Fig. 2.20 – Both output ports of the DI when white Gaussian noise (WGN) is injected.

The variation between the ports is due to the different interference conditions which produce an offset between them equal to half the FSR (50 GHz in Fig. 2.20). The phase control, φ, in the other arm of the DI can be used to tune the filter; however, the frequency offset between ports will remain constant.

As mentioned in Section 2.1.2, BPSK data encodes binary information onto the phase of its carrier signal, where a '0' is represented by a phase of 0 radians and a '1' by a phase π radians. As a result, phase encoded signals require a receiver which is sensitive to changes in the carrier's phase. A DI can be thought of as a 1 bit delay and add operator which compares the phase of the current bit with the previous bit. When the phase between subsequent bits differs they will destructively interfere and no signal will be present at the output. However, when two subsequent bits are the same the will constructively interfere to produce a signal. This is visualised in Fig. 2.21.
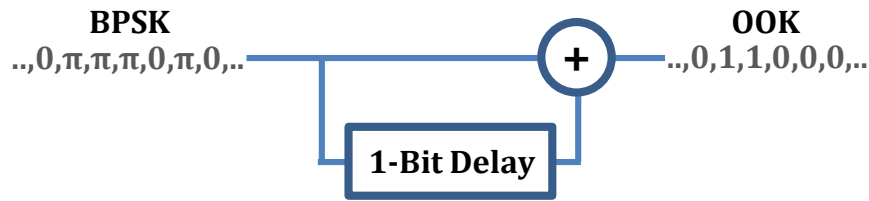

Fig. 2.21 – DI viewed as a 1 bit delay and add operation.

This operation converts the phase modulation (BPSK) to an intensity modulation (NRZ-OOK) which can then be detected using a photodiode. A simulation of a 10 Gbit/s BPSK signal being demodulated by a DI with a delay of 100 ps (FSR = 10 GHz) is demonstrated in Fig. 2.22. An intensity modulation is usually present on the BPSK data, which arises due to the use of a Mach-Zehnder modulator and is discussed in more detail later in this chapter. This residual intensity modulation has no effect on the operation of the DI, however. A PRBS signal was fitted to the recovered OOK data in Fig. 2.22 to demonstrate correct operation.
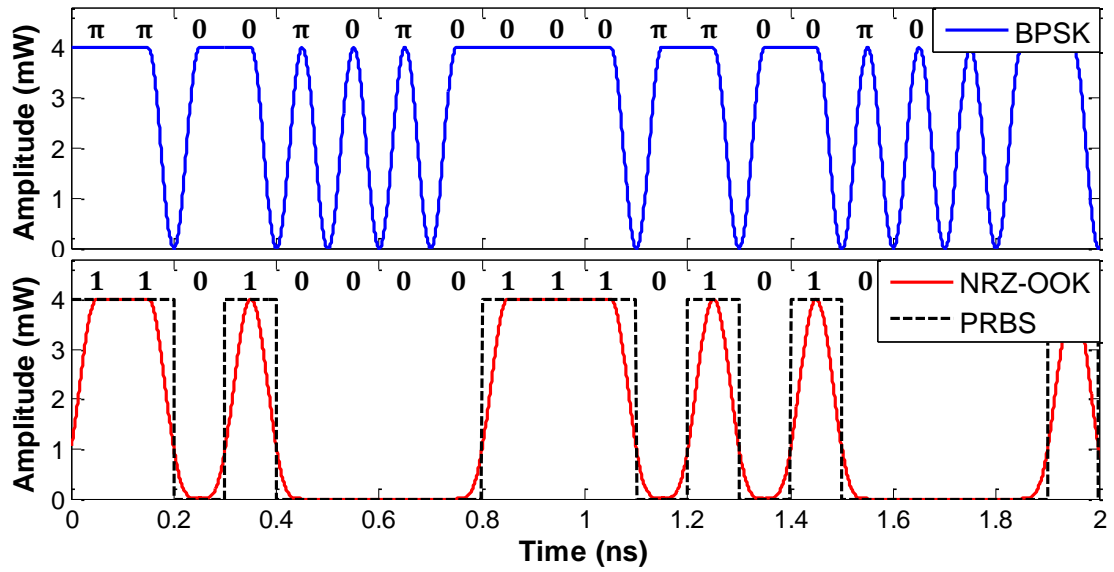
Fig. 2.22 – Time domain example of BPSK demodulation using DI.

It is important to note that the binary information encoded on the OOK signal can differ from the BPSK encoding and the use of precoding or decoding may be required.

2.3.2   Mach-Zehnder Modulator

A Mach-Zehnder modulator (MZM) is a common type of external optical modulator. These devices are widely used in optical communications due to their ability to produce both intensity-modulated (OOK) and phase-modulated formats (e.g. BPSK). A schematic of a MZM can be observed in Fig. 2.23.
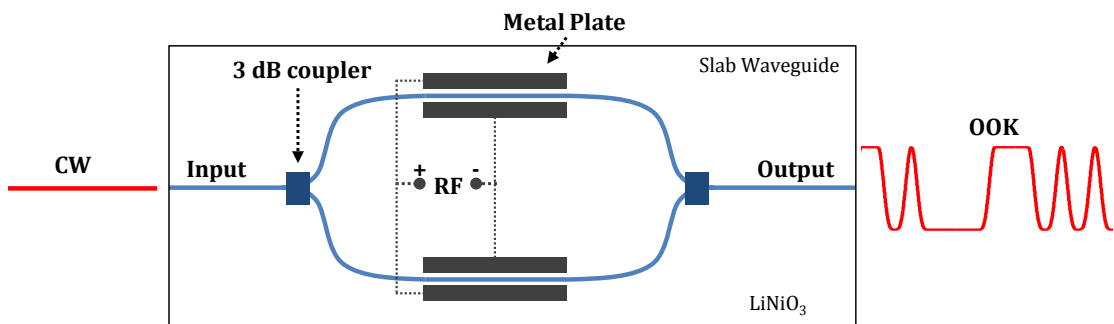

Fig. 2.23 – Integrated MZM schematic.

MZMs use a MZI architecture and are often made from Lithium-Niobate (LiNiO$_3$). Waveguides are formed in Lithium-Niobate by diffusing titanium through the material to increase the local refractive index without altering its electro-optic properties. Lithium-Niobate is commonly used in these devices because of its extremely high electro-optic coefficient. The electro-optic

coefficient is a measure of the electric field dependent refractive index change of a material. By applying a strong electric field to the Lithium-Niobate, the refractive index and consequently the phase of any optical signal passing through the material will change. Considering the travelling wave equation for an electromagnetic field to be:

$$E(t) = E_0 \cos(kz - \omega t) \tag{2-27}$$

where ω is the angular frequency such that $\omega = 2\pi f$, t is the time, z is the distance, k is the wave vector, and consider the phase of the wave to be $\varphi = kz$. The wave vector k is related to the angular frequency by

$$k = \frac{\omega n}{c} = \frac{2\pi n}{\lambda_0} \tag{2-28}$$

where λ_0 is the free-space wavelength and n is the refractive index of the material through which the wave propagates. The phase of the travelling wave can now be written as:

$$\varphi = \frac{2\pi n}{\lambda_0} z \tag{2-29}$$

which demonstrates that the phase is proportional to both the refractive index and distance travelled. A change in refractive index will therefore alter the phase of a signal.

A pair of metal plates are integrated into each arm of the MZM to apply an electric field across the waveguide in each arm, with their length determining the distance, z in Eq. (2-29). This change in phase will alter the interference condition at the output coupler of the MZM. By applying a varying electric field, such as an RF data signal, across the metal plates in each arm of the MZM, the interference conditions at the output coupler can be swept which will in turn modulate any optical signal, such as a CW or RZ pulsed signal, with the same data encoded onto the RF signal. The metal plates are connected inversely in the lower arm compared to the upper arm which will induce opposing phase shifts in each arm. This arrangement is referred to as the 'push-pull' mode of operation.

The bias voltage of the RF signal applied to the device is controlled separately allowing either intensity modulated (OOK) or phase modulated (BPSK) signals to be generated. The transfer function of the MZM, shown in Fig. 2.24, demonstrates how the two types of modulation may be achieved. The horizontal axis represents the RF voltage applied across the electrical contacts shown in Fig. 2.23. The vertical axis represents the optical output power, where 0 represents no output signal and 1 is the maximum output power.
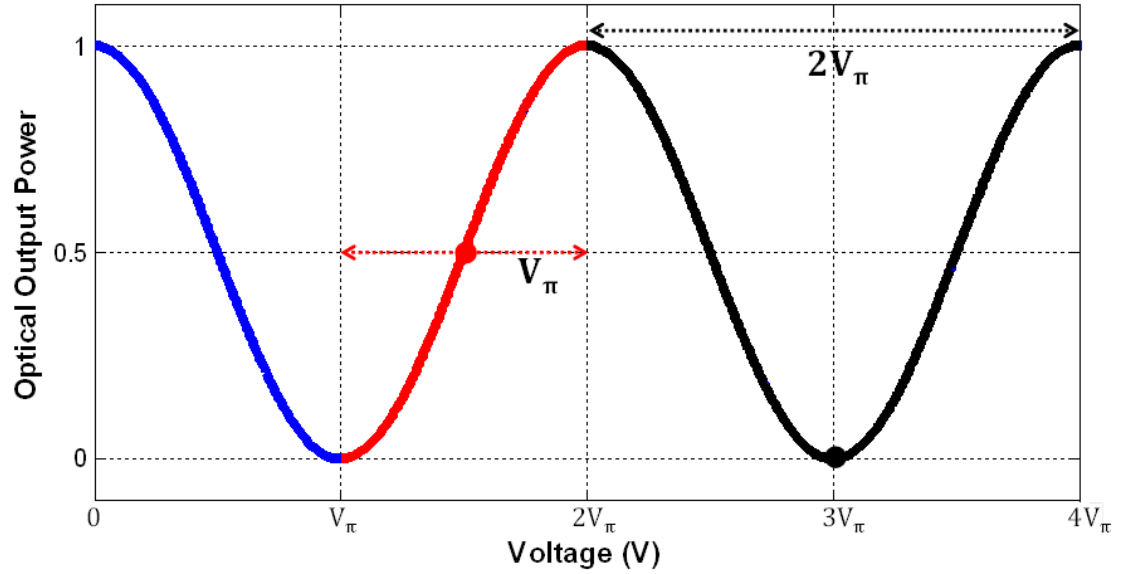

Fig. 2.24 – MZM transfer function. Red = intensity modulation. Black = phase modulation.

Adjusting the voltage bias, V_{Bias}, to the midpoint (e.g. $0.5V_{\pi}$ or $1.5V_{\pi}$ as shown in Fig. 2.24 and represented by the red dot) and applying a RF signal, V_{RF}, with a peak-to-peak voltage of V_{π} will produce an OOK signal. V_{π} denotes the required voltage to change the phase of the signal passing through the Lithium Niobate by π radians. The voltage, V_{π}, is device dependent but typical values are ~3.5 V. As the applied RF electric field, V_{RF}, varies from peak-to-peak (V_{π} to $2V_{\pi}$ in Fig. 2.24) the optical output sweeps from to a 0 to 1 and this is represented by the red line. A phasor diagram demonstration the operating of the MZM in generating OOK is shown in Fig. 2.25.
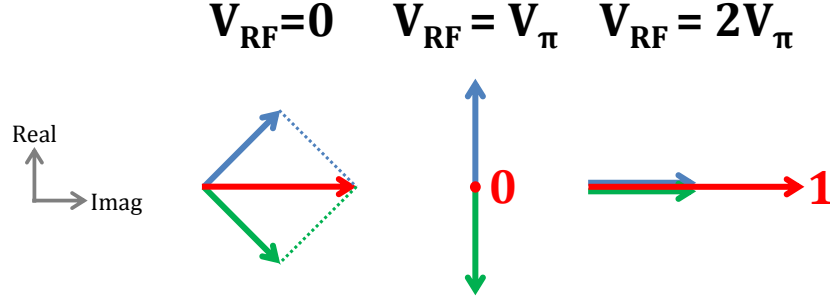
$$\mathbf{V_{RF}=0 \quad V_{RF} = V_\pi \quad V_{RF} = 2V_\pi}$$

Fig. 2.25 – OOK phasor diagram, V_{Bias} = 1.5V_π. Blue line = upper arm optical signal, green line = lower arm optical signal, and red line = output.

When only the bias voltage is present the optical signals from each arm are $\pi/2$ radians out of phase with each other. The RF signal, V_{RF}, will sweep the voltage from V_π, which phase shifts both optical signals so that they are π out of phase with each other and destructively interfere, and 2V_π which makes the two optical signals in phase with each other so they constructively interfere.

To generate BPSK data the device is biased at a null (e.g. V_{Bias} = V_π or 3V_π as shown in Fig. 2.24) and an RF data signal, V_{RF}, is applied to the device. To maximise the output power a RF signal with a peak-to-peak voltage of 2V_π should be applied to the device, however, lower peak to peak voltages will still produce BPSK data. The phasor diagram shown in Fig. 2.26 demonstrates how a π radian phase shift between '0' and '1' is achieved. When only the bias is present the optical signals in each arm are π radians apart and destructively interfere to produce no optical output. When V_{RF} is less than the bias point (<3V_π in Fig. 2.24), the optical signals in each arm interfere to produce an optical signal with a certain phase (e.g. 0 radians). Once V_{RF} sweeps back past the bias point, V_{Bias}, the phase of the output switches by π radians. This is demonstrated in Fig. 2.26, where two arbitrary V_{RF} voltages (V_{RF} = 2.2V_π and V_{RF} = 3.8 V_π) which are either side of V_{Bias} (3V_π) are shown.

$$V_{RF}=0 \qquad V_{RF} = \sim 2.2V_{\pi} \qquad V_{RF} = \sim 3.8V_{\pi}$$

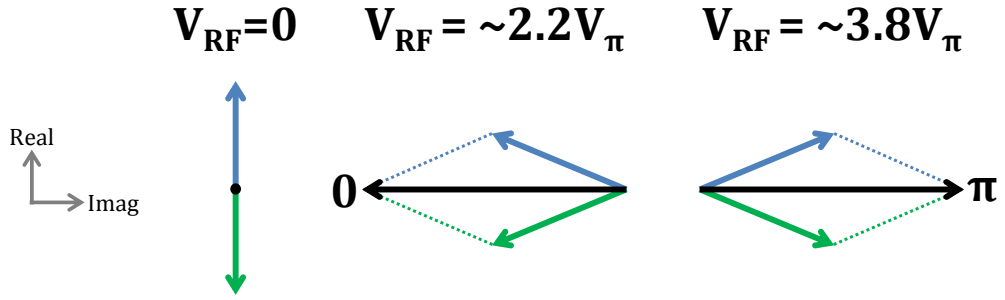Fig. 2.26 – BPSK phasor diagram, $V_{Bias} = 3V_{\pi}$. Blue line = upper arm optical signal, green line = lower arm optical signal, and black line = output.

2.3.3   IQ Modulator

Generating more advanced modulation formats, such as QPSK and QAM, requires the use of nested MZMs called IQ modulators. As mentioned previously, QPSK is a phase modulated format similar to BPSK, except that it has four constellation points $(0, \pi/2, \pi, 3\pi/2)$ compared to BPSK's two $(0, \pi)$. QPSK is a higher level modulation format and its use in optical networks has become increasingly common due to its higher spectral efficiency when compared to BPSK. A comparison of their constellation diagrams is show in Fig. 2.27. From these constellations we can see that QPSK can be thought of as the combination of two BPSK signals which are $\pi/2$ radians out of phase with each other, and this is the method by which the IQ modulation generates QPSK.
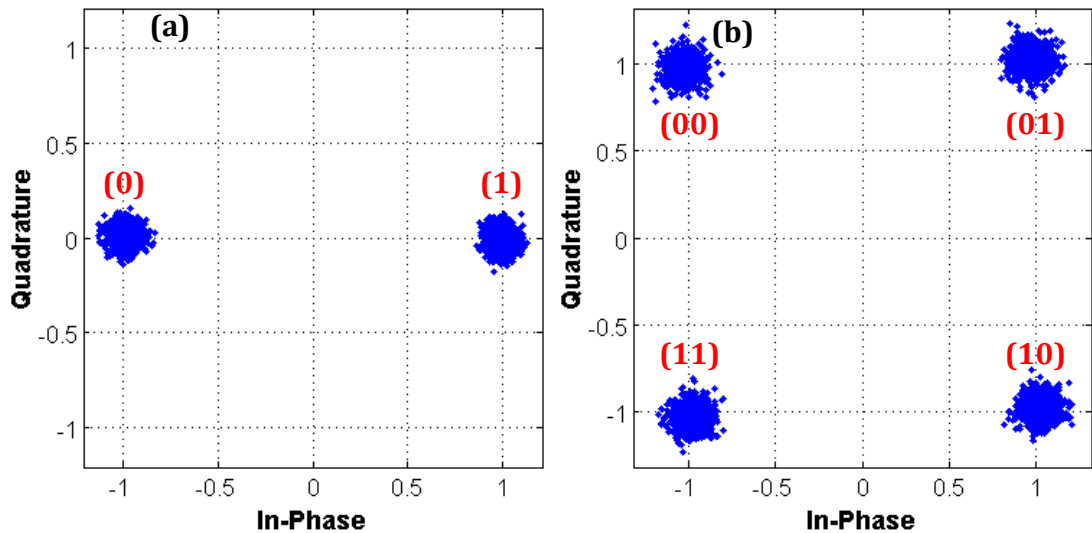

Fig. 2.27 – Constellation diagrams of (a) BPSK and (b) QPSK. Red numbers are binary representations of each phase.

A schematic of an integrated IQ modulator is shown in Fig. 2.28. Two MZM nested in a MZI architecture can be clearly seen along with the inclusion of a

phase shifter in one arm of the MZI, denoted by φ. Each MZM arm is biased to generate BPSK data and driven by a separate RF data signal. The upper arm of the MZI contains a phase control which can then be used to phase shift the upper BPSK signal so that it is π/2 radians out of phase with the lower arm BPSK signal, thus generating a QPSK signal at the output.
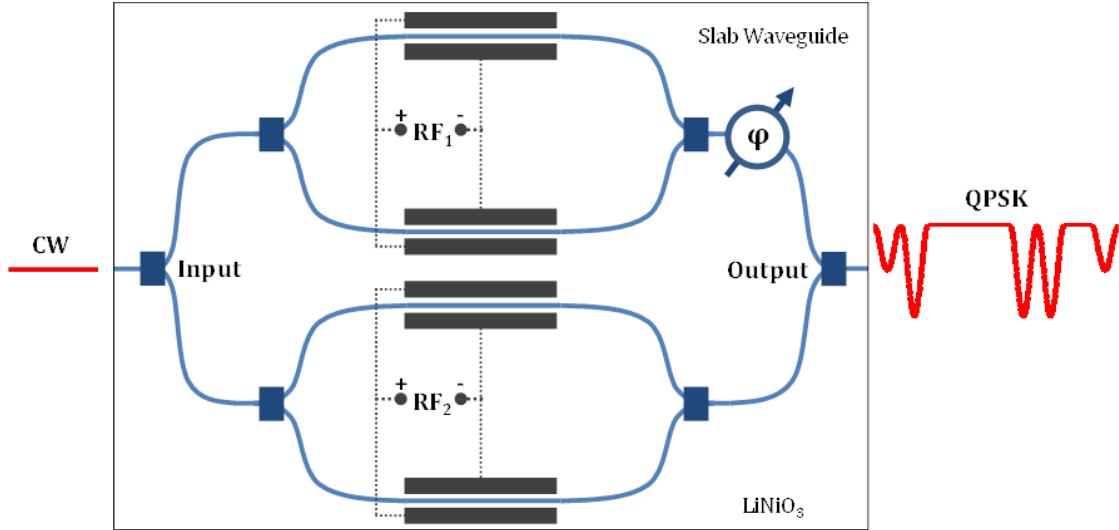

Fig. 2.28 – IQ modulator schematic.

It is important to note that using this type of modulator will produce a residual intensity modulation on top of the QPSK modulation. This residual amplitude modulation is a result of the null that the transfer functions of the modulators in each arm sweeps through when switching phases, as shown in Fig. 2.24.

2.4 Optical Fibre

Optical fibre is the default transport medium in today's optical communication networks. It is an optical waveguide which consists of two layers of dielectric material with different refractive index; the core and the cladding, as shown in Fig. 2.29. A buffer and jacket are commonly included to protect the optical fibre from damage. Typical diameter values for the different layers are also shown.
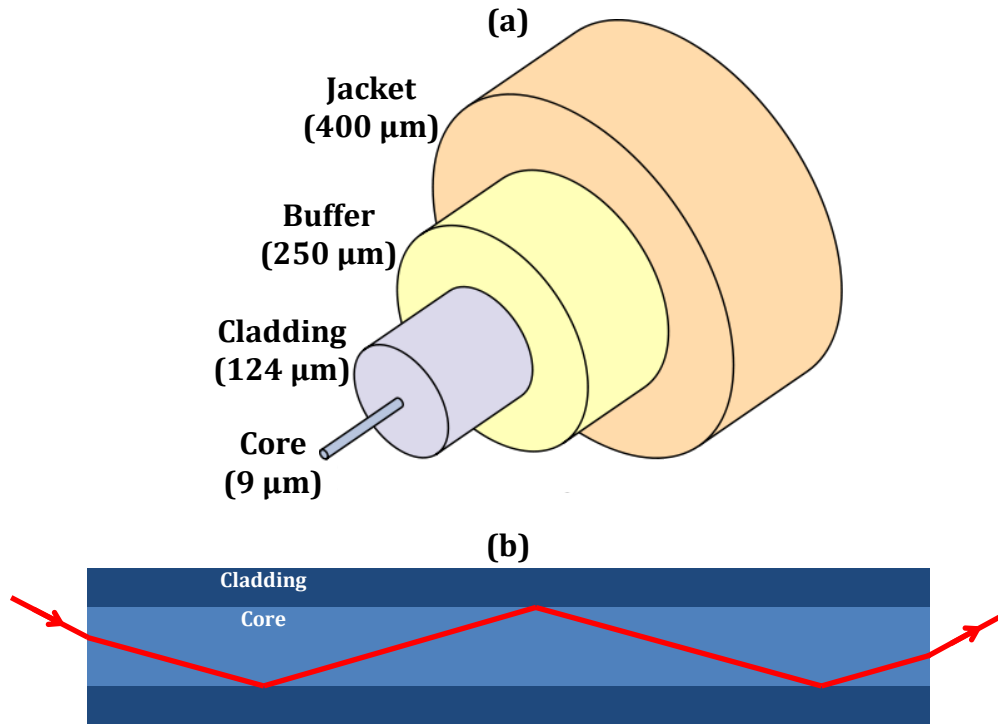
(a)

**Jacket
(400 μm)**

**Buffer
(250 μm)**

**Cladding
(124 μm)**

**Core
(9 μm)**

(b)

Cladding

Core

Fig. 2.29 – (a) SMF cross section [42] (b) Light propagating though SMF

The smaller diameter inner core has a higher refractive index than the outer cladding resulting in total internal reflection which guides any optical signal coupled into the core down its length. Optical fibre is traditionally made of glass silica which has many advantages including its flexibility, low attenuation, low cost of production, and wide optical bandwidth. Single-mode fibre (SMF) is the most common type of fibre in optical networks. Its small diameter core (~9 μm) limits the number of modes supported by the fibre to one, and hence its name.

2.4.1 Attenuation in Optical Fibre

As an optical signal propagates down fibre it loses power due to light absorption and scattering. Minimising this loss allows the optical signal to reach greater distances before optical amplification is required. Loss in fibre is dependent on the wavelength of light injected and a graph of the loss vs. wavelength for different eras is shown in Fig. 2.30. When optical fibre was originally developed it had absorption peaks at certain wavelengths and as such the low loss areas were divided into different bands and labelled. Optical fibre has the lowest loss around 1.55 μm (~193.55 THz) in the 'C' band and as a result this is the most widespread band used. The development of better fibre

technology has reduced the overall loss of fibre, as well as mitigating some of its absorption peaks. A typical value for loss in modern SMF fibre is ~0.2 dB/km.
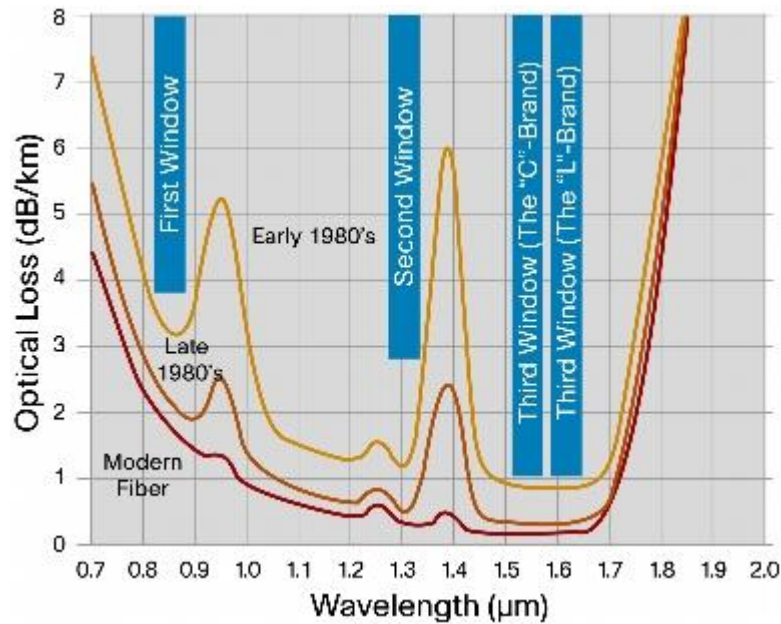

Fig. 2.30 – Fibre loss vs. wavelength. [43]

2.4.2 Dispersion

Dispersion is responsible for the broadening of optical pulses which occurs as they travel down a length of optical fibre. There are two main causes of pulse broadening in single mode fibre; group velocity dispersion (GVD) and polarisation mode dispersion (PMD). Dispersion limits the distance that an optical signal can travel and be demodulated due to the associated distortion of the signal. The pulse broadening can result in interference between adjacent pulse and result in errors at the receiver. An example of dispersion can be seen in Fig. 2.31. A width of an optical pulse at different distances in an optical fibre is shown in Fig. 2.31(a) demonstrating the broadening. Fig. 2.31 shows how interference between pulses due to dispersion can cause errors. The '0' level shown here has risen resulting in a smaller extinction ratio. This smaller extinction ratio will produce more errors at the receiver as the likelihood of a '0' being detected as a '1' is greater.
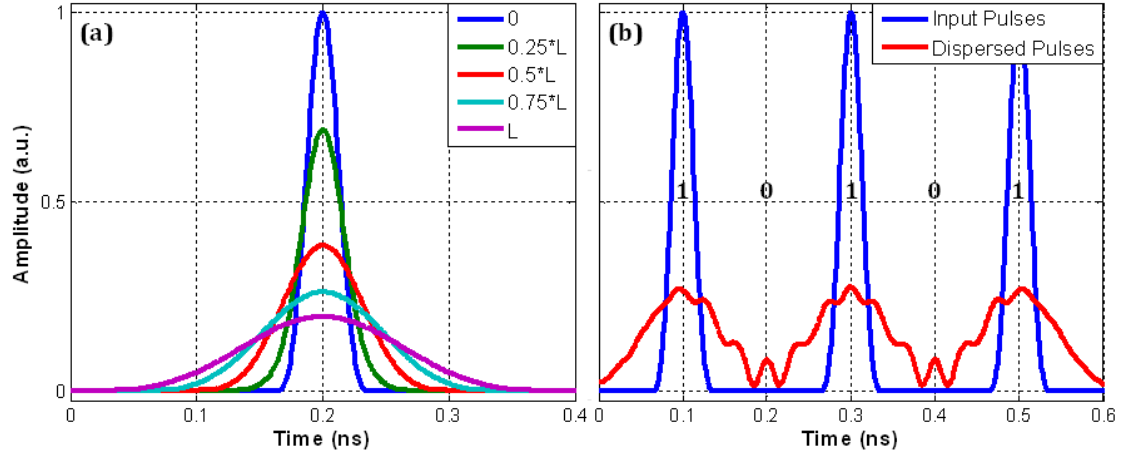
Fig. 2.31 – (a) Dispersion of optical pulse at different points in fibre of length, L (b) Effect of dispersion on decoding data.

If an optical signal propagates through SMF of length, L, a specific spectral component, ω, would arrive at the end of the fibre after a time delay $T = L/v_g$, where v_g is the group velocity, given by:

$$v_g = \left(\frac{d\beta}{d\omega}\right)^{-1} \tag{2-30}$$

By using $\beta = nk_0 = n\omega/c$ in Eq. (2-30), where n is the refractive index of the fibre material, k_0 is the free-space wave vector and c is the speed of light in a vacuum, it can be shown that $v_g = c/n_g$. Here, n_g is the group index given by:

$$n_g = n + \omega\left(\frac{dn}{d\omega}\right) \tag{2-31}$$

Since the group velocity is frequency dependent, different spectral components of an optical pulse will reach the end of the fibre at different times resulting in broadening. If $\Delta\omega$ is the spectral width of the pulse, the broadening is governed by:

$$\Delta T = \frac{dT}{d\omega}\Delta\omega = \frac{d}{d\omega}\left(\frac{L}{v_g}\right)\Delta\omega = L\frac{d^2\beta}{d\omega^2}\Delta\omega = L\beta_2\Delta\omega \tag{2-32}$$

The parameter, $\beta_2 = d^2\beta/d\omega^2$, is known as the GVD parameter and it determines how much a propagating pulse will broaden in an optical fibre.

The spectral bandwidth, $\Delta\omega$, commonly comes from the range of wavelengths, $\Delta\lambda$, emitted from an optical source. By using $\omega = 2\pi c/\lambda$ and $\Delta\omega = (-2\pi c/\lambda^2)\Delta\lambda$ Eq. (2-32) can be rewritten as:

$$\Delta T = \frac{d}{d\lambda}\left(\frac{L}{v_g}\right)\Delta\lambda = DL\Delta\lambda \qquad (2\text{-}33)$$

Where *D* is called the dispersion parameter and is given by:

$$D = \frac{d}{d\lambda}\left(\frac{L}{v_g}\right) = -\frac{2\pi c}{\lambda^2}\beta_2 \qquad (2\text{-}34)$$

and is expressed in units of ps/km.nm.

Polarisation mode dispersion (PMD) arises due to cross-sectional shape of optical fibres. Ideally optical fibre would have a perfect circular cross-sectional but in reality this is not practical to mass produce. Optical fibre generally has an elliptical shape which introduces a birefringence. Birefringence means that an optical signal will travel at different speeds in each axis of the fibre. This is shown in Fig. 2.32.
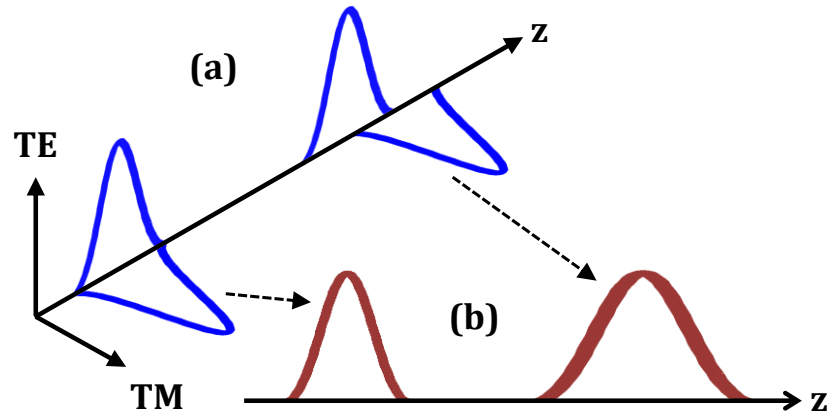

Fig. 2.32 – Polarisation mode dispersion: (a) TE and TM modes (b) Total optical pulse.
Blue = optical pulse in each polarisation mode. Red = Total optical pulse.

The optical pulse at the output will thus be broadened due to the TE and TM polarisation axis propagating along the fibre at different speeds. Dispersion is commonly compensated for using digital signal processing (DSP) combined with the use of the coherent receivers in optical systems.

2.5 Summary

In this chapter we explained the basic concept of modulation including examples of both OOK and PSK formats which are of interest in this thesis. Also discussed in this chapter was the operation of SOAs including their advantages and disadvantages including their limitations for use in all-optical switching

applications. The source of the SOA nonlinearities was detailed including, the operation of Cross-phase modulation, cross-gain modulation, and Four-wave mixing all of which are vital for the experimental work detailed later in this thesis.

The operation of DI was detailed including some of its uses such as filtering and demodulating BPSK data. MZMs, which are the most common type of modulator used, were described in detail including the method used to produce either OOK of PSK data. Lastly, single-mode fibre was discussed briefly including its main properties; absorption and dispersion, two factors which affect optical signals propagating down its length.

3.

Wavelength Dependent Gain Recovery in Nonlinear SOA

This chapter investigates the gain and phase recovery times of a long semiconductor optical amplifier (SOA), in particular the remarkably fast and strongly wavelength-dependent gain recovery of a single long SOA without the aid of any additional components such as an offset filter in detailed. As mentioned in Chapter 2, the main limiting factor of SOAs for their applications in optical switching is their gain and phase recovery times. A shorter recovery time allows for faster switching and thus faster optical switches. This is of importance for the work discussed in Chapter 4, where optical logic gates are used. The four-wave mixing (FWM) efficiency of SOAs, discussed in more detail in Chapter 5, is also dependent on these recovery times which is of importance for the all-optical signal processing techniques demonstrated in Chapter 5 and 6. In this chapter two pump-probe measurement techniques are demonstrated before the wavelength dependent nature of the gain and phase recovery times is investigated [36].

3.1 Introduction

In recent years, SOAs have been of interest for their use as active switching devices in optical networks [44]. Gain and phase recovery times limit the rate at which SOAs can switch high-speed signals. As mentioned in Chapter 2, there is an ultrafast component dependent on intraband effects such as spectral hole burning, carrier heating and subsequent carrier cooling, and a slower,

interband, band-filling process [35, 44, 45], the speed of which is ultimately determined by the current injection.

Many experimental and theoretical investigations of the physics underpinning both the gain and phase dynamics of SOAs have been carried out previously e.g. [46-50]. Despite ultrafast processes in the carrier recovery, the full gain recovery in most SOAs is limited by the slow band-filling process. Various techniques, such as narrow bandpass filtering, the use of a holding beam or employing two SOAs in either a Turbo-Switch arrangement or a "push-pull" interferometer, can improve the switching capability of SOAs [51-57].

A holding beam is a saturating CW beam at a wavelength other than that of the pump or the probe that is incident on the SOA and increases its effective carrier recovery rate [53, 58, 59]. The holding beam depresses the SOA gain, which reduces the gain and phase modulation and this leads to faster recovery times for the gain and phase. This method reduces the band-filling recovery process rather than eliminating it, so patterning effects can become apparent at high data rates. The SOA bias current must be large to allow fast recovery rates to be observed [60].

The Turbo-Switch is an arrangement consisting of two identical or similar SOAs in series separated by a broad optical bandpass filter [51]. A CW probe beam and pump pulses are introduced into the first SOA and cross-gain modulation (XGM) takes place in this SOA. The filter prevents transmission of pump pulses to the second SOA. The signal at the probe wavelength proceeds to the second SOA, where self-gain modulation (SGM) occurs, negating much of the slow tail of the gain and phase response of the first SOA. This technique also gives rise to an overshoot in the gain recovery, which can mitigate patterning effects. Wavelength conversion at 170.4 Gbit/s has been demonstrated using the Turbo-Switch [61].
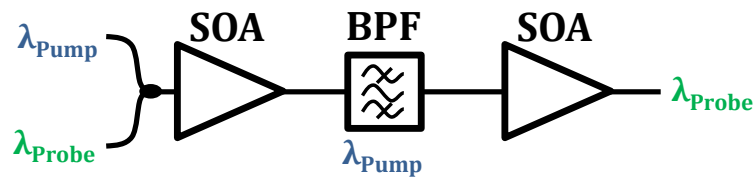

Fig. 3.1 - Turbo-Switch configuration.

SOAs can be placed within push-pull interferometers using a differential switching scheme to increase their switching capability as the switching "window" of the interferometer can be much shorter than the natural carrier recovery time [54]. Mach-Zehnder and Sagnac loop interferometers [62, 63] are frequently employed, although other configurations such as the ultrafast nonlinear interferometer (UNI) are also commonly used [64]. These nonlinear interferometer methods all work on the same principle; a nonlinear element is placed in an interferometric setup, a change in light intensity injected into the interferometer will alter the refractive index / carrier dynamics of the nonlinear medium thus producing a change in the output interference conditions of the interferometer. A SOA based Mach-Zehnder interferometer (MZI) is used in an experiment in the next chapter and is discussed in more detail there.

In this chapter we discuss a multiple quantum well (MQW) SOA that exhibits a highly wavelength-dependent gain response. A predominantly ultrafast gain recovery in a single MQW SOA is observed without employing specialized filters, additional SOAs, or push-pull interferometry. Pump–probe measurements using a 2.5ps pump pulse and a continuous wave (CW) probe demonstrated a gain recovery consisting almost entirely of an ultrafast component followed by a slow overshoot, when the pumping wavelength was to the blue of (shorter than) the probe. However, when the pump wavelength was to the red of (longer than) the probe, slower recovery times without a gain overshoot were measured. We used a simple delay interferometer arrangement to extract gain and phase responses, rather than heterodyne detection [65, 66], and pump and probe wavelengths were varied independently.

The structure of this chapter is as follows: Section 3.2 discusses the experimental details, the results of which are presented in Section 3.3. Section 3.4 details a description of the modelling results which explain the observed effects. The main results of this chapter are then summarised in Section 3.5.

3.2 Experimental Details

In order to measure the gain and phase impulse responses of the SOA, the pump-probe experiment shown schematically in Fig. 3.1 was used. The SOA

employed was a commercially available (CIP Technologies) InGaAsP/InP buried heterostructure MQW SOA with a confinement factor of 0.18, an effective length of 2.2mm and a small signal gain peak at 1565 nm. It had a -3 dB bandwidth of 125nm, a small signal fibre-to-fibre gain of 36 dB and, under typical experimental conditions described here, a fibre-to-fibre saturated gain of 21 dB. It had a saturation input power of -17 dBm. These gain values include input and output coupling losses of 2.3dB and 1.4 dB respectively. A 500 mA bias was used for all the measurements described in this chapter.
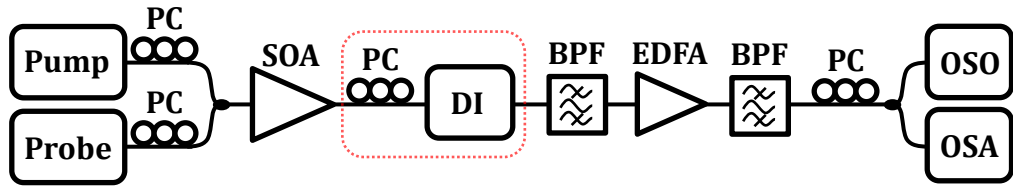

Fig. 3.2 - Experimental setup for measuring the gain and phase responses of the SOA. The delay interferometer (DI), highlighted by the red dashed box, was only present when measuring the phase response. (BPF = bandpass filter, PC = polarisation controller).

The pump was a 2.5 ps pulse clock stream, with -3 dB bandwidth of 1.68 nm, from an actively mode-locked tuneable laser, whose repetition rate was reduced from 10.65 GHz to 665 MHz using an optical modulator. This pump pulse stream was combined with a tuneable CW probe signal using a 3 dB coupler and both signals were injected into the SOA. The pump and probe wavelengths were varied in steps of 5 nm within the ranges $1535 \leq \lambda pump \leq 1570$ nm and $1535 \leq \lambda probe \leq 1580$ nm respectively and the gain and phase evolution curves were measured. The input probe power was fixed at -3.5 dBm and the pump energy per pulse was varied from 3 to 130 fJ in order to maintain a constant amplitude modulation depth of 50% for all wavelengths used. A 4nm band-pass filter after the SOA removed both ASE and pump signals. The output probe signal was passed through an erbium-doped fibre amplifier (EDFA) before being split in a 90:10 coupler. The larger proportion was sent to an optical sampling oscilloscope (OSO) having ~1 ps resolution, and the rest to an optical spectrum analyser (OSA).

The gain response was taken directly using the set-up in Fig. 3.2, without the red highlighted section. To determine the phase evolution, a delay interferometer (DI) with a differential delay of 1 bit period (equal to 94 ps at 10.65 GHz) was inserted after the SOA as shown in Fig. 3.2 (highlighted section).

The phase response was calculated using both the gain response and output temporal waveform from the DI.

In order to extract the phase, it is necessary to employ both the gain data and the delayed interference setup data. The DI has two outputs, only one of which was used. The electric field E_A of the signal from the constructive interference port is given by.

$$E_A = g_0 E_0 e^{i\varphi_0} + g(t)E_0 e^{i\varphi(t)} = g_0 E_0 e^{i\varphi_0}\left(1 + \frac{g(t)e^{i\Delta\varphi(t)}}{g_0}\right) \qquad (3\text{-}1)$$

Where g_0 is the signal field gain of the undisturbed SOA, E_0 is the input field to the SOA, φ_0 is the phase from the undisturbed SOA, and $\varphi(t)$ is the time dependent phase from the SOA at time t after the pump arrival. The detected optical power P_A is proportional to the modulus squared of the electric field (Eq. (2)).

$$P_A \propto E_A{}^* E_A = G_0|E_0|^2\left(1 + \frac{G(t)}{G_0} + 2\sqrt{\frac{G(t)}{G_0}}\cos(\Delta\varphi(t))\right) \qquad (3\text{-}2)$$

Where G_0 is the steady state power gain level, and $G(t)$ is the time-dependent power gain of the SOA. The DI bias was adjusted such that the steady state (fully recovered) level from the port was maximized, and we define T as the ratio of the output power from the DI normalized relative to this steady state level. The value of T from the DI port is given by Eq. (3-3). The multiplication factor of 4 in Eq. (3-3) ensures that T = 1 when $G(t) = G_0$ and $\Delta\varphi(t) = 0$.

$$T = \frac{1}{4}\left(1 + \frac{G(t)}{G_0} + 2\sqrt{\frac{G(t)}{G_0}}\cos(\Delta\varphi(t))\right) \qquad (3\text{-}3)$$

We rearrange Eq. (3-3) to give the phase change as [67]:

$$\Delta\varphi(t) = \cos^{-1}\left(\frac{4T - \frac{G(t)}{G_0} - 1}{2\sqrt{\frac{G(t)}{G_0}}}\right) \qquad (3\text{-}4)$$

Once the gain and phase evolutions were found, the lifetimes of these processes were estimated.

3.2.1   <u>Alternative Measurement Technique</u>

Using a Digital Sampling Oscilloscope (DSO) with three input ports instead of the single input OSO as well as using both output ports of the DI makes it possible to measure the gain and phase evolution curves simultaneously. This technique requires photodiodes and provides lower resolution recovery curves, however, the phase recovery measurements should be more accurate since they are recorded simultaneously with the gain recovery curves. Ideally an OSO with three input ports would be used, combining the advantages of both methods. In this method a DI with a delay of 400ps was used to ensure that the entire phase recovery was measurable as some SOAs can have gain and phase recovery times in excess of the 94 ps delay used in the previous approach.
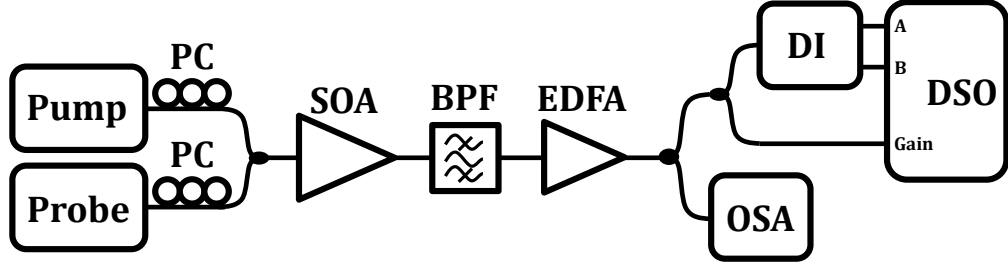
Fig. 3.3 - Alternative gain and phase curve measurement technique.

Eqs. (3-1) and (3-2) describe the electric field, E_A and the power, P_A observed at the constructive port of the DI. We must now also consider the destructive port of the DI where the electric field is given by:

$$E_B = g_0 E_0 e^{i\varphi_0} - g(t)E_0 e^{i\varphi(t)} = g_0 E_0 e^{i\varphi_0}\left(1 - \frac{g(t)e^{i\Delta\varphi(t)}}{g_0}\right) \qquad (3\text{-}5)$$

and subsequently the power is given by:

$$P_B \propto E_B{}^* E_B = G_0|E_0|^2\left(1 + \frac{G(t)}{G_0} - 2\sqrt{\frac{G(t)}{G_0}}\cos(\Delta\varphi(t))\right) \qquad (3\text{-}6)$$

At time $t = 0$, $P_A = 1$, $G(t)/G_0 = 1$, and $\Delta\varphi(t) = 0$:

$$1 = G_0|E_0|^2(1 + 1 + 2) \qquad (3\text{-}7)$$

Therefore:

$$G_0|E_0|^2 = \frac{1}{4} \tag{3-8}$$

Combining Eq. (3-8) with the equations for the power at each port, P_A (Eq.(3-2)) and P_B (Eq. (3-6)) gives:

$$P_A + P_B = \frac{1}{2}\left(1 + \frac{G(t)}{G_0}\right) \tag{3-9}$$

And

$$P_A - P_B = \sqrt{\frac{G(t)}{G_0}}\cos(\Delta\varphi(t)) \tag{3-10}$$

Eq. (3-9) can then be rearranged to give:

$$\frac{G(t)}{G_0} = 2(P_A + P_B) - 1 \tag{3-11}$$

To give the normalised input of the DI, i.e. the normalised gain response. Eq. (3-10) can also be rearranged giving:

$$\Delta\varphi(t) = \cos^{-1}\left[\frac{P_A - P_B}{\sqrt{\frac{G(t)}{G_0}}}\right] \tag{3-12}$$

And substituting Eq. (3-11) into Eq. (3-12) produces:

$$\Delta\varphi(t) = \cos^{-1}\left[\frac{P_A - P_B}{\sqrt{2(P_A + P_B) - 1}}\right] \tag{3-13}$$

Which is the change in phase of the signal injected into the DI and is measured from the output power of each port of the DI, P_A and P_B. The DI bias was adjusted to the linear region of its transfer function, which provides a larger change in intensity at the output of each port for any change in phase. The output of each port was recorded on the DSO along with the directly measured gain response of the SOA. This directly measured gain response was first compared with the calculated gain response, $G(t)/G_0$ from the DI. Once this result was observed to be accurate the change in phase, $\Delta\varphi(t)$, could then be accurately calculated using Eq. (3-13).

There is a frequency response associated with the photodiodes used at the input of the DSO which results in an incorrect representation of the gain and phase responses. As a result these frequency responses were measured and all gain and phase recovery curves measured were adjusted to compensate for this.
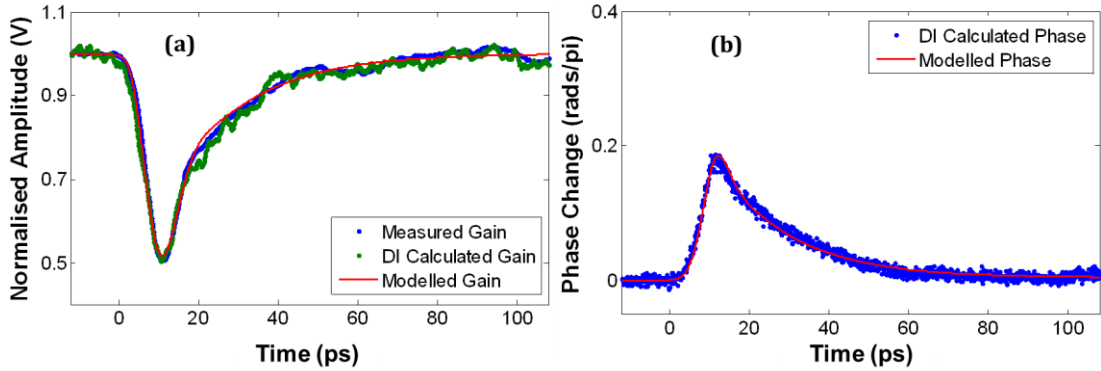

Fig. 3.4 - Alternative technique measurement of (a) Gain response and (b) Phase response.

In Fig. 3.4 above, the gain and phase recovery responses of a quantum dash SOA measured using this alternative technique is shown. This figure demonstrates how the gain calculated from the DI can be compared to the directly measured gain response to ensure the phase response calculated is accurate. A modelled result was fitted to both results and included also.

This experimental method was not used in the results shown in Section 3.3, however, this technique provides some improvements upon the previously mentioned method and has been included as such.

3.3 Experimental Results

Gain and phase data were measured within the wavelength ranges allowed by the available filters and the EDFA. The points in the pump-probe measurements were separated by 0.42 ps. Fig. 3.5(a) and Fig. 3.5(b) show the gain and phase evolution for five pump wavelengths with a fixed probe at 1550 nm. The dashed line in Fig. 3.5(a) marks the steady-state gain level. For this data, the pump pulse energy was within the range of 3 to 60 fJ, and was varied to maintain a constant amplitude modulation depth.

It can be seen from Fig. 3.5(a) that there was a marked increase in the recovery rate and an overshoot when the pump was to the blue of the probe (1535 nm and 1540 nm) compared to when the pump was to the red (1560 to

1570 nm). Measurements were taken for various fixed probe wavelengths (1545 to 1560 nm), always resulting in the same observed qualitative difference in recovery rates between pumping to the blue and to the red. Fig. 3.5(b) shows the phase change recovery for a 1550nm probe and shows that there was a larger ultrafast contribution with a blue-shifted pump compared to a red-shifted pump, although the total recovery time remained approximately the same. This large ultrafast component on the phase recovery is due to the carrier recovery being much faster when pumping to the blue. The blue pump enters and absorption regime in the second half of the SOA, which filters the blue pump and provides carriers for the recovery process. When pumping to the red, however, the pump always sees gain and will not contribute carriers to the recovery process. A more detailed explanation of this process is provided in Section 3.4
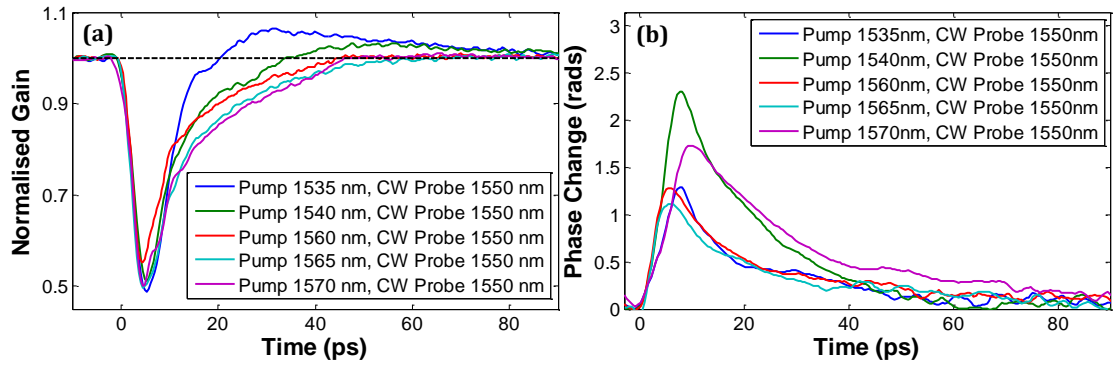
Fig. 3.5 - (a) Normalized gain and (b) phase change as a function of time with a fixed 1550nm probe.

The gain recovery times shown in Fig. 3.6 and Fig. 3.7 are the times for the gain to change from 10% to 90% of the full recovery (10/90 recovery) when compared to the steady state. This method of recovery time estimation avoids errors caused by fluctuations in the gain curve as full recovery is approached. Similarly, the trend in the phase recovery is followed by calculating a 10/90 recovery time, based on the time for the phase to change from 90% to 10% of the maximum phase shift. For all of the data in Fig. 3.6 and Fig. 3.7, we estimate an associated error of approximately ± 2.5 ps, as displayed in the figures. However, error bars are not attached to each point to avoid obscuring the trend in the data.

In Fig. 3.6(a), the 10/90 gain recovery times are plotted as a function of the pump-probe separation for the four fixed probe wavelengths (1545 to 1560 nm) for which there was data for pumping both to the red and to the blue. The zero position on the x-axis in Fig. 3.6(a) corresponds to equal pump and probe wavelengths, with the positive separation representing pumping red and the negative separation representing pumping blue. It is clear from Fig. 3.6(a) that the gain recovery time increases as the pump moves further to the red. In Fig. 3.6(b), the graph of the 10/90 recovery times for both the gain and phase with a 1550 nm fixed probe demonstrates that the phase recovery rate approximately followed the same trend as that of the gain recovery rate, within the limits set by the error bars.
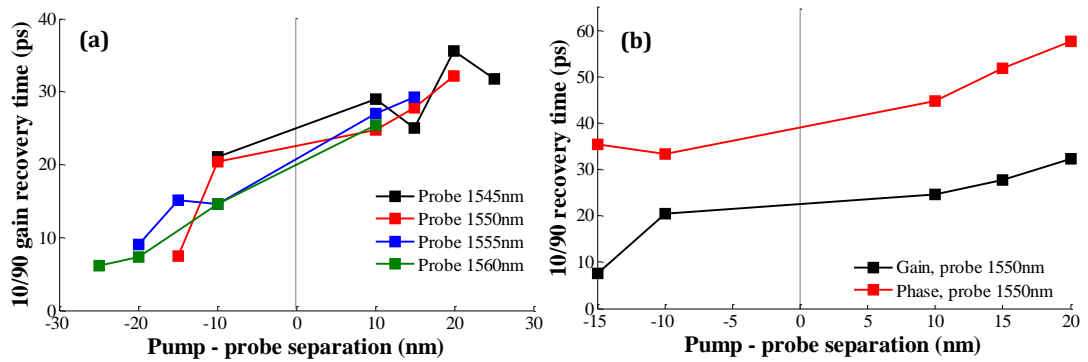
Fig. 3.6 - (a) Gain recovery times for several probe wavelengths and (b) gain and phase recovery times for a fixed 1550nm probe as a function of pump-probe separation. The lines joining the points are a guide for the eye only.

The recovery time as a function of probe wavelength with the pump at a fixed wavelength was also studied. In Fig. 3.7(a), the 10/90 gain response time as a function of the separation between the probe and the small signal gain peak (1565 nm) is shown, with positive and negative separation representing probing at longer and shorter wavelengths respectively. Note that in Fig. 3.7, the pump was always blue-shifted relative to the probe. An approximate parabolic shape to the curves was observed when the pump was between 1535 and 1545 nm, with a minimum located near the 0 nm separation. This demonstrates that the fastest response was achieved when the probe wavelength was close to the gain peak. When the pump was within 1550 to 1555 nm, the curves do not appear to be parabolic and the data was inconclusive.

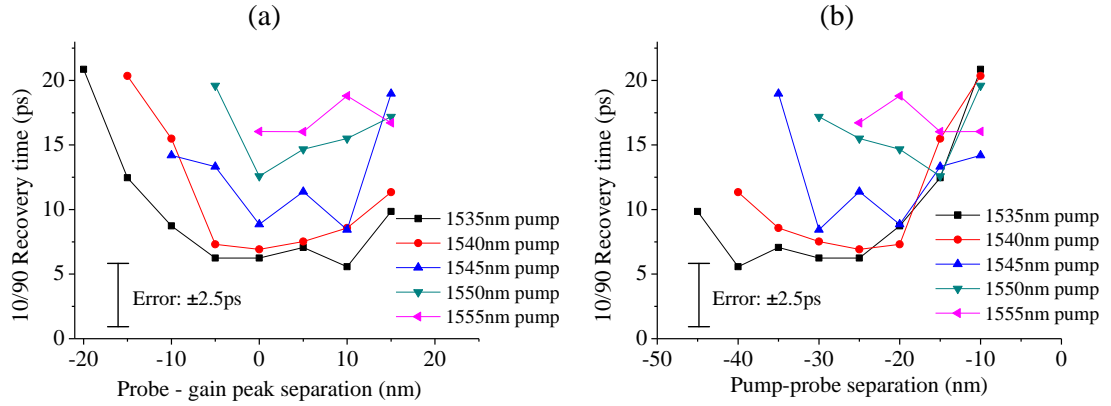(a)   (b)

Fig. 3.7 - 10/90 gain recovery time as a function of (a) probe - gain peak separation and (b) pump - probe separation with the pump fixed in each separate curve. The lines joining the points are a guide for the eye only

In Fig. 3.7(b), the pump wavelength was kept to the blue of the probe and remained fixed for each separate curve while the probe wavelength was incrementally changed. An approximate parabolic shape to the curves was observed in when the pump was within the range 1535 to 1545 nm and indicates that there was an optimum pump-probe separation (20 to 30 nm) for obtaining a fast gain response at a given pump wavelength. However, this was not the case when the pump is within 1550 to 1555nm, where the data was inconclusive.

For several wavelengths of the pump and probe, having the optimum wavelength separation of ~30nm, the gain response was almost completely dominated by a large ultrafast component with just a small band-filling component manifested as an overshoot. The magnitude of the overshoot was low but it persisted for a long time (>60 ps). Some of these gain and phase evolution diagrams are displayed in Fig. 3.6. As may be seen in Fig. 3.9(a), the gain made a 10/90 recovery within 6 to 9 ps and a full recovery within 9 to 20 ps [36]. These were remarkably short recovery times and were substantially shorter than both the recovery time of 100ps for the same SOA when the CW probe was non-saturating and the typical full recovery time of ~60 ps for fast SOAs [47, 48, 68]. The phase recovery time, however, was longer than that of the corresponding gain recovery, although there was a significant ultrafast component to the phase (Fig. 3.8(b)). Also, since the phase recovery took longer than the differential delay of the DI (94 ps), the full phase recovery could not be shown. The pump pulse energies for these results ranged from 60 to 130 fJ.

Using a 1535nm pump and a 1560 nm probe, we observed the same very large fast responses of Fig. 3.5. Increasing modulation depth further gave the same response as in Fig. 3.8(a), but the 10/90 times were larger simply due to the increased depth from which the recovery started.
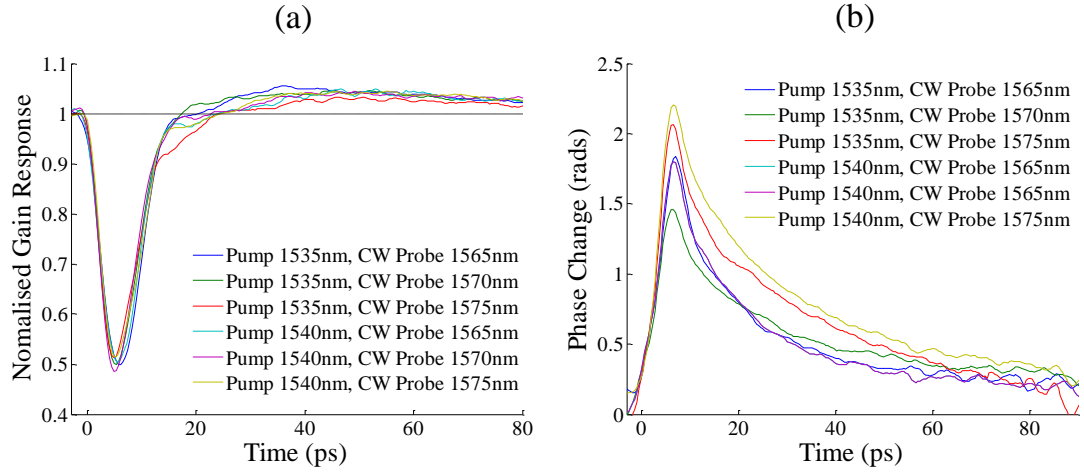
(a)   (b)

Fig. 3.8 - Graphs of (a) gain and (b) phase as a function of time for the optimum pump-probe separation.

The SOA gain spectra when there was a CW input of -3.5 dBm within the wavelength range 1565 to 1575 nm along with the spectrum when there was no input are displayed in Fig. 3.9. The gain at the CW wavelength could not be measured, leading to discontinuities in the spectra. It is clear from Fig. 3.9 that the CW input strongly suppresses the gain and that the gain at wavelengths to the blue of the CW is more strongly suppressed.
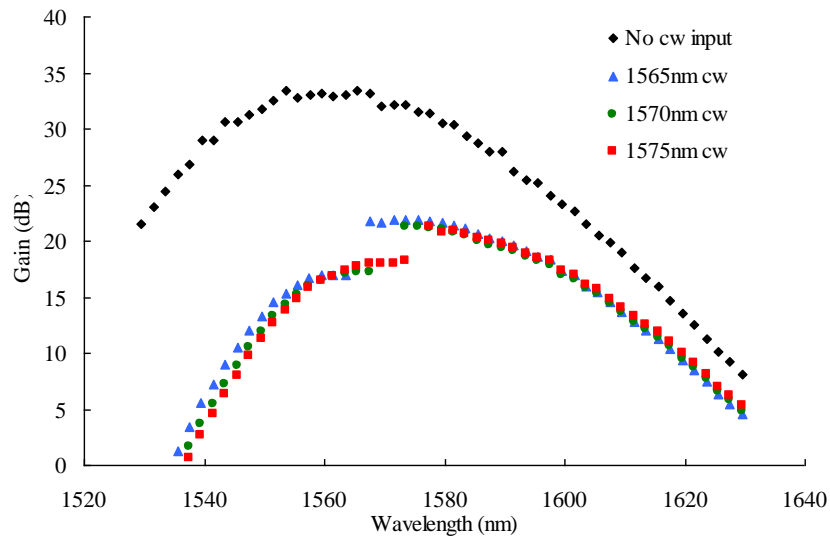
Fig. 3.9 - Gain spectra with a -3.5 dBm CW input whose wavelength is varied, and with no CW input.

3.4 Theory and Modelling

The SOA model used was a multi-section time-domain model of the carrier dynamics within the device, similar to that described in [69], but with some additional features. The temporal and longitudinal variations of both carrier concentration and carrier temperature in response to the pump, probe and ASE powers were calculated using rate equations [69, 70]. The approximation to the gain spectrum introduced in [71] was employed to enable the gain and ASE spectra to be represented efficiently as functions of both time and distance along the SOA.

The experimental device was modelled with CW probe having a power of -3.5 dBm and wavelength 1550 nm and with a pump either to the blue (1535 nm) or to the red (1565 nm). The pump pulse energies at the SOA input facet were 17 fJ and 0.7 fJ respectively, chosen to achieve the same gain compression as the corresponding experimental results (50%). The carrier density variation along the amplifier length with and without the probe is shown in Fig. 3.10. With no input, the forward and backward travelling ASE reached their maximum levels at each end of the amplifier where they caused symmetrical reductions in the carrier density. With the input probe present, the forward travelling power was enhanced and the carrier density beyond the first quarter of the SOA was further progressively reduced, until the modal gain per unit length at the probe wavelength was depressed to near zero by the end of the device (Fig. 3.11(a)). The backward travelling ASE was also reduced but still caused a small dip in the carrier density close to the SOA input.

As a result of the saturation induced by the strong probe, the pump pulses experienced decreasing gain as they travelled along the SOA (Fig. 3.11(a)). With the blue-shifted pump, the gain became negative beyond the midpoint of the SOA and the pulses were attenuated. With the red-shifted pump, on the other hand, the pulses continued to grow up to the end of the SOA, albeit at a reduced rate (Fig. 3.11(b)). In the latter case, smaller pulse energies were sufficient to obtain the same gain compression.

With the blue-shifted pump, the behaviour of the device was similar to that of a Turbo- Switch [51], which employs a filter between two SOAs to block the

onward transmission of the pump. Here, the pump was effectively filtered out in the second section of the SOA because the carrier density was below the transparency point for the pump wavelength. In the first section, where the pump experienced gain, cross-gain modulation (XGM) of the probe by the pump occurred. In the second section, where the pump was absorbed, self-gain modulation (SGM) of the probe signal took place without XGM. Thus, the gain compression in the first section was partially opposed by a gain increase in the second that compensated for the slow band-filling tail in the recovery.
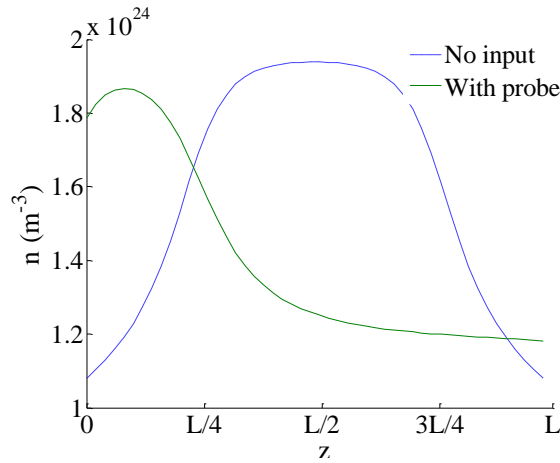
Fig. 3.10 - Carrier density along the length of the SOA. The value of z is normalized relative to L, the length of the SOA active region (L is 2.2mm for this device).
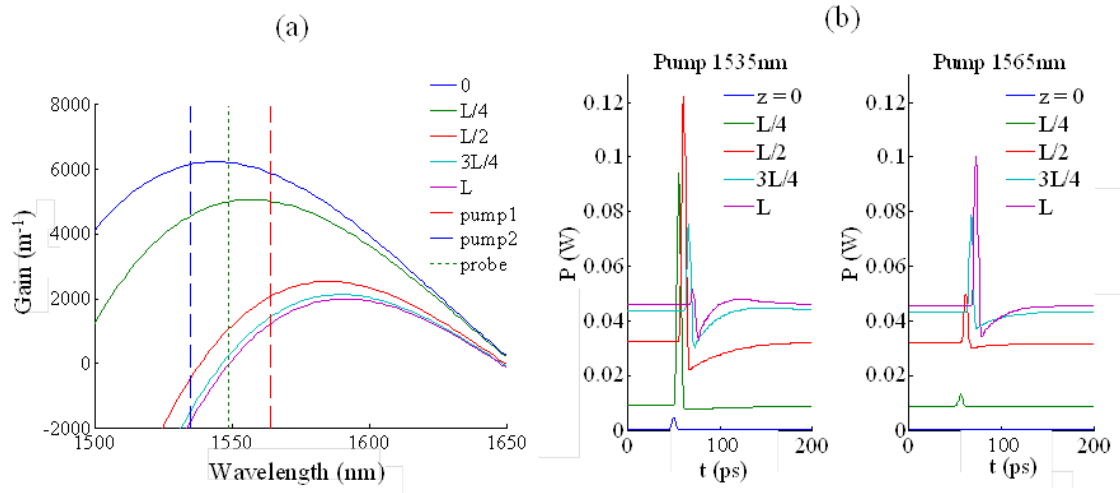
Fig. 3.11 - (a) Gain spectra at various points within the SOA.. The red pump (pump 1, red dashed line) gain is always positive but the blue pump (pump 2, blue dashed line) gain is negative beyond the middle of the SOA. (b) Total signal power (pump + probe) at various points within the SOA. The red pump pulses increase in energy throughout whereas the blue pump pulses lose energy for z > L/2.

When the pump was red-shifted, however, it was not absorbed and therefore gave rise to XGM throughout the entire length of the SOA. Although SGM took place to some extent, it was not sufficient to eliminate the slow tail of

the response. This is illustrated in Fig. 3.12 which shows the evolution of the change in carrier density as a function of time at several points along the active region length. When the pump was blue-shifted, the carrier density change quickly became positive from the centre of the SOA onwards, whereas when the pump was red-shifted, the carrier density change was always negative except at the input facet (where the influence of backward-travelling ASE predominated).

The normalized probe gain was plotted for both pump wavelengths and compared with the corresponding experimental measurements in Fig. 3.13. With the blue-shifted pump, the response resembled that of the Turbo-Switch in showing a rapid recovery succeeded by an overshoot. It is interesting to note that, although the probe amplitude had returned to its original level following the overshoot by t = 200 ps, 125 ps after reaching its minimum value, the carrier density was still far from equilibrium at that time (Fig. 3.12). Clearly the increase in carrier density near the midpoint of the SOA was successfully compensating for the reduction in density in the preceding section.
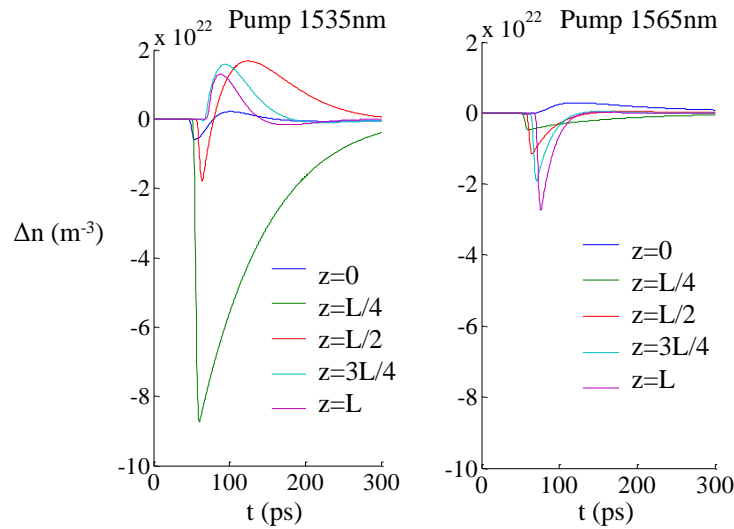
Fig. 3.12 - Carrier density time response at different points within the SOA.
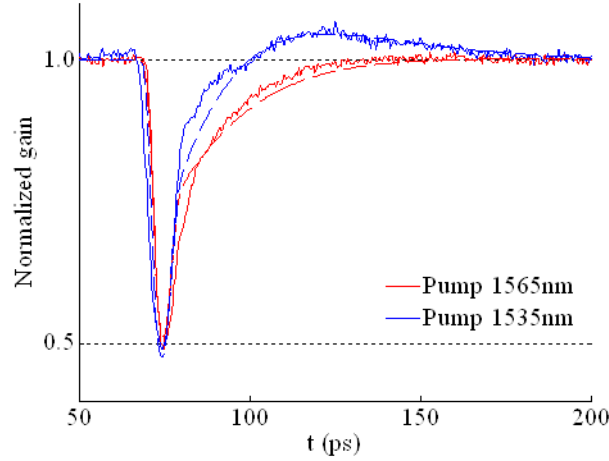
Fig. 3.13 - Comparison between simulated probe gain (dashed lines) and measured gain (solid lines).

Finally, the good agreement between the modelled and measured probe gain gives confidence that the foregoing explanation of the observed behaviour of the device is correct. Further numerical analysis of the variation of the SOA recovery time as a function of pump-probe and probe-gain peak separation is on-going.

3.5 Summary

This chapter investigated the gain and phase dynamics of a long (2.2 mm) non-linear SOA with a large small signal gain. The recovery rates of this device were found to be wavelength dependent and there was a marked difference in the recovery profiles between pumping to the blue and pumping to the red of the CW probe wavelength.

When the pump was blue-shifted and the pump-probe separation was optimized (~20 to 30 nm), gain recovery curves almost entirely dominated by an ultrafast component and accompanied by an overshoot, were observed. Although the measured phase recovery times were slower, they followed the same trend as a function of pump-probe wavelength separation. When the pump was red-shifted, the gain and phase recovery rates were slower, the ultrafast component was reduced and there was no appreciable gain overshoot. Computational modelling of the SOA explained these observations in terms of behaviour similar to that of a Turbo-Switch when pumping to the blue, where the pump was effectively filtered out within the SOA. This work is believed to be

the first demonstration of such an ultrafast gain response from a single SOA, without the use of a filter or additional SOAs. Interestingly, the optimum behaviour of this device was similar to that of an ideal quantum dot (QD) SOA regarding the dominance of the ultrafast component in the gain recovery [31], although a QD SOA generally requires a higher bias current than did this MQW SOA. As in the case of the QD SOA, the phase response was slower than that of the gain. This does mean that an interferometer based switch will not demonstrate the ultrafast response we observe in the gain.

Even though fast gain recovery rates were achievable, their wavelength dependent nature, in conjunction with the slow phase recovery times of this long nonlinear SOA, limit its use for all-optical switching applications. As such these long nonlinear SOAs were not used in the remainder of the work covered in this thesis.

4.

All-Optical Modulation Conversion

This chapter details a novel method of all-optically generating both duobinary (DB) and alternate-mark-inversion (AMI) modulation formats at 42.6 Gbit/s from an input on-off keyed (OOK) signal. The modulation converter consists of two semiconductor optical amplifier (SOA)-based Mach-Zehnder interferometer gates. A detailed SOA model numerically confirms the operational principles and experimental data shows successful AMI and DB conversion at 42.6 Gbit/s.

4.1 Introduction

As engineers strive for novel ways to attain ultimate channel capacity over fibre and maximize the efficient use of network resources, attention has increasingly turned to the use of advanced modulation formats [8]. The pursuit of high-bandwidth transmission in long-haul core networks is dominated by research into phase-shift keying (PSK) and quadrature amplitude modulation (QAM) formats, which have increased spectral efficiency, among other advantages, compared to non-return-to-zero (NRZ) and return-to-zero (RZ) on-off keying (OOK). Research also continues into other advanced modulation formats in network applications where fibre capacity is not the most important criterion. The duobinary (DB) and alternate-mark-inversion (AMI) modulation formats [72-74] can out-perform OOK through the suppression of both linear and nonlinear transmission impairments. For example, NRZ-DB can be utilized for greater tolerance to dispersion [75], and both RZ-AMI and RZ-DB have shown increased nonlinear transmission performance at 42.7 Gbit/s compared with OOK [72]. AMI and DB convey information via binary intensity levels, as in OOK, and the transmission benefits result from auxiliary phase modulation. As a

result, AMI and DB can be received using simple square-law detectors and the additional complexity of coherent receivers is avoided.

It seems likely that future optical networks will incorporate disparate modulation formats depending on the reach and bitrate requirements of its various constituents. Some means of conversion between modulation formats will become an important network function. At high bitrates this conversion process may benefit from an all-optical implementation where savings in energy consumption over optical-electronic-optical approaches may be possible [76]. The all-optical generation of DB and AMI could also be advantageously employed in high-bandwidth transmitters. Kang, *et al* [77], have pointed out that optical signal generation beyond 40 Gbaud is hampered by the stringent requirements on various electronic signal processing components and RF drive amplifiers. They propose the use of optical time-division multiplexing and all-optical modulation converters to push beyond these limits.

This chapter discusses an experimental demonstration of an active all-optical system which translates RZ-OOK to RZ-AMI or RZ-DB at 42.6 Gbit/s [11]. The fast optical nonlinearity is provided by semiconductor optical amplifiers (SOAs) which are capable of providing large phase shifts with relatively small input powers and are particularly attractive in terms of photonic integration potential. In these experiments, four SOAs are hybrid-integrated with planar silica waveguides making a pair of optical gates. This dual-gate scheme offers the potential for further integration, scaling to higher bitrates, and is flexible in its ability to easily change between AMI and DB output formats. Though passive approaches are possible for the all-optical generation of AMI from an OOK input [78], we anticipate that our SOA-based active approach has the potential for 3R regeneration (reshaping, retiming, and reamplification) [79] and the choice of output wavelength is arbitrary.

In Section 4.2 the theory of operation of this all-optical modulation converter is discussed and the expected spectral shapes of both AMI and DB signals are derived. Numerical results for 40 Gbit/s DB generation are shown in Section 4.3. Section 4.4 contains the experimental results for 42.6 Gbit/s and

10.65 Gbit/s all-optical modulation conversion of OOK to both AMI and DB before Section 4.5 provides a brief summary.

4.2 Theory of operation

4.2.1 AMI and DB Generation

In both AMI and DB, data is conveyed via pulse amplitudes, as in on-off-keying (OOK), but with an auxiliary phase modulation encoded onto each. The additional (0,π) phase modulation for AMI and DB is qualitatively different: AMI marks always flip phase regardless of their spacing (Fig. 4.1 (a)), whilst DB marks only flip phase when separated by an odd number of spaces (Fig. 4.1(b)).
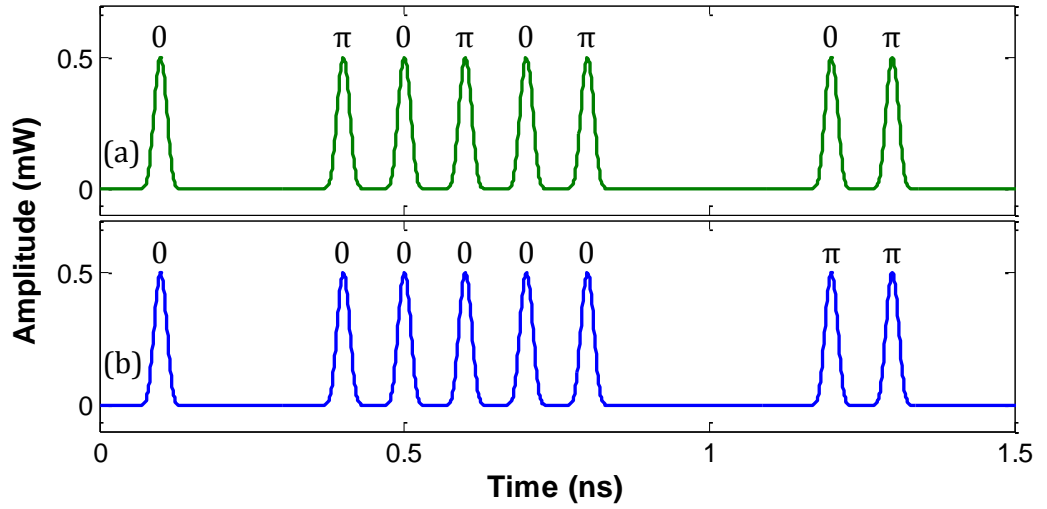
Fig. 4.1 – (a) RZ-AMI modulation format. (b) RZ-DB modulation format. The 0 and π above the pulses represent the auxiliary phase modulation.

The alternate-mark-inversion (AMI) and duobinary (DB) line codes can be generated using delay-and-subtract and delay-and-add operations, respectively [8, 80]. These mathematical operations impress the characteristic auxiliary phase modulation on the pulses but will alter the original binary information, requiring the use of a simple precoding or decoding. The delay-and-subtract and delay-and-add operations are summarized below in Eq. (4-1) and Eq. (4-2) for a binary input signal $x[n] = \{0,1\}$ and output signals $y_{AMI}[n]$ and $y_{DB}[n]$:

$$y_{AMI}[n] = x[n] - x[n-1] \tag{4-1}$$

$$y_{DB}[n] = x[n] + x[n-1] - 1 \tag{4-2}$$

where y_{AMI} and y_{DB} are the AMI and DB sequences, respectively. Both output sequences use the symbols $\{-1, 0, +1\}$. The -1 has been included in Eq. (4-2) to force the mean signal value to zero, consistent with optical DB signals used in practice. An example of an RZ-OOK data can be seen in Fig. 4.2(a) and the same data delayed by one bit is shown Fig. 4.2(b). When the delayed data is subtracted from the original data, the RZ-AMI signal shown in Fig. 4.2(c) is obtained. The -1 value on the vertical axis, shown in Fig. 4.2(c) and Fig. 4.3(c), denotes a π change in phase not a negative amplitude. In Fig. 4.2(c), the phase of every mark is inverted with respect to the previous one, a characteristic of AMI. The data encoded on the AMI signal is also visibly different from the original OOK data, demonstrating the need for data precoding/decoding when using this technique.
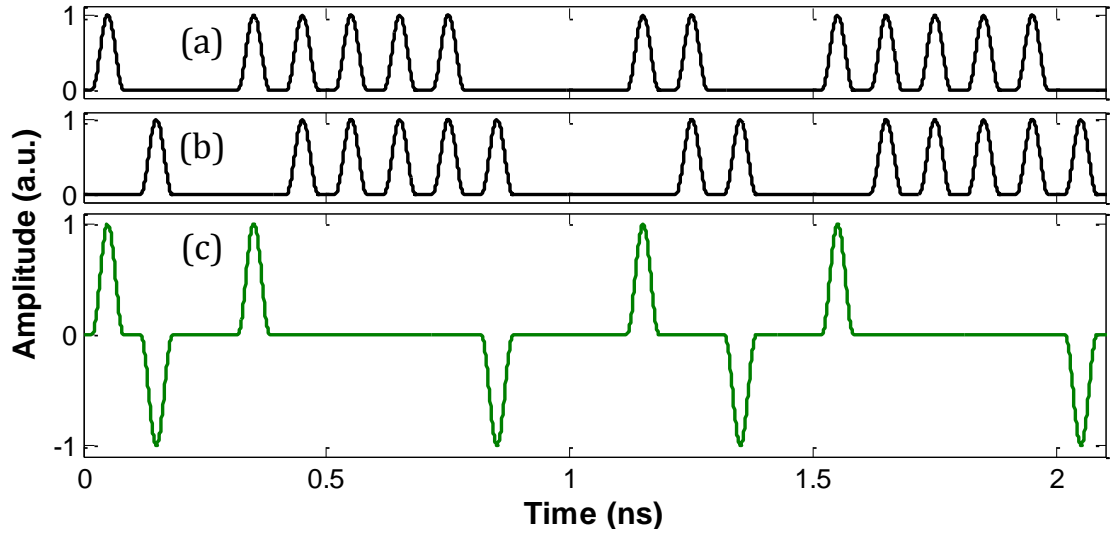
Fig. 4.2 – AMI generation: (a) Data, (b) Data delayed by 1 bit, (c) Alternate Mark Inversion

It should also be noted from Eq. (4-2) that DB can be calculated using a subtraction operation as follows:

$$
\begin{aligned}
y_{DB}[n] &= x[n] - (1 - x[n-1]) \\
&= x[n] - \overline{x}[n-1]
\end{aligned}
\tag{4-3}
$$

where the -1 term in Eq. (4-2) has been utilized to invert the delayed input signal. Later, it will be shown that Eq. (4-3) is crucial for producing a high-quality signal with the all-optical gates. An example of this delay-and-subtract method for RZ-DB can be seen in Fig. 4.3. The RZ-OOK data in Fig. 4.3(b) is inverted before being delayed by one bit as required by Eq. (4-3). In DB, the

mark only inverts its phase when there are an odd number of zeros between it and the previous mark, as shown in Fig. 4.3(c). As with AMI, data precoding or decoding is required to restore the original binary information.
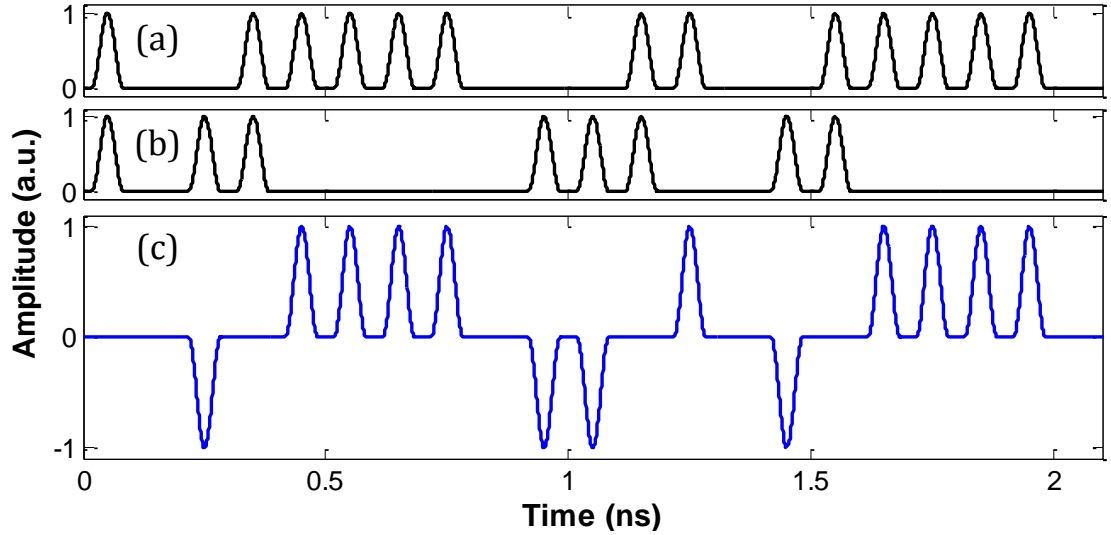
Fig. 4.3 – DB generation: (a) Data, (b) $\overline{\text{Data}}$ delayed by 1 bit, (c) Duobinary.

4.2.2   All-Optical Logic Gates

The all-optical modulation conversion technique detailed in this chapter uses two all-optical logic gates; a dual output all-optical wavelength (DOWC) converter and an all-optical XOR, both of which incorporate SOA-based-Mach-Zehnder Interferometers in their architecture. The SOA-based-MZI is a normal integrated planar silica MZI with the addition of an identical SOA to each of the interferometer arms as shown in Fig. 4.4. The SOA-based-MZI is in a well know push-pull configuration [81, 82] which allows short switching windows, but will not eliminate patterning. It has three inputs: a probe at wavelength λ_{Probe} (a pulse probes is required for this experiment), 'push' data pulse stream and a 'pull' data pulse stream both at wavelength λ_{Data}. The probe pulses are injected into both SOAs, however the push pulse only enter SOA 1 and the pull pulses only enter SOA 2. The push and pull are identical pulsed data streams with pull delayed by τ with respect to the push as shown in Fig. 4.4.
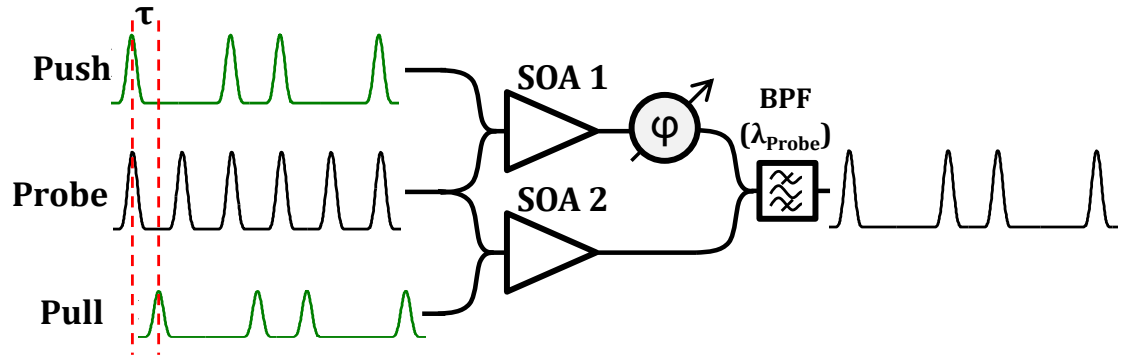
Fig. 4.4 – SOA based MZI. Phase shifter = φ, band-pass filer = BPF. Different pulse colours represent different wavelengths.

Initially, only the probe is injected into both SOAs with the push and pull disabled. The probe pulses are then split in a 50:50 (3 dB) splitter before travelling through the SOAs in each matched arm of the MZI. At the output port they are destructively interfered by adjusting the phase shifter, denoted by φ in Fig. 4.4, to produce no output pulses from the SOA-based-MZI. Once a push pulse is injected, SOA 1 will saturate causing the probe pulse, injected simultaneously, to undergo XGM and XPM. This alters the interference conditions between the probe pulses from SOA 1 and SOA 2 and will open a 'switching window' resulting in a probe pulse visible at the output port. At time τ later, the pull pulse enters SOA 2 and closes the 'switching window' provided the pull pulses input power is adjusted to overlap the gain and phase recovery of SOA 2 with that of SOA 1 as shown in Fig. 4.5.
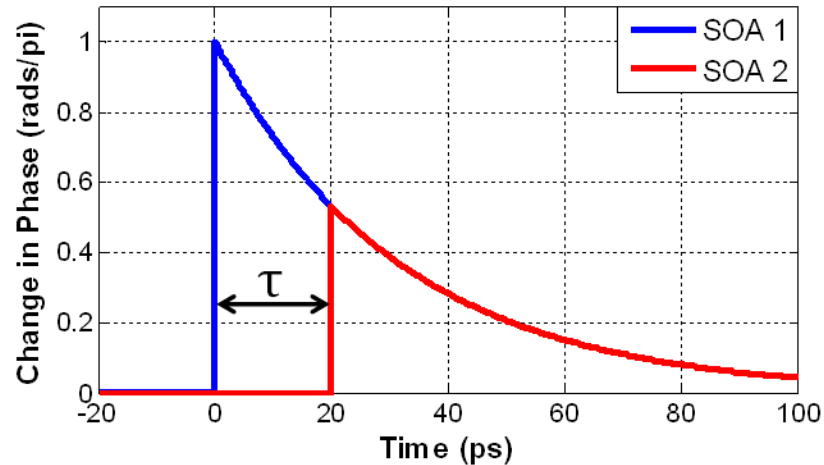
Fig. 4.5 – Phase dynamics of SOA 1 and SOA 2, due to injected 'push' and 'pull' pulses in the SOA-based-MZI.

By adjusting the pull time delay, τ, short switching windows (< 20 ps) and as a result high bitrates (> 40 Gbit/s) can be achieved with this technique. The

main limitation of the SOA-based-MZI is the patterning resulting from the carrier recovery time of SOAs. If another pulse is injected into the SOA before its gain has recovered, that pulse will experience a reduced gain and as a result less amplification, known as patterning. Patterning was discussed in more detail in Chapter 2 and there have been various techniques developed to overcome patterning such as using complementary data inputs to the SOAs [83] or the use of an asymmetrical MZI [84].

Inverted data ($\overline{\text{data}}$) is required to produce the DB modulation format in this scheme. As such, a method of producing both data and $\overline{\text{data}}$ simultaneously is required. This can be accomplished using a dual output wavelength converter (DOWC), which is essentially a SOA-based-MZI with two output ports, as shown in Fig. 4.6. This device is capable of producing either data and data, for AMI, or data and $\overline{\text{data}}$, for DB.
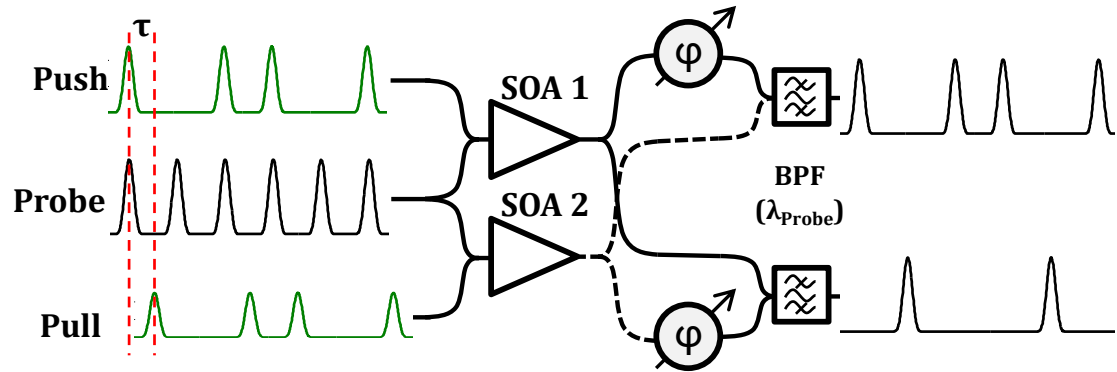
Fig. 4.6 – Dual output wavelength converter. Please note, the dotted line output of SOA 2 does not interfere with the solid line output of SOA 1, their paths merely overlap.

Each SOA output in the MZI is split using 50:50 (3 dB) couplers. Using a second phase shifter (φ in Fig. 4.6) the interference conditions in the bottom port can be independently adjusted to produce either data or $\overline{\text{data}}$. The top port produces the wavelength converted RZ-OOK signal (data) as usual, however, to produce the inverted RZ-OOK signal ($\overline{\text{data}}$) the bottom phase shifter is adjusted to constructively interfere the output probe pulses, when no push and pull are present. The probe pulses will then destructively interfere during the 'switching window', suppressing them and thus producing an inverted RZ data stream at the probe wavelength, λ_{Probe}, as shown in Fig. 4.6. The pulsed probe is required to produce inverted RZ-OOK data, a CW probe would result in an NRZ-OOK signal which was the inverse of the input RZ-OOK data.

We now have the required input both for AMI and DB given by equations (4-1) to (4-3). Next, an all-optical gate capable of calculating sums and differences is utilized to generate the DB and AMI outputs. Such a gate can be realized using an all-optical XOR logic gate and is shown in Fig. 4.7 with three inputs (data inputs A and B, and a probe input) and a pair of output ports (Δ and Σ). The XOR gate is based on the architecture of the SOA-based-MZI except both data inputs are now injected into both arms of the MZI, creating their own push and pull signals for the switching window. With no data input to the MZI, the phase shifter is adjusted such that the output probe pulses constructively interferes at the Σ port and destructively interferes at the Δ port.
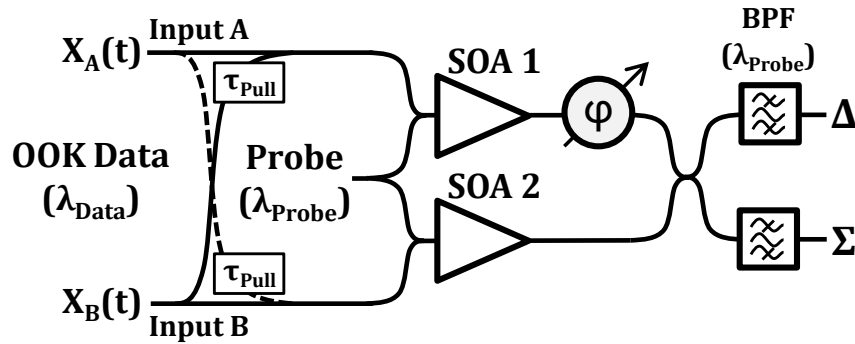
Fig. 4.7 - All-optical logic gate with XOR-type architecture. BPF = Band-pass filter, φ = phase shifter, τ_{Pull} = fixed optical delay.

A pulse injected only into input port A, denoted as input state (1, 0), is split between SOA1 and SOA2. As mentioned above, the "push" pulse first saturates SOA1, and due to both cross-gain (XGM) and cross-phase modulation (XPM), the interference conditions for the probe are changed, opening a switching window for λ_{probe} at the output ports. The other pulse copy is delayed by τ_{pull} and this "pull" pulse enters SOA2 and closes the switching window. If a pulse enters input A and B simultaneously both SOAs will produce identical switching windows and thus the interference conditions at the output will not change, producing no pulse.

The logical operation of this gate can be predicted using a transfer function analysis to derive the relative amplitude and phase relationships between the various MZI output states. It is straightforward to show that the transfer functions describing the outputs from the Δ and Σ ports of the interferometer are given by:

$$H_\Delta = \frac{1}{2}\left(e^{-\frac{\varphi_1}{\alpha}}e^{i\varphi_1} - e^{-\frac{\varphi_2}{\alpha}}e^{i\varphi_2}\right) \tag{4-4}$$

$$H_\Sigma = \frac{1}{2}\left(e^{-\frac{\varphi_1}{\alpha}}e^{i\varphi_1} + e^{-\frac{\varphi_2}{\alpha}}e^{i\varphi_2}\right) \tag{4-5}$$

where the XPM shifts for SOA1 and SOA2 are given by φ_1 and φ_2, respectively. The XGM on the probe is captured via the α-factor within exponential terms; these exponentials decrease with increasingly large XPM shifts, i.e. both α and φ are positive-valued. In the derivation of Eqs. (4-4) and (4-5), the unsaturated gains through the SOAs have been normalized to unity.

The logical output states from the XOR gate, as electric field quantities, can be calculated using Eqs. (4-4) and (4-5) and some representative values are summarized below in **Table 4.1**. The binary values in the "A" and "B" columns indicate whether or not a pulse is injected into Input A and Input B, respectively. The second row in **Table 4.1**, for example, is calculated assuming that a pulse enters Input A only, and corresponds to $\varphi_1 > 0$ and $\varphi_2 = 0$. The pull inputs in Fig. 4.7 are neglected for the sake of clarity in this analysis.

Table 4.1 - All-Optical Gate Output Logic

		$\alpha = \infty$	$\varphi = \pi$	$\alpha = 5$	$\varphi = \pi/2$
A	**B**	**H_Σ**	**H_Δ**	**H_Σ**	**H_Δ**
0	0	+1	0	+1	0
1	0	0	-1	$0.62e^{i0.2\pi}$	$0.62e^{i0.8\pi}$
0	1	0	+1	$0.62e^{i0.2\pi}$	$0.62e^{-i0.2\pi}$
1	1	-1	0	$0.73e^{i0.5\pi}$	0

Two sets of calculations are shown in **Table 4.1**. The first group (columns 3 and 4) corresponds to an infinite α-factor and a possible XPM shift of π (indicated by φ in the table), and the second group (columns 5 and 6) shows the results for a representative α-factor of 5 and potential XPM shift of $\pi/2$. The first group of calculations suggests that the XOR output ports operate in the following way:

$$H_\Delta \propto B - A \tag{4-6}$$

$$H_\Sigma \propto 1 - (A + B) \tag{4-7}$$

Eqs. (4-6) and (4-7) correspond to Eqs. (4-1) and (4-2) demonstrating that AMI and DB can be obtained at the Δ and Σ ports, respectively. However, the calculations shown in the first group (columns 3 and 4) assume that the SOAs exhibit zero XGM (the infinite α-factor) and have exact π radian XPM shifts. The infinite α-factor assumption is unrealistic in practice, and π phase shifts generally become increasingly difficult at high bit-rates.

The second group of data (columns 5 and 6) represent more realistic calculations, where XGM is included and the XPM shift is somewhat smaller. In this data set, Eq. (4-7) is clearly no longer correct for the Σ port. The spaces are very poorly extinguished and the two mark vectors are unequal in amplitude and are not separated by π radians. However, Eq. (4-6) still holds true for the Δ output port, as good zeros are obtained and the two mark vectors are equal in amplitude and separated by π radians. The only consequence of the XGM and smaller XPM shift is that the output mark amplitude is reduced.

The key conclusions here are that the Δ output port is much more appealing for logical operations, and when using this port the only criterion for perfect phase inversions on the output pulses is symmetrical XPM shifts in the two SOAs. We also expect better exploitation of the MZI's regenerative abilities [79, 85] using the Δ port. We conclude that the difference calculation at the Δ port must be used for both AMI and DB generation as consistent with Eqs. (4-1) and (4-3) given above. It has been previously demonstrated via numerical modelling that the Δ port can generate a high-quality AMI output signal [82].

4.2.3   AMI and DB Spectral Shape

Since the binary information is encoded onto the intensity of the signal in both alternate-mark-inversion (AMI) and duobinary (DB) formats, only a simple square law detector is required to demodulate the data. This means that differentiating AMI and DB from OOK data, in the time domain, can be difficult without the use of a phase sensitive receiver such as coherent receiver or delay interferometer (DI). Due to the auxiliary phase information on both modulation formats, however, both AMI and DB have distinct optical spectrum which can be

used to verify the correct operation of this all-optical modulation conversion technique.

Here we will derive the expected spectral shapes of AMI and duobinary DB baseband output signals. Key features from these spectra can be compared with the measured optical spectra to indicate the output modulation format. The output signal, $Y(t)$, from the XOR gate can be represented as a comb of identical pulses each with temporal shape $U(t)$.

This comb is modulated by a three-level discrete message $y[n]$ of length M:

$$Y(t) \approx \sum_{n=0}^{M-1} y[n] \cdot U(t - nT) \tag{4-8}$$

where T is the bit period and $y[n]$ is zero for $n < 0$ and $n > M\text{-}1$. The Fourier Transform of $Y(t)$ can be written as

$$\begin{aligned}
\tilde{Y}(2\pi f) &= \int_{-\infty}^{\infty} Y(t) e^{-i2\pi f t} dt \\
&= \sum_{n} y[n] \int_{-\infty}^{\infty} U(t - nT) e^{-i2\pi f t} dt \\
&= \tilde{U}(2\pi f) \sum_{n} y[n] e^{-i2\pi f nT} \\
&= \tilde{U}(2\pi f) \cdot \tilde{y}(2\pi f T)
\end{aligned} \tag{4-9}$$

where i is the imaginary number $\sqrt{-1}$ and f is the frequency. The time-shift property of the Fourier Transform has been utilized on $U(t)$ to generate the pulse spectrum, $\tilde{U}(2\pi f)$, and $\tilde{y}(2\pi f T)$ is the Discrete-Time Fourier Transform (DTFT) of the message $y[n]$. Equation (4-9) indicates how the pulse spectrum is modified by the modulation spectrum.

The spectral envelope of the pulse is the same for AMI and DB, and it is the transform of the message, $y[n]$, that changes. We first consider Eq. (4-1) from section 4.2.1, which describes AMI:

$$y_{AMI}[n] = \begin{cases} x[n] - x[n-1], & 0 \le n \le M-1 \\ 0, & otherwise \end{cases} \tag{4-10}$$

where $x[n]$ is the binary (OOK) message being converted to AMI. We denote the DTFT of $x[n]$ as $\tilde{x}(2\pi fT)$ and using the time-shift property of the DTFT, we can write the transform of Eq. (4-10) as

$$\begin{aligned}
\tilde{y}_{AMI}(2\pi fT) &= \tilde{x}(2\pi fT) \cdot \left(1 - e^{-i2\pi ft}\right) \\
&= 2i \cdot \tilde{x}(2\pi fT) \cdot e^{-i\pi ft} \sin(\pi fT)
\end{aligned}$$

(4-11)

This result indicates that on top of the OOK spectral shape due to the input signal modulation, $\tilde{x}(2\pi fT)$, the AMI coding will impress in amplitude a $\sin(\pi fT)$ signature characteristic. This sine term suppresses the DC and modulation harmonic components ($f = 0, \pm B, \pm 2B, \dots$) on the AMI signal, as shown in Fig. 4.8.
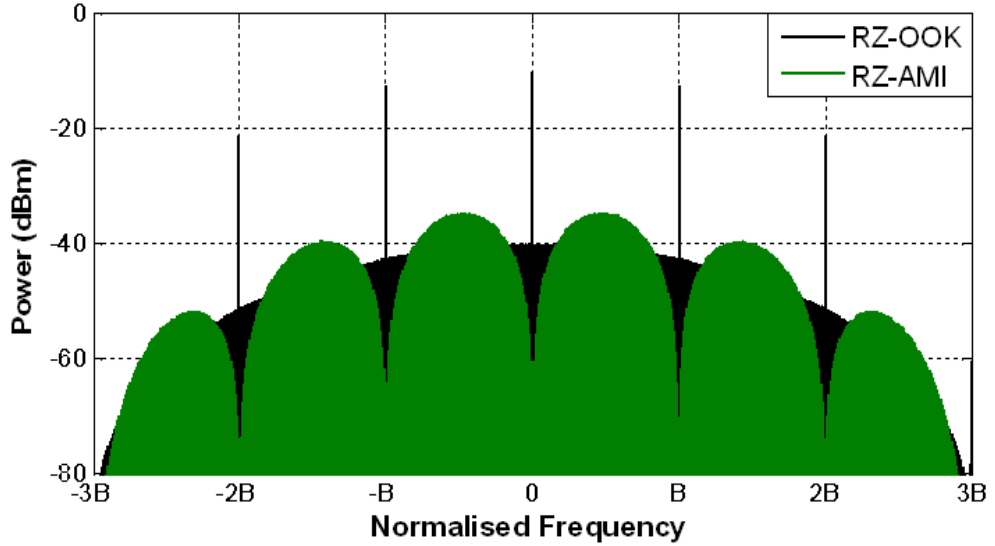
Fig. 4.8 – OOK and AMI spectrum comparison. Frequency axis is normalised to the bitrate, *B*.

The DB line coding is given by Eq. (4-2), assuming that the three-level discrete signal is centred at zero (note the AMI signal is also centred at zero)

$$y_{DB}[n] = \begin{cases} x[n] + x[n-1] - 1, & 0 \le n \le M-1 \\ 0, & otherwise \end{cases}$$

(4-12)

and the DTFT of Eq. (4-12) produces

$$\tilde{y}_{DB} = 2.\left[\sum_{n=0}^{M-1} x[n]e^{-i2\pi fnT}\right] \cdot e^{-i\pi ft} \cdot \cos(\pi fT) - \sum_{n=0}^{M-1} e^{-i2\pi fnT}$$

(4-13)

where the transform for $x[n]$ has been written explicitly. The first term on the right hand side of Eq. (4-13) contains a $\cos(\pi fT)$ which modifies the amplitude of the DB spectrum, shown in Fig. 4.9, in a similar way to the sine term for AMI

in Eq. (4-11). Frequency components at $f = \pm 0.5, \pm 1.5B, \pm 2.5B, \dots$ are supressed due to this cosine term.
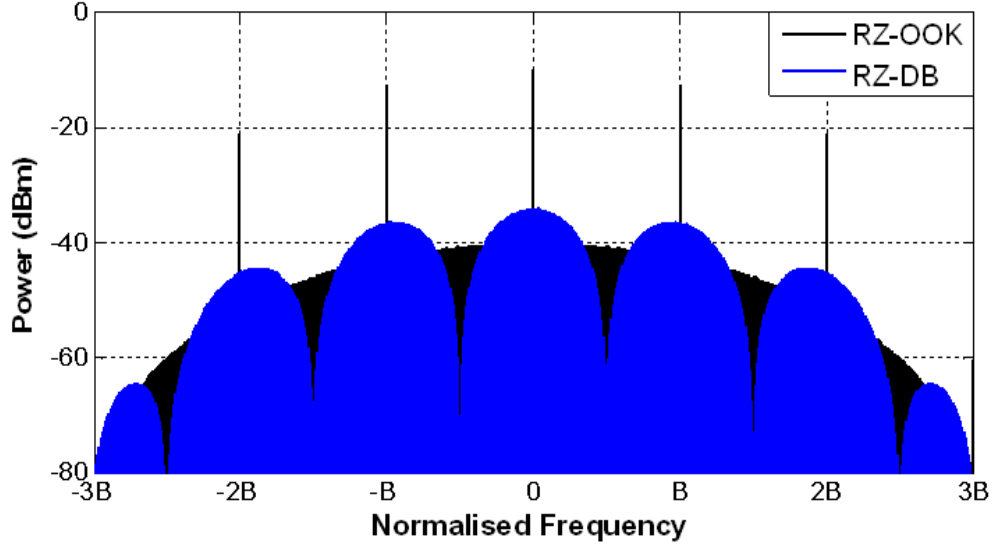
Fig. 4.9 – DB spectrum. Frequency axis is normalised to the bitrate, *B*.

The second term on the right-hand side of Eq. (4-13) produces DC and modulation harmonic suppression for the DB signal also shown in Fig. 4.9. The DC suppression can be seen by calculating $\tilde{y}(2\pi fT = 0)$:

$$
\begin{aligned}
\tilde{y}_{DB}(f = 0) &= 2 \cdot \sum_{n=0}^{M-1} x[n] - \sum_{n=0}^{M-1} 1 \\
&= 2\frac{M}{2} - M \\
&= 0
\end{aligned}
\tag{4-14}
$$

where we have assumed that *x*[*n*] is a random signal with an equal number of marks and spaces. A similar result applies at the modulation harmonics where $f = 0, \pm B, \pm 2B, \dots$ Note that the suppressed DC components in Eqs. (4-11) and (4-13) correspond with the carrier in an optically modulated signal.

4.3 Numerical Modelling of 40 Gbit/s Duobinary Generation

This sections details the modelling results for the operation of the all-optical XOR gate as an OOK to DB modulation converter. The simulations and numerical model were performed and developed by a colleague, Dr. James M. Dailey. Similar modelling results for AMI modulation conversion have been previously been reported in [82]. The computer model is based on a travelling-

wave rate-equation analysis and the coupled partial differential equations are solved using a fourth-order Runge-Kutta algorithm. The XGM and XPM on the probe are captured via gain and refractive index changes calculated using a density matrix approach, eliminating the need for an α-factor approximation such as that used above. Ultrafast gain saturation and recovery are captured through carrier heating calculations. Further details on the numerical model can be found in [86], and similar device parameters are used here.

The 2mm SOAs are each injected with 350 mA of current producing a mean saturated gain of 19 dB peaking at ∼ 1552 nm. The saturated gain and phase recovery times (10% to 90%) are ∼ 15 ps and 24 ps, respectively, and so we expect pattern effects to be minimized in these simulations. This will allow the operation of the gate to be more clearly seen, and the impact of carrier density recovery times on the results will be discussed in further detail in subsequent sections. The 1548.51 nm OOK input signal into port A is the logical inverse of a standard 2^7-1 pseudorandom binary sequence (PRBS) and the input to port B is the non-inverted PRBS sequence delayed by one bit period. The 2 ps push and pull-pulses have peak powers of 1 mW and 0.3 mW, respectively, at the SOA inputs. The pull-pulse delay, τ_{pull}, is set to 8 ps. A 100 μW CW signal injected into each SOA at 1550.92 nm is used as the probe. The output power is calculated at port Δ and shown in Fig. 4.10 (bottom trace) along with the input signals into ports A (top trace) and B (middle trace).
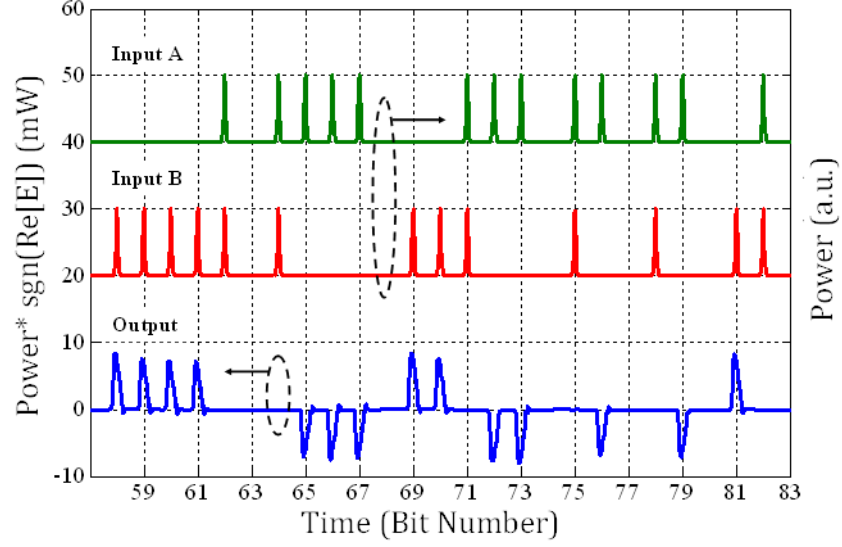
Fig. 4.10 - The all-optical gate OOK inputs and DB output. *Re[E]* is the real part of the output electric field, and *E* has been rotated in the complex plane so as to be aligned with the real axis.

The amplitude of the bottom trace in Fig. 4.10 clearly shows the XOR operation, i.e. modulo 2 addition, between inputs A and B. The sign of the DB output power shows the pulse-to-pulse phase changes as pulse inversions around the zero-power level. The phase inversions occur only when there is an odd number of zeros between pulses which is consistent with DB modulation.

The output modulation format also has particular features in its spectrum. In the section 4.2.3 we used Fourier Transforms to derive the following spectral shape for baseband DB signals:

$$\tilde{Y}_{DB} = \tilde{U}\left(2\pi\frac{F}{T}\right) \cdot \left\{ 2 \cdot \tilde{x}(2\pi F) \cdot e^{-i\pi F} \cdot \cos(\pi F) - \sum_{n=0}^{M-1} e^{-i2\pi nF} \right\} \qquad (4\text{-}15)$$

where $\tilde{Y}_{DB}$, $\tilde{U}$, and $\tilde{x}$ are the Fourier Transforms of the DB signal and a single pulse, and the Discrete-Time Fourier Transform (DTFT) of $x[n]$, respectively. F is the dimensionless normalized frequency, i.e. $F = fT$, where f is the frequency (Hz) and T is bit period (s), respectively. In accordance with the discussion in Section 4.2.3, Eq. (4-15) indicates that the amplitude of the OOK spectrum ($\tilde{x}$) will be modified by a cosine function producing nulls at half-fractional values of the normalized frequency, i.e. $F = \pm 0.5, \pm 1.5B, \pm 2.5B, \dots$ The negative exponential functions suppress the DC component (or the carrier for an optical signal) and modulation-harmonics at $F = 0, \pm B, \pm 2B, \dots$
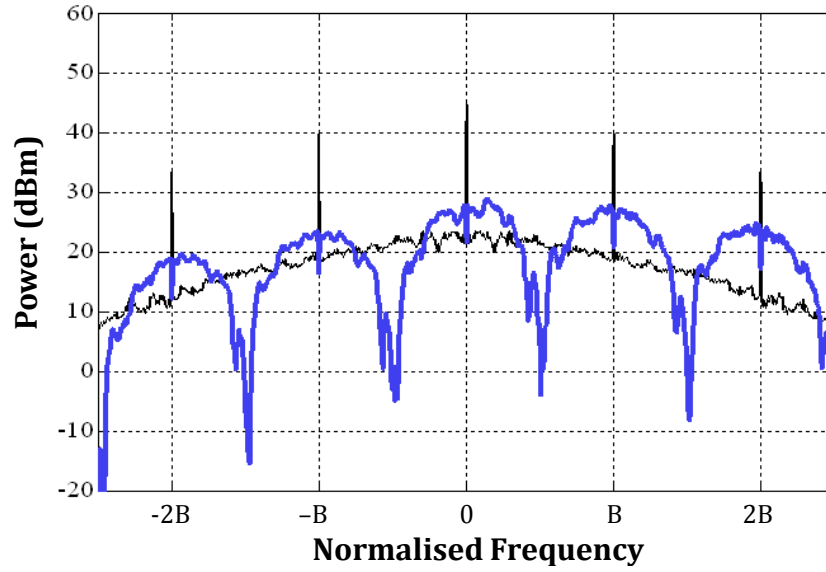
Fig. 4.11 - Output RZ-DB (blue) and RZ-OOK (black) spectra calculated from the electric field output from the XOR gate. Spectral features consistent with Eq. (4-15) can be clearly seen. The frequency axis is centred at the carrier and normalized to the bitrate, *B*.

The spectrum calculated from the modelled output electric field from the XOR gate is shown in Fig. 4.11. Also shown for comparison is the OOK spectrum that results if the phase modulation is stripped from the output field. The DB spectrum agrees with the features predicted in Eq. (4-15). The phase inversions on the output pulses lead to DC component and modulation harmonic suppression and well-defined nulls between the DC component and modulation harmonics as predicted in Section 4.2.3. These predicted spectral features will also be compared with the DB and AMI experimental results discussed in the next section. The results in [82] include similar time-domain and spectral modelling data for the XOR gate operating as an AMI generator.

4.4 Experiments

This section details the experimental setup used and the results obtained at both 42.6 Gbit/s and 10.56 Gbit/s for the all-optical modulation conversion of input OOK to output DB and AMI. As discussed in the previous sections, non-delayed and delayed replicas of the input OOK data are required for input to the XOR gate. One of these copies is then either non-inverted or inverted to produce AMI or DB, respectively. A Dual-Output Wavelength Converter (DOWC) optical gate [83] is utilised to produce two copies of the input data, which in turn drive the XOR gate as modelled above. This SOA-MZI-based optical gate has two output ports which can be easily reconfigured to produce either inverted or

non-inverted copies of the input data. This principle of operation of this scheme is shown in Fig. 4.12.
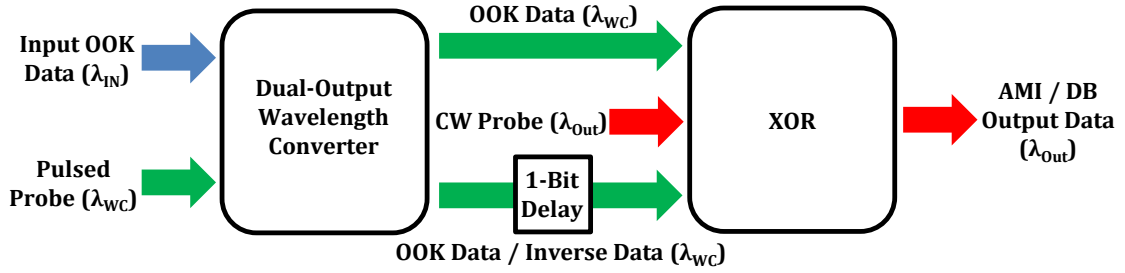
Fig. 4.12 - Conceptual diagram of the all-optical modulation converter incorporating two optical gates.

The DOWC is not strictly necessary for producing AMI, but the extra wavelength conversion allows an arbitrary choice for the final output signal wavelength, including the original input wavelength. The use of two optical logic gates increases the complexity of this system but could still provide benefits at higher bitrates when compared to an optical-electronic-optical (OEO) approach. In a typical OEO approach, the input OOK data would first be demodulated using a photodiode to recover a RF data signal. This signal would then be precoded before being filtered using a low-pass filter (LPF) to generate a three level RF data signal. A local laser source is then modulated using a Mach-Zehnder modulator (MZM), which is biased at null, and driven by the three level RF signal to produce DB data [87]. To generate AMI, different precoding is required before the filter. Although this OEO method may be less complex, it introduces an "electronic bottleneck" meaning scaling to higher bitrates may be difficult [58]. It is important to note that the output pulse sequence from the all-optical technique will generally differ from the input sequence, and a conventional transceiver precoding or decoding will also be required to recover the message.

A detailed picture of the experimental setup is shown in Fig. 4.13. The pair of all-optical gates was produced by CIP Technologies. The proprietary buried-heterostructure SOAs were fabricated using III-V materials and then hybrid-integrated with low-loss planar silica waveguides. The saturated gain recovery times were measured on the SOAs to be ~ 28 ps. The DOWC has two MZI outputs each with full interferometer bias control. These are necessary for independent optimization of the non-inverted and inverted outputs,

particularly when the dynamic XPM shifts are less than π radians. The XOR gate also has integrated push-pull power splitters and delays providing convenient optimization of the relative optical pumping of the two SOAs. Further details on the operation of SOA-based MZIs can be found in references [86, 88].

The RZ-OOK data used at the input to the setup was created by modulating the output of a 10.65 GHz mode-locked laser with a standard 2^7-1 pseudo-random bit sequence (PRBS) and passively multiplexing to 42.6 Gbit/s. The short pattern length was necessary due to the design of the passive data multiplexer. On the left-hand side of Fig. 4.13, the input data at wavelength λ_{in} = 1562.3 nm enters a 3-dB power splitter which provides the push and pull inputs to the DOWC. Variable time delays and attenuators ensure proper timing and relative amplitudes of the two input signals. Fibre-based polarization controllers allow control of the optical field orientation injected into the SOAs. The output from a 42.6 GHz mode-locked laser provides the clock input at wavelength λ_{WC} = 1556.1 nm to the DOWC. The phase shifter (i.e. interferometer bias), shown as φ in Fig. 4.13, on the upper MZI output is adjusted to produce a wavelength-converted copy of the Data input to the XOR gate. The phase shifter on the lower output is independently adjusted to either produce Data or Data-Inverse, corresponding to AMI or DB at the XOR output, respectively. The clocked input to the DOWC is necessary here so that Data-Inverse is generated as an RZ signal.

It is important to note that only RZ formats work for this scheme and as such this will limit its usage in today's optical networks. The main disadvantage of RZ formats is their large bandwidth requirements, when compared to NRZ formats which has resulted in their use lessening in recent years.
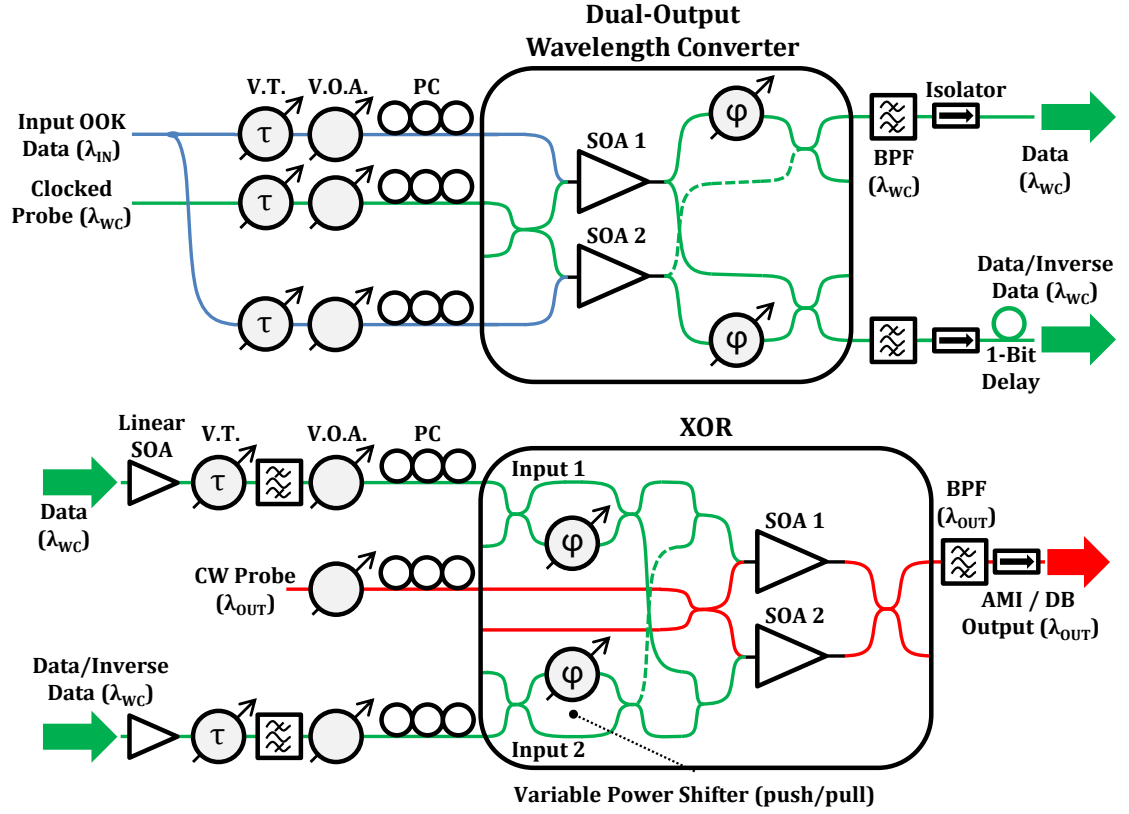
Fig. 4.13 - Detailed experimental setup. BPF, V.T., V.O.A., P.C., and φ are bandpass filter, variable time delay, variable optical attenuator, polarization controller, and phase shifter, respectively.

The outputs from the DOWC are then transmitted to the integrated XOR gate where variable time delays allow adjustment of the necessary 1-bit delay between the two signals. The continuous-wave (CW) probe signal injected into the XOR gate is at wavelength λ_{out} = 1562.5 nm. Numerical values for the measured power levels are given in **Table 4.2**. P_{push}, P_{pull}, P_{clock}, P_1, P_2, and P_{cw} listed in Table 2 are the push, pull, and clock input powers to the DOWC and Input 1, Input 2, and CW input powers to the XOR gate, respectively. P_{out} is the signal output power at λ_{out} from the XOR gate. The SOAs sink ~ 450 mA and ~ 470 mA for the DOWC and XOR gate, respectively.

Table 4.2 - Experimental Parameters

Output Modulation	Power (dBm)					
	P_{push}+ P_{pull}	P_{clock}	P_1	P_2	P_{cw}	P_{out}
AMI	-7.0	-2.5	0.1	2.2	-1.1	-6.9
DB	-1.0	-0.3	4.5	6.7	2.5	-5.6

Evidence for the correct output modulation can be seen on the XOR output spectra [11], which are shown in Fig. 4.14(b) and Fig. 4.14(b). A comparison

between the output DB spectrum (blue line) and the OOK output spectrum (black line) produced by turning off Input 2 to the XOR gate can be seen in Fig. 4.14(a). The spectra are measured using a 0.015 nm resolution and then plotted versus the frequency which has been normalised to the bitrate, *B* (= 42.6 Gbit/s), and centred at the CW carrier. The two spectra are also normalised so that their integrated powers are equal. The OOK spectrum in Fig. 4.14(a) displays the expected carrier and modulation-harmonic peaks at integer values of the normalized frequency, i.e. at multiples of the bitrate, *B*. The other bump-like features in the measured spectra between the modulation peaks are artefacts of the short PRBS pattern.

The DB spectrum in Fig. 4.14(a) exhibits characteristic nulls at fractional values of the normalized frequency ($F = \pm0.5B$, $\pm1.5B$, etc.) as well as suppression of the carrier and modulation-harmonics ($F = 0$, $\pm1B$, $\pm2B$, etc.). Clear and open output eyes corresponding to each spectrum are also shown, which have Q (quality) factors of 26 dB (OOK) and 24.5 dB (DB) as estimated from the equivalent-time scope traces [1]. Similarly, Fig. 4.14(b) shows the AMI output spectrum (green line) plotted along with the OOK output spectrum (black line) when Input 1 to the XOR gate is turned off. In this case, the AMI spectrum shows the expected nulls at integer values of the normalized frequency ($F = 0$, ±1, ±2, etc.). The output eyes are shown in the upper corners and have estimated Q factors of 23 dB (OOK) and 22.2 dB (AMI) when compared with the measured input OOK data Q factor of 28 dB. This results in a penalty of 3-5 dB when using this modulation conversion technique.

These Q factors relate to the number of errors that will be recorded at the receiver and as such give an indication of the performance of the system. Since these values are only estimated from the eye diagrams they may not be exact. However, the Q factor penalty between input and output should match the power penalty calculated from the bit error rate (BER) measurements [89]. As can be seen, there is some degradation observed between the input and output Q factors demonstrating that there will be some errors introduced due to this modulation conversion scheme.
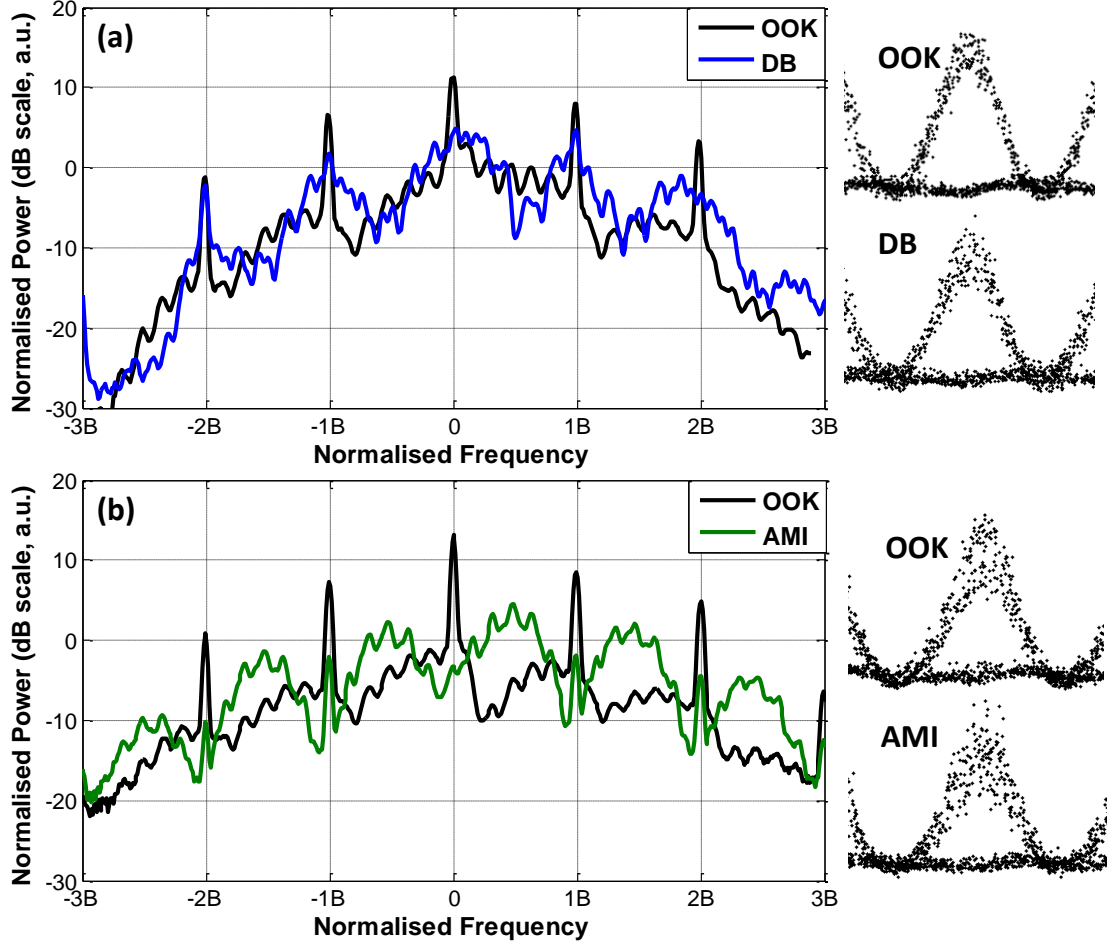
Fig. 4.14 - (a) The OOK and DB output spectrum. (b) The OOK and AMI output spectrum. Frequency axis in both spectra is normalised to the bitrate, *B* (= 42.6 Gbit/s).

The measured spectra in Fig. 4.14(a) and (b) show some deviation from the *cos(πF)* and *sin(πF)* spectral shape predicted by Eqs. (4-13) and (4-11) in section 4.2.3, in particular the partial re-emergence of the modulation-harmonics. These spectral characteristic are thought to manifest, in part, due to the presence of patterning on the output signal, which is expected since the bit period is comparable to the gain recovery time of the SOAs. The relationship between amplitude and phase patterning on the AMI output from the XOR gate has been previously experimentally demonstrated [82]. In this work we noted that the temporally correlated nature of the two XOR input signals leads to unequal average phase shifts for the 0 and π phase-shifted output pulses. This breaks the operational symmetry discussed in Section 4.2 as being necessary for perfectly inverted output pulses and should result in some reduction in carrier suppression. This phenomenon was denoted as phase compression to describe the subsequent sub-π mean phase shift between the two sets of output

marks. Intensity patterning is evident on the eye diagrams in Fig. 4.14 and this suggests the presence of phase patterning and phase compression as well. Other operational and device asymmetries may result in further distortion of the output spectra, yet despite these factors, the suppression of the carriers in the DB and AMI output spectra are measured to be at least ~ 6.4 dB and ~ 16.5 dB, respectively, with respect to the OOK carrier.

The pattern effects and phase compression should be reduced if the input signal data rate is decreased. This allows the SOAs to reach a more recovered state before being pumped by the next data pulse. The experiment described above was repeated at a lower data rate of 10.65 Gbit/s using a similar experimental setup. The probe into the XOR gate in this case is taken from the same clock source providing pulses for the data modulator feeding the DOWC (i.e. Input OOK Data in Fig. 4.13). The output spectra were measured and are shown below in Fig. 4.15.
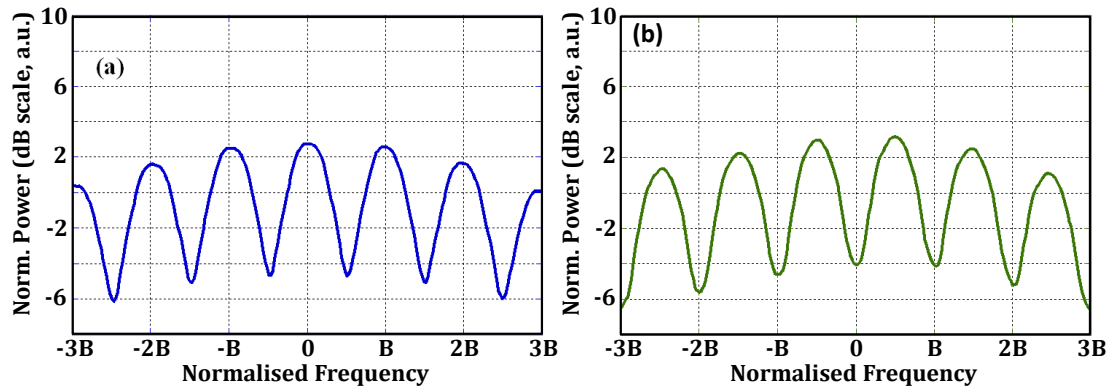
Fig. 4.15 - (a) DB and (b) AMI spectra measured for 10.65 Gbit/s modulation conversion. Horizontal axis is normalised to the bitrate, *B* (= 10.65 Gbit/s).

The spectra show excellent carrier and modulation-harmonic suppression and also clearly display the *cos(πF)* and *sin(πF)* spectral envelope shape predicted by the Fourier analysis described in section 4.2.3 and given in Eqs. (4-13) and (4-11).

These results suggest that by employing faster SOA configurations, the output signals at 42.6 Gbit/s can be improved. This could be accomplished using nanophotonic devices such as quantum dots [90] or perhaps by utilizing alternate filtering schemes [61, 91, 92]. The use of a pattern suppression scheme in a SOA-based MZI wavelength converter has also been experimentally demonstrated [83]. This technique utilizes the injection of an additional data-

inverse signal into the probe input port of the gate, effectively equalizing the optical energy in the SOAs in every bit period. Such a technique can be adapted to operate with XOR gates.

4.5 Summary

This chapter included an experimental demonstration of a 42.6 Gbit/s OOK-to-AMI and OOK-to-DB all-optical modulation converter consisting of two hybrid-integrated SOA-based MZI gates: a Dual-Output MZI and an XOR gate. The DB and AMI formats were theoretically predicted at the output of the XOR gate using a transfer function analysis as well as a comprehensive computer-based SOA model. The experimental results indicate open output eyes and spectral features matching those predicted using a simple Fourier Transform analysis of the XOR gate operation. Comparison with 10.65 Gbit/s data suggests the importance of the carrier density recovery time and the impact of the pattern effect on the quality of the output signals.

Degradations in the Q factor of 3.5 dB and 5 dB were measured with respect to the input OOK signal for both DB and AMI, respectively. This reduction in the Q factor results in a higher probability of errors at the receiver which means the use of this all-optical modulation conversion scheme will have a penalty associated with it. However, this penalty can be minimised by using the improvements mentioned earlier, such as faster SOAs. Ideally, direct measurement of the BER would provide greater insight into the performance of this system. However, the 42.6 GHz mode-locked laser, used as the input clock to this system, produced an error floor which impaired any results taken. The use of an alternate clocked laser source would fix this issue.

This dual-gate active approach to modulation conversion has the potential for 3R regeneration, can output to an arbitrary wavelength (within the SOA gain bandwidth), and can easily change between DB and AMI outputs. The system is also amenable to further photonic integration and subsequent reductions in power consumption. This all-optical approach to DB and AMI generation could impact implementations of both high-speed transmitters and modulation converters.

5.

Phase-Sensitive Frequency Conversion of Quadrature Modulated Signals

This chapter details a phase sensitive frequency conversion scheme based on nonlinear mixing in semiconductor optical amplifiers (SOA), i.e. four-wave mixing (FWM), which can separate the two orthogonal phase components of an optical signal onto two different frequencies. An experimentally verified numerical model is used to confirm the correct operation principles of this phase discrimination technique, separating a 40 Gbaud quadrature phase shift keyed (QPSK) signal into two 40 Gbit/s binary phase shift keyed (BPSK) signals, before it was experimental demonstrated on a 10.65 Gbaud QPSK signal, producing two 10.65 Gbit/s BPSK signals at different frequencies.

5.1 Introduction

As the demand for higher capacity networks continues to grow, higher order modulation formats such as QPSK have become increasingly common in today's optical networks. High order phase encoded modulation formats generally require complex coherent receivers to demodulate the information at the receiver. The all-optical phase discrimination technique detailed in this chapter was used to convert QPSK data into two BPSK signals before demodulation using a delay interferometer (DI). Differential phase shift keying (DPSK) is normally required when using a DI, however, since a pseudo-random binary sequence (PRBS) data pattern is used, the BPSK signal can be demodulated using a DI. This is due to the fact that when PRBS data undergoes encoding, when generating a DPSK signal, it produces the same PRBS sequence. This

means the recovered BPSK signal can be considered a DPSK signal and a DI used for demodulation. This phase discrimination technique is novel and negates the need for a complex coherent receiver.

An experimentally verified numerical model was used to simulated the demodulation of a 40 Gbaud QPSK signal into two 40 Gbit/s BPSK signals [93]. An experimental demonstration of this phase discrimination technique was performed on a 10.65 Gbaud QPSK signal which was separated into two 10.65 Gbit/s BPSK signals before demodulation with a DI [14]. Experimental results demonstrate the effectiveness of SOAs for nonlinear mixing over a wide range of wavelengths and difference frequencies and confirm the accuracy of the numerical model.

Nonlinear mixing in optical devices is a well-known means of providing phase-sensitive amplification and can be used to regenerate BPSK signals [94-97]. QPSK signals can be regenerated by arranging two phase sensitive amplifiers in parallel [38]. More recently, a phase-sensitive amplifier with a four-step phase transfer characteristic has been demonstrated that can regenerate QPSK signals in a single device [98, 99]. Phase-sensitive frequency conversion of BPSK using nonlinear mixing has also been shown [39] and has the potential for greater phase discrimination because of the isolation of the output from the input signal.

SOAs have been extensively studied as nonlinear mixing elements [100-103] and offer a number of advantages. As mentioned previously, they require only sub-milliwatt input powers, provide gain, are compact and are also readily integrated. This chapter includes experimental verification that SOAs can be efficient nonlinear mixing devices over a broad range of wavelengths and difference frequencies. There are two mechanisms by which phase-sensitive frequency conversion can be obtained and both are detailed in this chapter. The first is that exploited in Croussore and Li's experiment [39], but only the second, introduced in Webb *et al* [13], allows more than one phase component to be converted to separate outputs simultaneously which is a key component for a true phase discrimination technique.

In this chapter, Section 5.2 details an investigation into the nonlinear mixing (FWM) efficiency in SOAs, before Section 5.3 discusses the mechanism by which phase sensitive frequency conversion is achieved. Section 5.4 simulates this all-optical technique before Section 5.5 provides an experimental demonstration. Finally Section 5.6 gives a brief summary of the results obtained in this chapter.

5.2 Nonlinear Mixing Efficiency

In order to assess the efficiency of nonlinear mixing in SOAs, devices were characterized over a range of wavelengths and difference frequencies. The measurements were carried out by injecting two continuous wave (CW) pump inputs, at wavelengths λ_1 and λ_2, into the SOA and observing the output spectrum. Nonlinear mixing between the two pump inputs produced additional frequency components spaced at multiples of the difference frequency. The output powers of the two first-order sidebands and the amplified pumps were recorded with an optical spectrum analyser. Wavelength dependence was investigated by stepping λ_1 from 1530nm to 1585nm in 5nm increments. With λ_1 fixed at each wavelength step, λ_2 was swept from $\lambda_1 + 0.08$nm to $\lambda_1 + 11$nm, thus varying the difference frequency from ~10GHz to ~1.4THz. To speed up data collection, the experiment was largely automated using LabVIEW (Fig. 5.1).
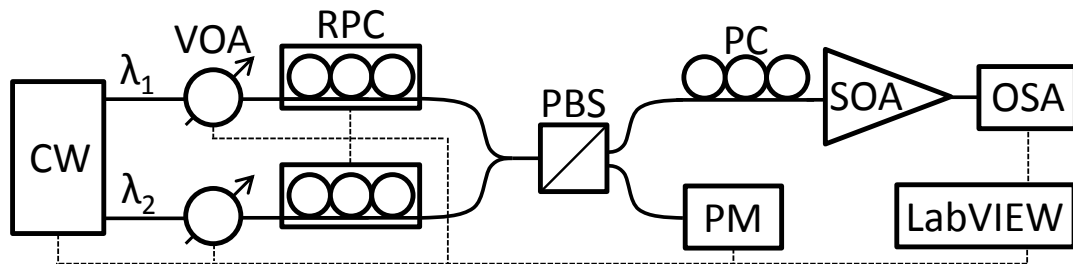
Fig. 5.1 - Experimental system (VOA: variable optical attenuator, RPC: remote polarisation controller, PBS: polarisation beam splitter, PC: polarisation controller, PM: power meter, OSA: optical spectrum analyser). The solid lines represent optical paths and the dotted lines are data and control paths.

The bias current of the SOA was set to 400mA and two variable optical attenuators kept the power of each pump at a constant -10 dBm at the input facet for all wavelength settings. Since the relative polarisation of the pumps at the ends of their connecting fibres varied with tuning, two remote polarisation controllers were used to ensure that both injected signals remained co-polarized for maximum nonlinear mixing efficiency. The pumps were combined

and passed through a polarisation beam splitter. A downhill simplex algorithm adjusted the remote polarisation controllers to minimize the power measured at the unused output port. A manual polarisation controller set the polarisation state at the SOA input for maximum gain.

In order to refer the measured powers to the SOA facets, the coupling efficiencies at the input and output of the SOA were measured. A CW source was connected to each fibre tail in turn and varied in power, and the photocurrent generated in the SOA with the PN junction at 0V bias was measured. With the assumption that all of the light reaching the active region stimulated photocurrent, the coupling efficiency is given by:

$$\eta = \frac{\hbar\omega I}{eP} \tag{5-1}$$

where $\hbar\omega$ is the photon energy, I is the photocurrent, e is the charge of an electron, and P is the injected power.

The waveguide loss is one of the parameters used in the SOA model (described in the Appendix 8.1) and is equal to the loss of the SOA when the bias current is set to give a net material gain of 0 dB. At this bias, which depends on input wavelength, the number of carriers generated by absorption balances the number removed by stimulated emission when averaged along the length of the device. There is, therefore, no change in junction voltage when the input power is varied. The bias for transparency was found by amplitude modulating the optical input at 1 kHz and observing the phase reversal of the junction voltage variation when the transition point between net material gain and loss was reached. The waveguide loss was measured at a number of points across the gain band and showed little wavelength dependence.

5.2.1   Nonlinear Mixing Efficiency Results

Sets of measurements were made on a number of SOAs using a range of wavelengths for the fixed pump. Here we concentrate on the SOA which has been employed previously to demonstrate separation of the in-phase and quadrature phase components of a signal (a CIP NL-OEC-1550) [13]. When biased at 400 mA, this device had a peak small-signal gain of 32 dB at 1560 nm

and a saturated output power of 15.4 dBm at 1550 nm (all measurements referred to the SOA facets).
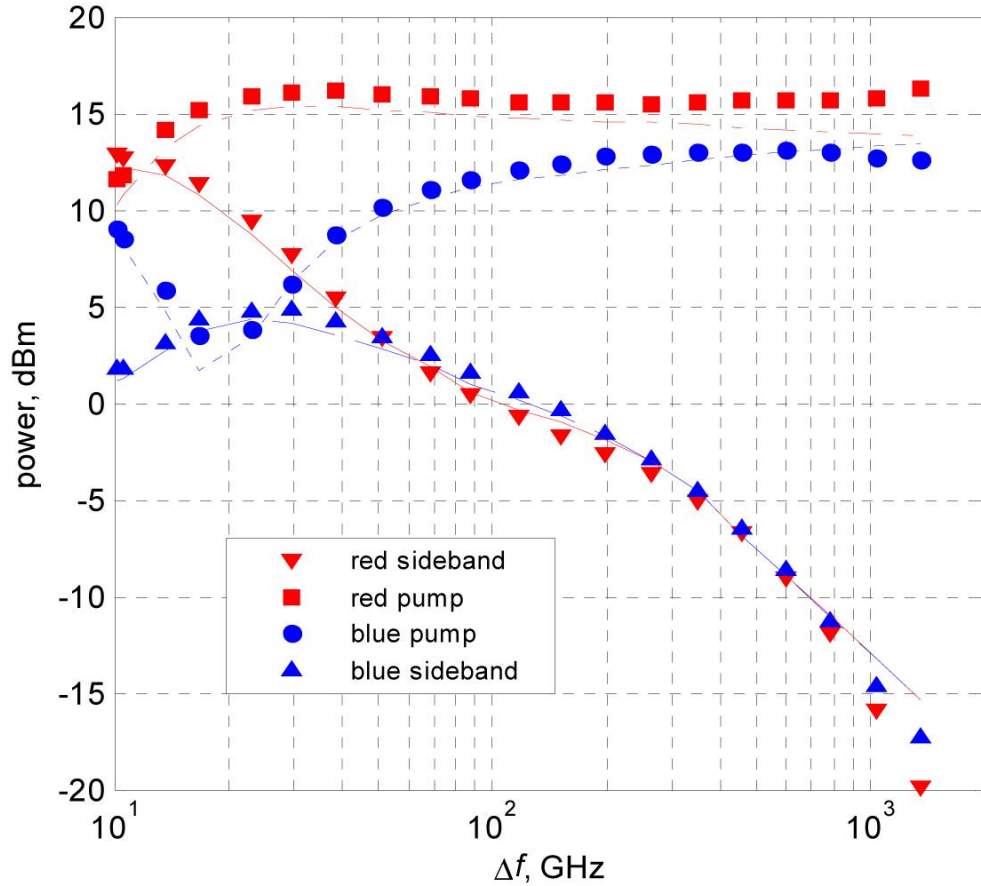
Fig. 5.2 - Pump and sideband powers for fixed-pump wavelength = 1555nm. Symbols are measurements and lines are model results.

Nonlinear mixing results for a fixed-pump wavelength of 1555 nm, the centre wavelength in our previous experiment, are shown in Fig. 5.2, where the output pump powers and the powers of the two first-order sidebands have been plotted against the frequency difference between the pumps. Simulated results from the model described in the Appendix (Section 8.1) are also shown. For difference frequencies up to 50 GHz there was a strong transfer of power from the blue (fixed) pump to the red (swept) pump and the red sideband was larger than the blue sideband. At higher frequencies, the sideband powers rolled off with increasing slope, but remained greater than the input pump powers (-10 dBm) until the difference frequency reached 600 GHz. The availability of frequency conversion gain up to such a high frequency is attributed to carrier temperature modulation.

For difference frequencies up to 700 GHz, the simulated sideband powers were within 1 dB of the experimental measurements. However, above this frequency the roll-off of the measured sideband powers was more rapid than the 6 dB/octave expected from an exponential decay of the carrier temperature with time (Eq. (8-8) in Appendix). Dispersion in the SOA did not appear to account for this discrepancy because calculations based on the ASE fringe spacing suggest that dispersion should not have significant effect for difference frequencies below 2THz.
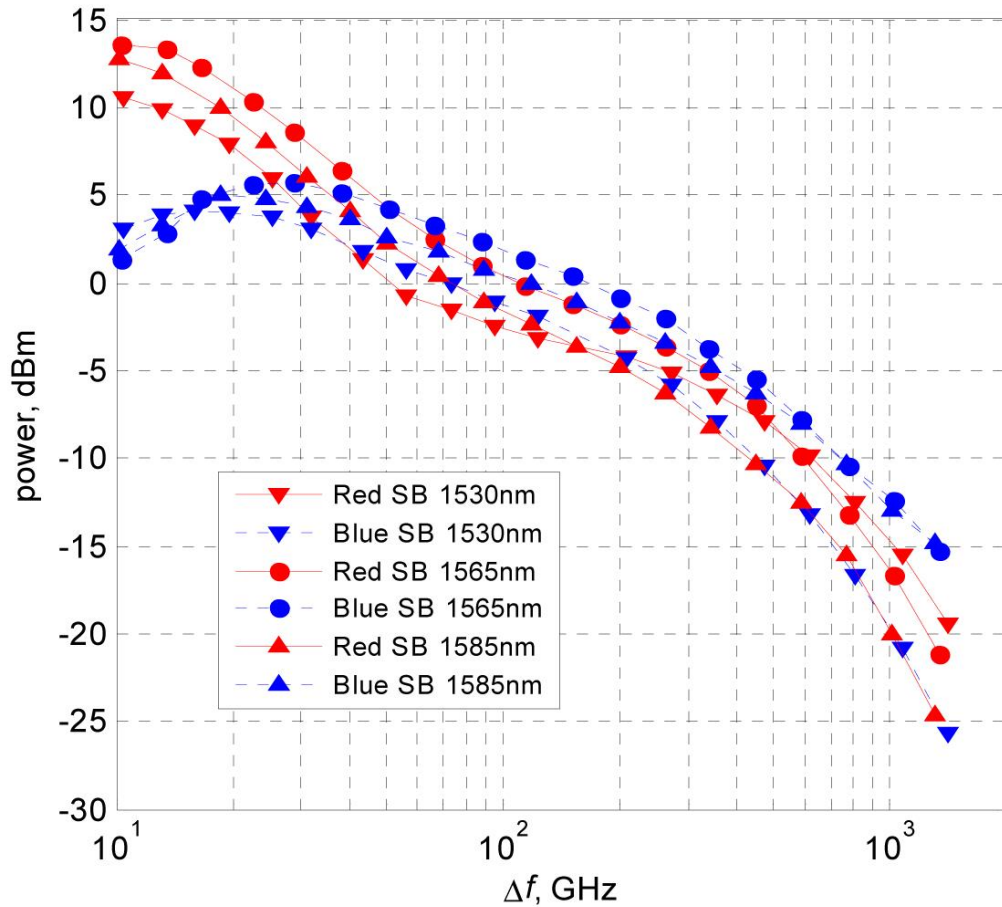
Fig. 5.3 - Sideband powers for three fixed-pump wavelengths. Lines are to guide the eye.

The sideband powers were also plotted for fixed-pump wavelengths of 1530nm, 1565nm and 1585nm (Fig. 5.3), represented by the different shaped symbols. These wavelengths correspond to the shortest pump wavelength used, the pump wavelength giving the maximum sideband power, and the longest pump wavelength used, respectively. For difference frequencies up to 400GHz, the frequency conversion process showed gain for all these wavelengths and the variation of sideband power with fixed-pump wavelength was less than 5

dB, demonstrating that SOAs are well suited to the phase-sensitive frequency conversion application described in the next section.

5.3 Principles of Phase-Sensitive Frequency Conversion

The nonlinear mixing between optical fields that occurs at each point along the length of a SOA can be regarded as a two-stage process. Firstly, interference between the fields gives rise to beats in the total power and the carrier density and temperature vary in response to the beats. Secondly, these variations cause phase and amplitude modulation of the fields, generating new sidebands as detailed in Chapter 2 [40, 101, 104]. We show in the following that there are consequently two mechanisms by which the amplitude of a frequency converted output can become sensitive to signal phase. Either the interference between the signal and some pump fields is arranged so that the power beats at a given frequency vary in amplitude with signal phase, or the output can be the sum of two or more sidebands whose relative phases depend on signal phase. Using the first mechanism, only one phase component of the signal can be converted to a new frequency. However, by using the second mechanism, multiple outputs dependent on different phase components of the signal are possible.

The beating between a signal, with electric field given by:

$$U_s(t) = u_s \text{exp} i(\omega_s t + \varphi_s) \tag{5-2}$$

and a pump electric field, given by:

$$U_{p1}(t) = u_p \text{exp} i(\omega_s - \Delta\omega)t \tag{5-3}$$

causes modulation at the difference frequency, $\Delta\omega$ ($= 2\pi\Delta f$) as described in Chapter 2. The power of the summed fields (choosing units so that power = mean square field) is given by:

$$P(t) = \frac{u_s u_p}{2} \cos(\Delta\omega t + \varphi_s) + constant\ term \tag{5-4}$$

The modulation amplitude is independent of the signal phase, φ_s. Introducing a second pump with the same amplitude as the first and with equal but opposite

frequency difference from the signal (the two difference frequencies are assumed to be phase locked),

$$U_{p2}(t) = u_p expi(\omega_s + \Delta\omega)t \tag{5-5}$$

gives rise to a power modulation at $\Delta\omega$ whose amplitude varies as the cosine of signal phase.

$$P(t) = u_s u_p \cos\Delta\omega t + const. \, and \, higher \, freq. \, terms \tag{5-6}$$

An additional probe input at another optical frequency will acquire sidebands (idlers) as a result of this modulation (Fig. 5.4(a)). It is not necessary for the SOA to respond to the beats between the probe and the pump or signal, so the probe frequency can be far removed provided that it remains within the gain bandwidth of the SOA. The sidebands will be proportional (for small modulation depths) to one phase component only ($\varphi_s = 0$) of the input signal. This is the arrangement used by Croussore and Li to obtain phase-regenerative wavelength conversion [39].
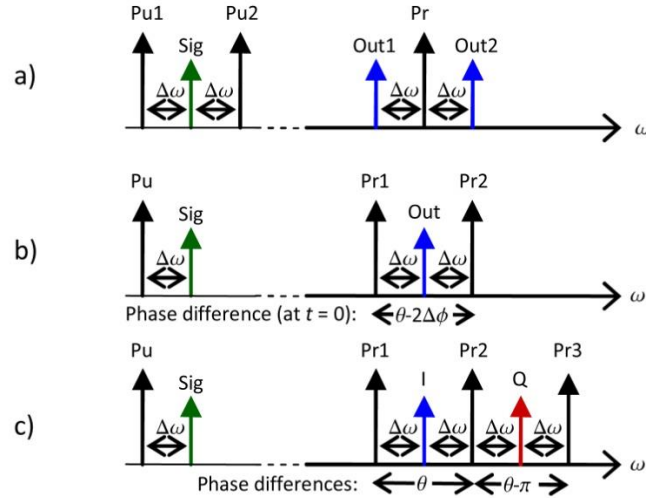
(Pu = pump, Pr = probe, I = in-phase output, Q = quadrature output).

Fig. 5.4 - Examples of phase-sensitive frequency conversion schemes. (a) Croussore and Li's scheme with two pumps and one probe. Both outputs follow the same phase component of the signal. (b) Alternative scheme with one pump and two probes. Probe phases set to select φ_s signal component. (c) With a third probe, in-phase and quadrature outputs can be obtained simultaneously. (Pu = pump, Pr = probe, I = in-phase output, Q = quadrature output).

However, it is also possible to use an inverse configuration with one pump and two probes, with frequencies $\pm \Delta\omega$ relative to the output frequency, ω_0 (Fig. 5.4(b)). Consider first a single probe with electric field $V(t)$. The signal-pump

beats (Eq. (3)) causes both phase and amplitude modulation of the probe, and the first-order lower and upper sidebands are given by:

$$V_L(t) = V(t) \left\{ J_1(\beta) \text{exp} i \left(\frac{\pi}{2} - \varphi_\beta \right) + \frac{m}{2} \text{exp}(-i\varphi_m) \right\} \text{exp}$$
$$- i(\Delta\omega + \varphi_s) \tag{5-7}$$

and

$$V_U(t) = V(t) \left\{ J_1(\beta) \text{exp} i \left(\frac{\pi}{2} - \varphi_\beta \right) + \frac{m}{2} \text{exp}(i\varphi_m) \right\} \text{exp} i(\Delta\omega + \varphi_s) \tag{5-8}$$

where the phase and amplitude modulation is assumed to be sinusoidal with modulation coefficients β and m, respectively, and phases φ_β and φ_m relative to the power variation. J_1 is the first-order Bessel function. In general, $\varphi_\beta \neq \varphi_m$, because the carrier density responds more slowly to the power modulation than the carrier temperature does and the band filling alpha factor is larger than the carrier heating alpha factor [105]. It may be shown that this leads to the upper sideband of each probe being larger than its lower sideband. However, if the two probes, with electric fields $V_1(t)$ and $V_2(t)$ at frequencies $\omega_0 - \Delta\omega$ and $\omega_0 + \Delta\omega$ respectively, are defined so that

$$V_1(t) = \frac{u_0 \text{exp} i(\omega_0 t - \Delta\omega t + \Delta\varphi)}{J_1(\beta) \text{exp} i \left(\frac{\pi}{2} - \varphi_\beta \right) + \frac{m}{2} \text{exp}(i\varphi_m)} \tag{5-9}$$

and

$$V_2(t) = \frac{u_0 \text{exp} i(\omega_0 t + \Delta\omega t - \Delta\varphi)}{J_1(\beta) \text{exp} i \left(\frac{\pi}{2} - \varphi_\beta \right) + \frac{m}{2} \text{exp}(-i\varphi_m)} \tag{5-10}$$

where u_0 and $\Delta\varphi$ are freely chosen parameters, then the upper sideband of $V_1(t)$ and the lower sideband of $V_2(t)$ have equal amplitudes and both appear at the centre frequency, ω_0, between the two probes. They sum to give the output field:

$$V_0(t) = 2u_0 \cos(\varphi_s + \Delta\varphi) \text{exp}(i\omega_0 t) \tag{5-11}$$

As implied by Eq. (8) and (9), the difference frequencies between the two probes and the output frequency must be phase locked to the difference between the signal and the pump, but the output can have arbitrary phase. Thus

the output of this configuration also shows signal-phase selectivity, being proportional to one phase component only ($\Delta\varphi$) of the input signal. The desired signal phase component is selected by setting the phase difference between $V_2(t)$ and $V_1(t)$ to $\theta - 2\Delta\varphi$, where θ is the phase difference (given by Eqs. (8) and (9)) for $\Delta\varphi = 0$. (The effect of beating between the probes has been ignored in this analysis because it does not generate any sidebands at the output frequency, ω_0. It can, however, modify the probes themselves but the probe input amplitudes and phases can be adjusted to compensate.) There is an important difference in the operating mechanism of the two configurations. In contrast to the Croussore and Li scheme, the amplitude of the power modulation in the configuration proposed here does not vary with signal phase. Instead, phase selectivity is obtained by forming the output from the vector sum of two sidebands. As a result, a further pair of probes can be introduced to generate a second output with a different dependence on signal phase (Fig. 5.4 (c)). By setting $\Delta\varphi = 0$ for one probe pair and $\Delta\varphi = -\pi/2$ for the second, both the in-phase and quadrature components of the signal can be extracted simultaneously in a single device. For example, three probes can be used, i.e. two pairs sharing a common central probe, to generate the in-phase and quadrature outputs at different frequencies.

More complex configurations are possible, such as the examples reported previously [13] and in the following section, where the signal is placed in one gap in a four-tooth frequency comb and orthogonal outputs are generated in the other two gaps. The signal must be phase locked to the comb. In these cases, the frequency comb teeth act as both pumps and probes and multiple mixing processes contribute to each output.

5.4 Simulation of Phase-Sensitive Frequency Conversion

Using the numerical model presented in the Appendix and verified by comparison with the measurements presented in Section 5.2, a simulation of the four-tooth frequency comb scheme similar to earlier published work [13] but with doubled comb spacing and symbol rate is detailed. A Mach-Zehnder interferometer (MZI) with a SOA in each arm [106] was employed as the nonlinear element in order to reject the amplified pumps and probes, thus

reducing the demands placed on the bandpass filters used for the output signals.

5.4.1 Four-Tooth Frequency Comb Scheme
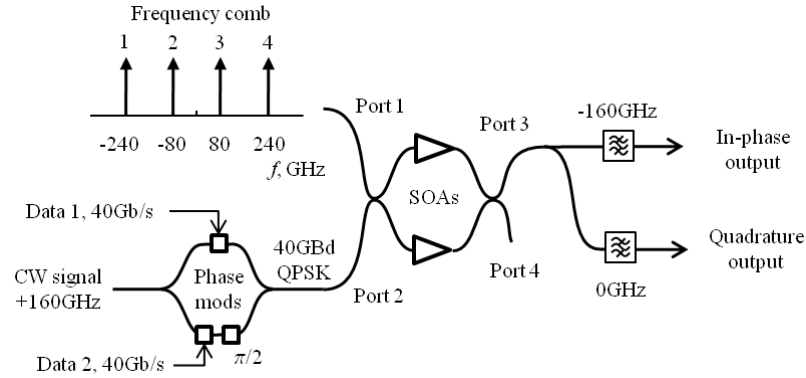
Fig. 5.5 - Simulation of four-tooth frequency comb scheme. Frequencies shown are relative to the comb centre frequency.

For this simulation, a four-tooth frequency comb with 160GHz spacing and centre wavelength 1555nm was connected to input port 1 and the symbol rate of the QPSK signal connected to port 2 was set to 40 Gbaud in order to investigate phase-sensitive signal processing in SOAs at a high data rate (Fig. 5.5). The signal carrier frequency was phase locked to the comb and set at the midpoint between the two highest frequency comb teeth, giving a signal pump difference frequency, Δf, of 80GHz. The comb powers and phases (**Table 5.1**) were optimized to obtain BPSK outputs at the comb centre and between the two lower frequency comb teeth ($2\Delta f$ relative to the comb centre). The two outputs showed low crosstalk (Fig. 5.6) and gains of 4 dB relative to the mean signal power despite the increased frequency spacing (not including filter and SOA coupling losses).

Table 5.1 - Inputs and outputs for the four-tooth comb scheme.

	Frequency	Phase (radians)	Power (dBm)
Signal	f_{cent} + 160GHz	QPSK	-8.56
Comb 1	f_{cent} − 240GHz	0.76	8.3
Comb 2	f_{cent} − 80GHz	0.37	-10.9
Comb 3	f_{cent} + 80GHz	0.5	-14.5
Comb 4	f_{cent} + 240GHz	2.16	-2.3
In-phase output	f_{cent} - 160GHz	BPSK	-4.5
Quadrature output	f_{cent}	BPSK	-4.5

f_{cent} = comb centre frequency, 193THz (1555nm).
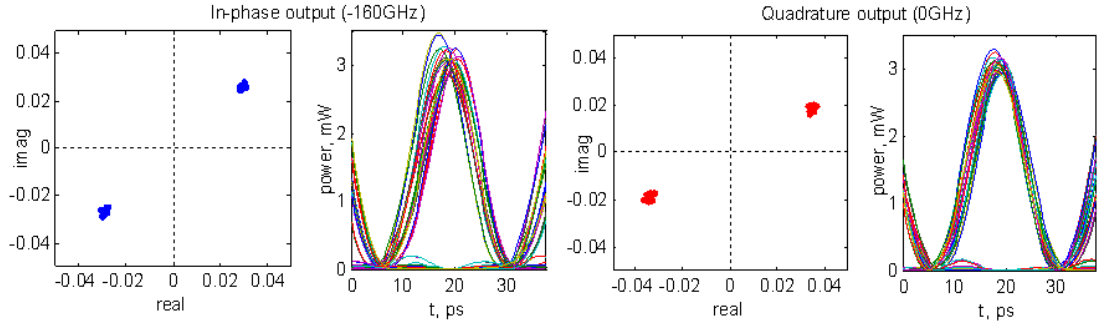
Fig. 5.6 - BPSK constellations from the four-tooth frequency comb scheme with eye diagrams after DPSK demodulation. The field components are in units of $\sqrt{(2W)}$.

Simulations with a CW input stepped through a range of phase values again showed that comb settings for optimum signal performance and for optimum CW response did not exactly coincide (Fig. 5.7). Calculation of the constituent vectors of the two outputs revealed that the behaviour of this scheme was rather more complex. The comb teeth beat with the signal and with each other to generate power beats at all integer multiples of the difference frequency from Δf to $6\Delta f$. Each output was the sum of five vectors and, each vector varied in amplitude as well as phase with signal phase (Fig. 5.8), indicating that both mechanisms of phase-sensitive frequency conversion identified in Section 5.3 were in operation.
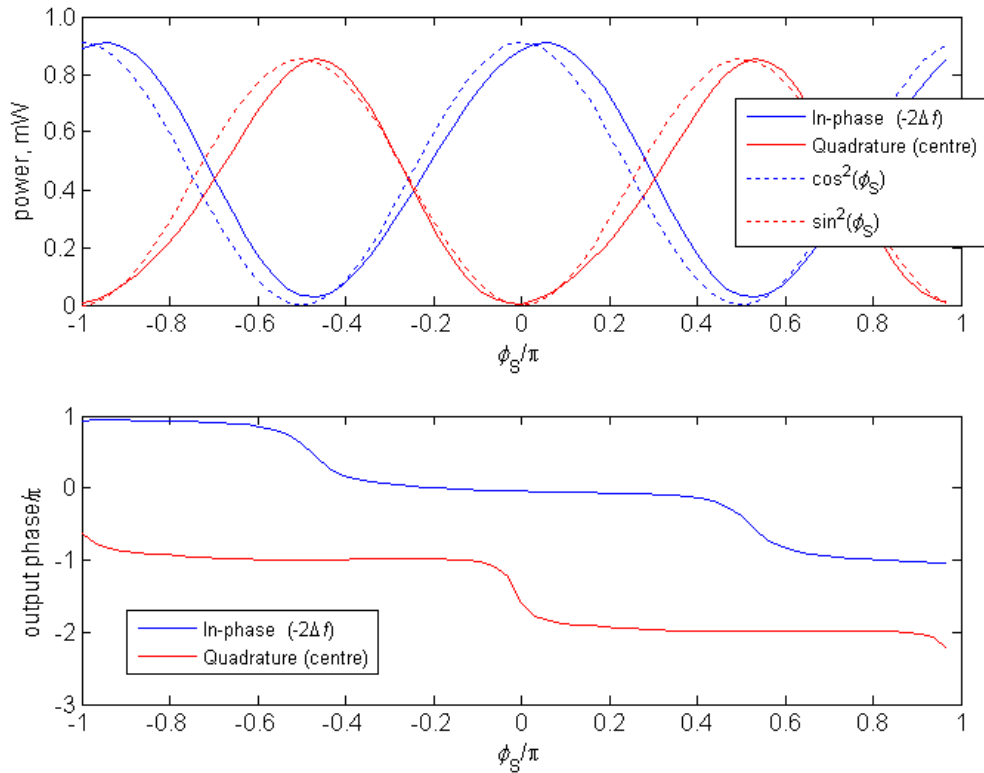
Fig. 5.7 - In-phase and quadrature outputs of the four-tooth frequency comb scheme. CW input phase.
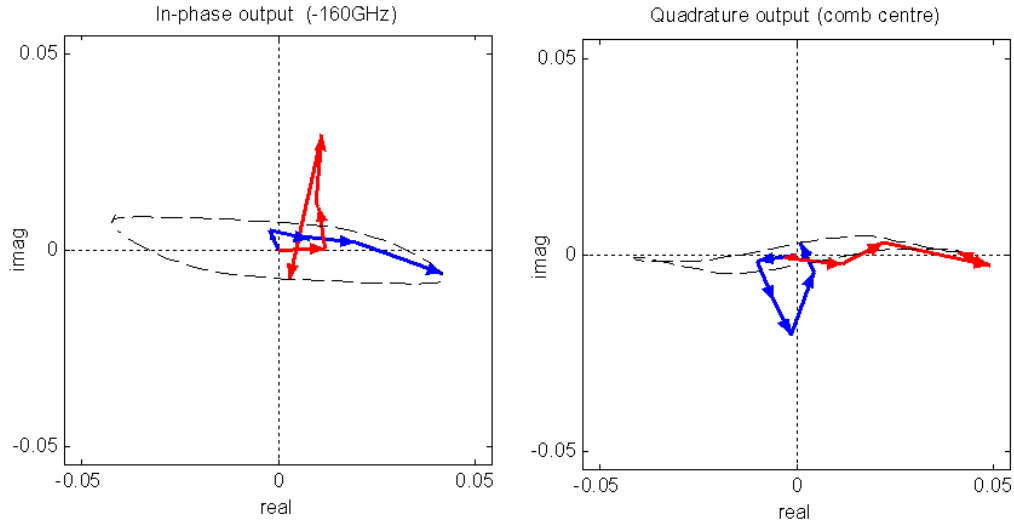
Fig. 5.8 - Vector components of the four-tooth frequency comb scheme outputs. **Table 5.2** lists the vectors starting from the origin of the plots. Column 1 shows the input component from which each vector is derived. Colum 2 shows the relative frequency of the modulation sideband contributing to the in-phase output and, similarly, column 3 shows which sideband contributes to the quadrature output. Blue arrows show their summation for the CW input phase, $\varphi_s = 0$, and red arrows correspond to $\varphi_s = \pi/2$. Dashed lines show the locus of the vector sum for all φ_s.

Table 5.2 - Inputs and outputs phase for the four-tooth comb scheme.

	Sideband relative frequency (GHz)	
Input component	In-phase output	Quadrature output
Comb 4	-400	-240
Signal	-320	-160
Comb 3	-240*	-80
Comb 2	-80	+80
Comb 1	+80	+240

* Vector not visible at this scale.

5.5 Experimental Demonstration

An experimental investigation of the four-tooth comb scheme was also performed, the details of which are recorded in this section. The simulation results in the previously mentioned suggest that higher bitrate (>40 Gbaud) phase discrimination is feasible using SOAs. However, due to the availability high bandwidth equipment, such as modulators and synthesisers, this experiment was demonstrated using a 10.65 Gbaud QPSK signal, not the 40 Gbaud QPSK signal used in the simulation results. This also relaxed the required comb spacing to 85.2 GHz, with a resulting signal pump spacing of 42.6 GHz.

Initially a SOA based MZI, similar to the simulation in the previous section, was to be utilised. Due to an imbalance in the first 3 dB splitter of the device a single SOA (a CIP NL-OEC-1550) was used instead. This power imbalance would cause a power difference into each SOA in the MZI and result in different mixing conditions in each arm. The single SOA scheme necessitated the use of a wavelength selective switch (WSS) at the output of the SOA to filter out each of the two BPSK channel frequencies.

In a real world system a method of recovering the optical carrier of the incoming QPSK signal [107], a local RF clock (i.e. 40 GHz) and a method of generating a comb, such as in [41],would be required to generate the four pumps at exact optical frequency spacings around the incoming QPSK signal, a crucial aspect of this phase discrimination technique. However, for the purpose of this proof-of-principle experiment a comb is generated first before one of its comb lines is extracted and modulated with QPSK data thus providing pumps at the correct optical frequency spacings.

5.5.1   Experimental Setup

A distributed feedback laser (DFB) was used in conjunction with two MZM each of driven by a 42.6 GHz RF source to produce a spectral comb with seven lines which were spaced at the RF drive frequency [41]. The biases of both MZM and the phase difference between the two RF drive signals were optimised to produce a comb with a flatness less than 0.5 dB and a side mode suppression ratio (SMSR) of >20 dB. This comb was then injected into a four port wavelength selective switch (WSS) which was capable of controlling the individual amplitude and phase of each line of the comb. The WSS suppressed every second comb line to produce the four-tooth comb (pumps) required, each spaced 85.2 GHz apart. A further single (CW) signal, spectrally located equidistant between the two highest frequency pumps, was extracted to the second port of the WSS from the original comb.
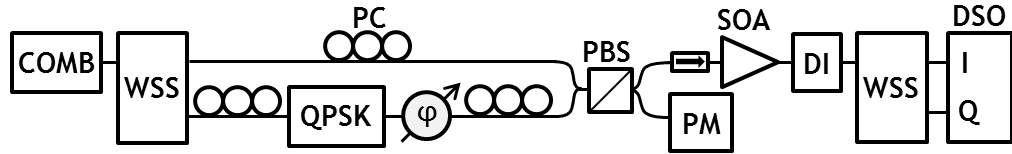
Fig. 5.9 - Experimental Setup

This single CW signal was modulated with a QPSK modulator driven by two 10.65 Gb/s 2^{10}-1 bit PRBS data RF signals to produce a 10.65 Gbaud signal. The QPSK modulated signal was then passed through a phase modulator (φ), which was used to control the absolute phase of QPSK signal relative to the pumps. This allowed for any phase drift between the two paths to be corrected. The four pumps and the QPSK signal were passed through separate polarisation controllers (PC) and recombined in a 3 dB splitter before they were passed through a polarisation beam splitter (PBS). The two PCs and a power meter (PM) at the unused port of the PBS ensured both signals were co-polarised. This was important because the four-wave mixing (FWM) efficiency in the SOA is dependent on the relative polarisation of the signals [33, 108]. The combined signals were then injected into the SOA.

As detailed in previous sections, FWM is used to produce two BPSK signals, I and Q, at separate frequencies located between the first three pumps. The first WSS was used to control this relative phase and amplitude of each pump and QPSK signal to ensure maximum phase discrimination at the output of the SOA. The I and Q channels at the output of the SOA will have different carrier frequencies, however, they can be simultaneously demodulated using a delay interferometer (DI) with a (free spectral range) FSR of 10.65 GHz, provided the channels carrier frequencies are separated by multiples of the FSR, as is the case here. A second WSS was then used to filter out both the I and Q channels to separate ports, where they were observed on a digital sampling oscilloscope (DSO).

5.5.2   Experimental Results

Initially, to verify the correct operation of this experimental setup and to optimize the system for maximum phase discrimination, the QPSK data was disabled resulting in the CW signal passing through the QPSK modulator without incurring any modulation. This CW signal was then combined and co-

polarised with the four pumps before being injected into the SOA. The first WSS optimised the amplitude and phase of each pump such that when the phase of CW signal was switched by π/2 radians it gave a maximum extinction to both the I and Q channels, when observing the output spectrum of the SOA (Fig. 5.10).
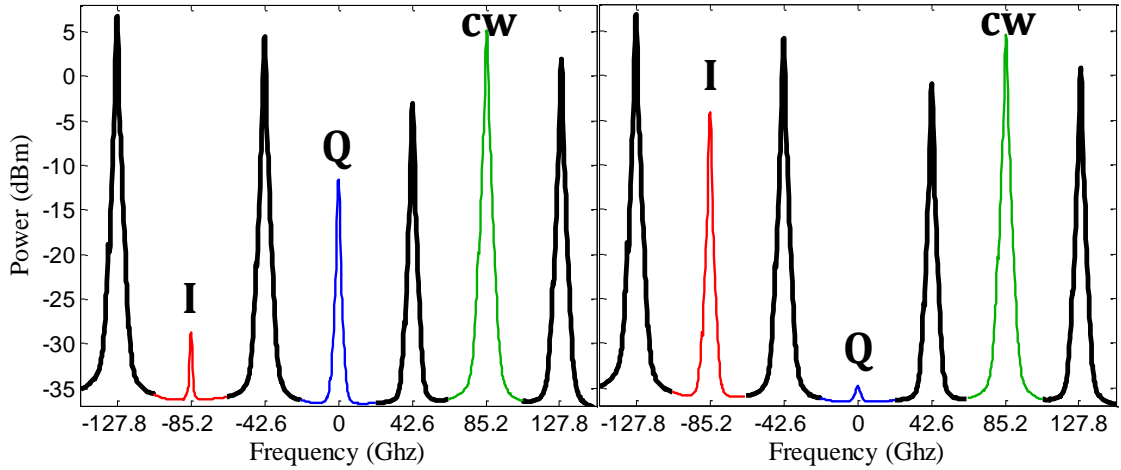
Fig. 5.10 – (a) CW φ = 0, (b) CW φ = π/2, Pumps = Black

Next the phase modulator (φ) was driven with a low frequency (~600 Hz) sinusoidal signal through 2π radians to produce a low frequency phase modulated signal. This phase modulated signal was combined and co-polarized with the four pumps, as mentioned previously, before being injected in the SOA. At the output of the second WSS two low frequency photo receivers were used to observe the resulting I and Q channels. The output of the two photo receivers was read into a computer using two analogue-to-digital converters (ADC), and a Matlab program was then used to optimise the relative amplitude and phase of each of the four pumps and the low frequency phase modulated signal to produce the maximum phase discrimination. Fig. 5.11 shows the resulting I and Q channels of a sinusoidally modulated signal. Extinction ratios greater than 14 dB were measured for both channels.
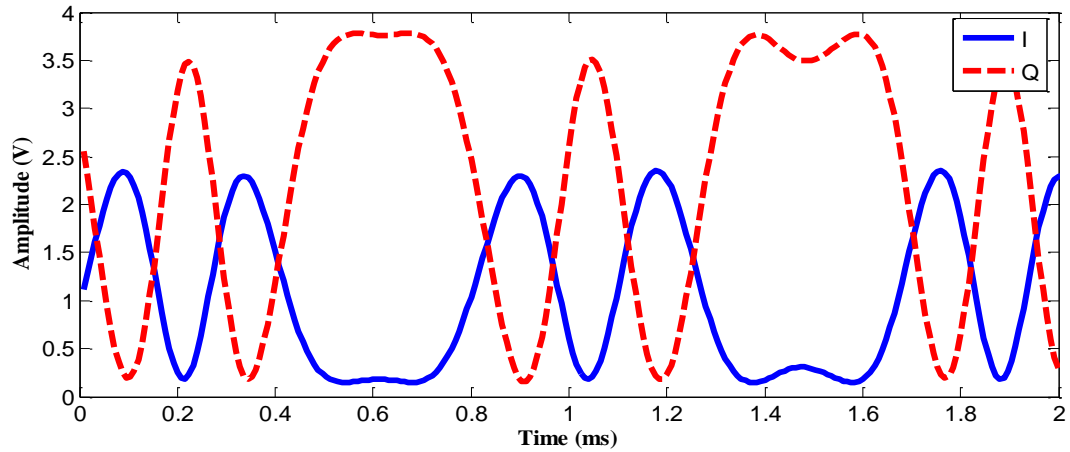
Fig. 5.11 - Low Frequency Phase Discrimination

Once optimization had been completed the low frequency RF signal was disconnected and the QPSK modulator was turned on. Fig. 5.12 shows the input and output spectrum of signals entering and leaving the SOA.
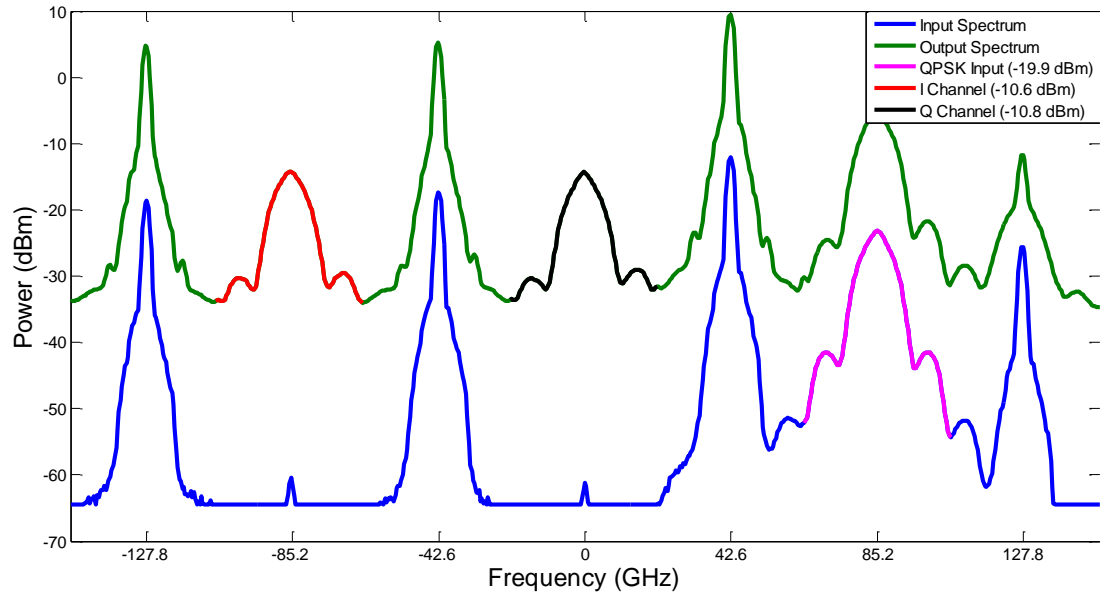
Fig. 5.12 - Input vs. Output Spectrum for QPSK phase discrimination.

A fibre to fibre gain of 9.3 dB and 9.1 dB was measured for the I and Q channels with respect to the input QPSK signal. The output pattern of the demodulated BPSK signals was recorded on a DSO, and compared to the two 2^{10}-1 bit PRBS input patterns which drove the QPSK modulator. This ensured correct system operation. The relative decorrelation between the two input patterns was identical to that of the two output demodulated BPSK signals. Eye diagrams were also recorded and are shown in Fig. 5.13. Due to a slow phase drift of the QPSK signal relative to the four pumps, measuring the eye diagrams directly was not possible. Because of this the eye diagrams were generated

offline from multiple pattern lengths saved on the DSO. Clear and open eyes, with Q factors of ~20.9 dB and ~20.1 dB, were observed for the I and Q channels. A comparison with the input Q factor was not possible as the input QPSK signal was phase modulated. Further optimization of the pump amplitudes and phases was prevented due to the phase drift of the QPSK signal with respect to the four pumps due to the interferometric nature of the system. This phase drift also prevented bit error rate (BER) measurements from being performed but could be prevented with a phase stabilization system similar to [109] or [107].
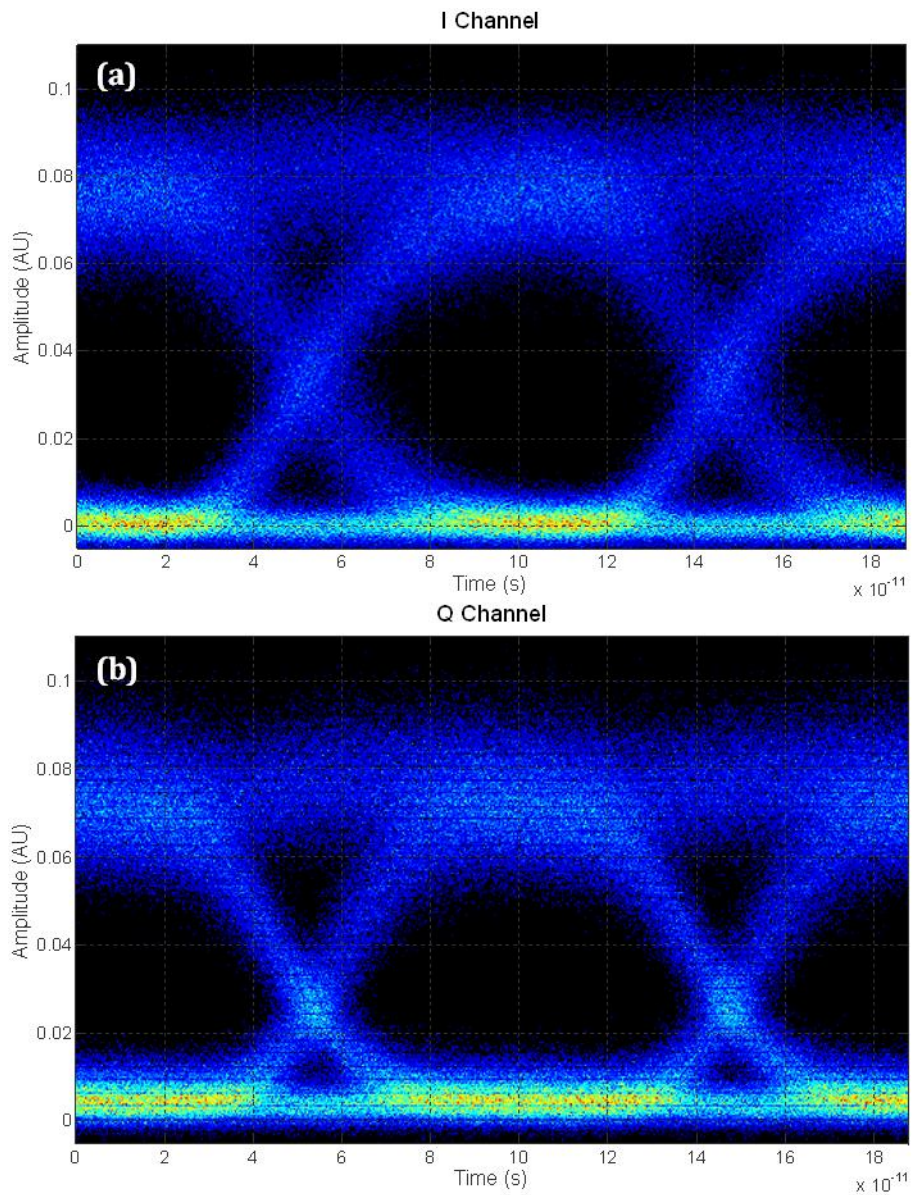
Fig. 5.13 – Demodulated eye diagrams for (a) I channel (b) Q channel.

5.6 Summary

We have shown experimentally that SOAs are efficient as nonlinear mixing devices over a broad wavelength range and provide frequency conversion gain for signal-pump difference frequencies that are sufficiently large for most telecommunications applications. There are two mechanisms by which frequency conversion can be made sensitive to signal phase: either the magnitude of the power beats can vary with the phase of the signal relative to the pump inputs or the output can be the superposition of more than one modulation product (both mechanisms can be combined). The second mechanism permits the generation of additional outputs proportional to different phase components of the signal.

This chapter demonstrated that SOAs can provide phase-sensitive frequency conversion at 40 Gbaud with conversion gain by adapting a previously reported four-tooth frequency comb scheme [13, 93]. With this arrangement, the QPSK signal was converted into two BPSK outputs at different frequencies, each comprising multiple vector components. This scheme was experimentally demonstrated for the first time by separating a 10.65 Gbaud QPSK signal into two 10.65 Gbit/s BPSK signals at different frequencies. These BPSK signals were then demodulated using a DI and clear and open eye diagrams were observed for both the I and Q channels. Q factors of ~20.9 dB and ~20.1 dB were measured for the I and Q channels respectively. Gains of 9.3 and 9.1 dB were also observed relative to the input QPSK signal at the output of the SOA, showing one of the advantages of using SOA as a mixing element.

Since this scheme separates the I and Q channels of a QPSK signal it could be used to demultiplex data in an optical node, separating the data to different frequencies and routing it down different optical paths. This technique could also be used as part of an all-optical QPSK regenerator and could also be advantageous in resolving higher order quadrature modulated amplitude (QAM) formats into their in-phase and quadrature components.

6.

Clock Recovery of Phase Modulated Optical OFDM Superchannel

All-optical signal processing in semiconductor optical amplifiers (SOA) can be used in many applications, amongst which is recovering the clock of optical signals. This chapter provides a detailed analysis of an all-optical clock recovery technique for phase modulated orthogonal frequency division multiplexing (OFDM) superchannels, first demonstrated in M.J. Power *et al* [15]. Included are the experimental measurements taken and numerical simulations developed, providing a detailed analysis of this method. Specifically, four-wave mixing (FWM) in a SOA was used to strip the modulation from the subcarriers of a 53.54 Gbit/s BPSK optical OFDM superchannel before two subcarriers were filtered out and beat together in a photodiode, thus recovering the clock. The tolerance of this system was experimentally tested both to degradations in the optical signal-to-noise ratio (OSNR) and to transmission over various lengths of single-mode fibre (SMF).

6.1 Introduction

Recovering the clock of a transmitted signal is an integral part of optical telecommunications. Decoding the data from any received optical signal requires both a decision circuit and a clock-recovery circuit. A clock recovery circuit is required to isolate a frequency component, Δf, equal to the bitrate, B, of the transmitted optical signal. This frequency component provides

information regarding the bit slot ($T_B = 1/B$) and synchronises the decision circuit to ensure a decision is performed at an optimal time within the bit slot, T_B, of the received signal. The decision circuit samples the output from a linear channel, at a sampling time determined by the clock-recovery circuit and compares the output to a threshold level to determine whether a bit 0 or bit 1 was received [1]. An example eye diagram can be seen in Fig. 6.1 showing the threshold level, decision time and the bit period, T_B.
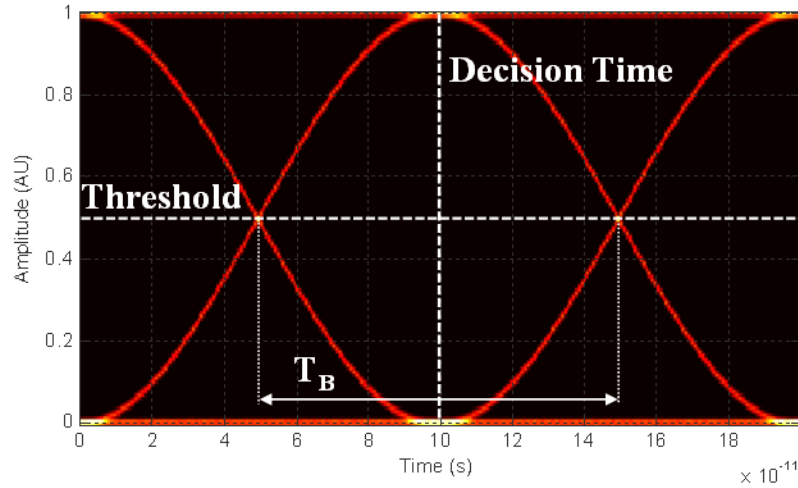
Fig. 6.1 – Example eye showing threshold level and decision time.

When two optical frequency components are injected into a photodiode the power envelope of the beating between them produces a sinusoidal signal at their frequency separation. In return-to-zero on-off keying (RZ-OOK) modulation format, shown in Fig. 6.2(a), there are multiple optical frequency components separated by the bitrate, *B*, two of which can be filtered out using a narrow BPF and injected into a photodiode to recover a clock, Δf (where $\Delta f = B$), due to this beating. Recovering the clock in non-return-to-zero on-off keying (NRZ-OOK) data is more difficult due to the absence of multiple optical frequency components, as shown in Fig. 6.2(b). In general, clock recovery of NRZ data is achieved by all-optically converting it to a PRZ (pseudo return-to-zero) signal, which will produce the desired discretely separated frequency components. The clock is then obtained in the same manner as RZ data. This modulation conversion from NRZ to PRZ can be performed in nonlinear material such as SOAs [110] and highly nonlinear fibre (HNLF) [111] but can also be achieved using a delay interferometer (DI) [112]. Since the data signal is processed in the optical domain to produce the desired frequency components,

these are known as all-optical clock recovery techniques. It is a well-established field having many different methods of all-optical clock recovery for both RZ-OOK and NRZ-OOK modulation formats including injection-locking [113, 114] and optical phase locked loops [115].
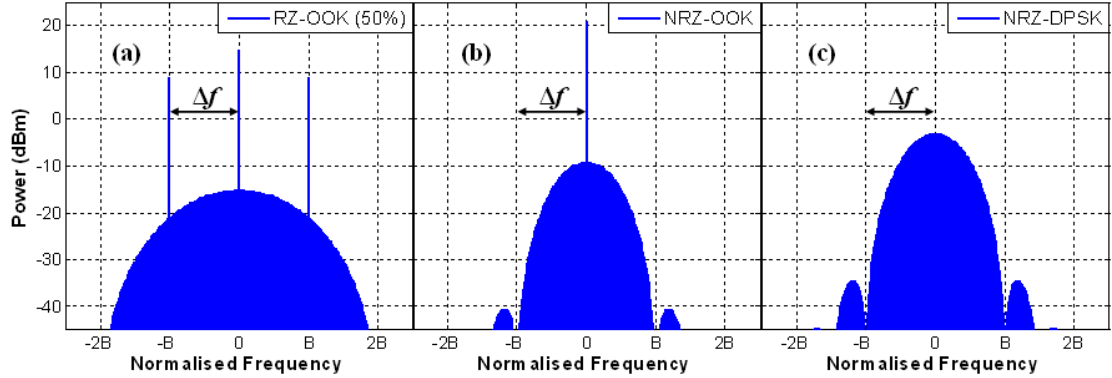
Fig. 6.2 – Format spectrum comparison: (a) RZ-OOK (50%). (b) NRZ-OOK. (c) BPSK. Horizontal axis normalised to the bitrate, *B*.

Phase modulated formats such as binary phase shift keying (BPSK), shown in Fig. 6.2(c), are increasingly common in today's optical networks due to their increased spectral efficiency, increased tolerance to dispersion, resistance to nonlinear effects, and increased receiver sensitivity when compared to OOK modulated signals [6]. However, recovering the clock from such carrier-less signals is challenging. The use of digital signal processing (DSP) in conjunction with a coherent receiver is frequently used as this can recover the clock as well as provide impairment compensation and reconstruction of the signal [116, 117], and as a result DSP has also been suggested for use in an optical node [118]. DSP can be computationally intensive particularly in long haul transmission where high capacity networks, commonly using 'Superchannels', are required. The addition of an all-optical clock recovery system either within the optical node or at the end-point receiver could ease this computational burden, as well as provide other advantages mentioned later in this chapter.

Modern optical communication networks require spectrally efficient schemes to meet ever-growing capacity demands. Transmission schemes using closely spaced frequency channels, called 'Superchannels', offer an attractive solution for capacities exceeding 400Gbit/s [116, 117]. The use of flexible grid wavelength-division multiplexing (WDM), with a granularity of <12.5GHz, has recently been suggested in the updated G.694.1 ITU-T recommendations

(02/2012), demonstrating the demand for decreased channel spacing. These closely spaced frequency channels are commonly generated from a single laser source, providing frequency locking between them. Any fluctuation in the output frequency of the laser source (due to temperature variations, etc.) is then observed by all channels. If a laser source is used for each individual channel then the frequency spacing between channels may vary. All-optical OFDM is one format that could be easily used for flexi-grid implementations. OFDM enables high capacity with high spectral efficiency [119], and with transmission impairments dominated by the baud rate of each optical subcarrier [120]. In the context of this chapter, the key property of an OFDM superchannel is that its channel spacing, *Δf*, is the same frequency as the bitrate, *B*, used to encode the data on each channel, as shown in Fig. 6.3(a). The all-optical clock recovery technique detailed in this chapter relies on this property of OFDM superchannels. If this system was implemented in a WDM system (see Fig. 6.3(b)) where the channel spacing, *Δf*, differs from the bitrate, *B*, the recovered clock would be at the same frequency as the channel spacing, *Δf*, and could not be used for the decision timing of the recovered optical signals, since *Δf* > *B*. Some superchannels variations also have baud rates/bitrates smaller than channel spacing (*Δf* > *B*), such as Nyquist WDM. Even though the recovered clock may not be used for decision timing the clock may still be useful in regenerating the original comb (frequency channels) or in tracking the relative phase between channels.
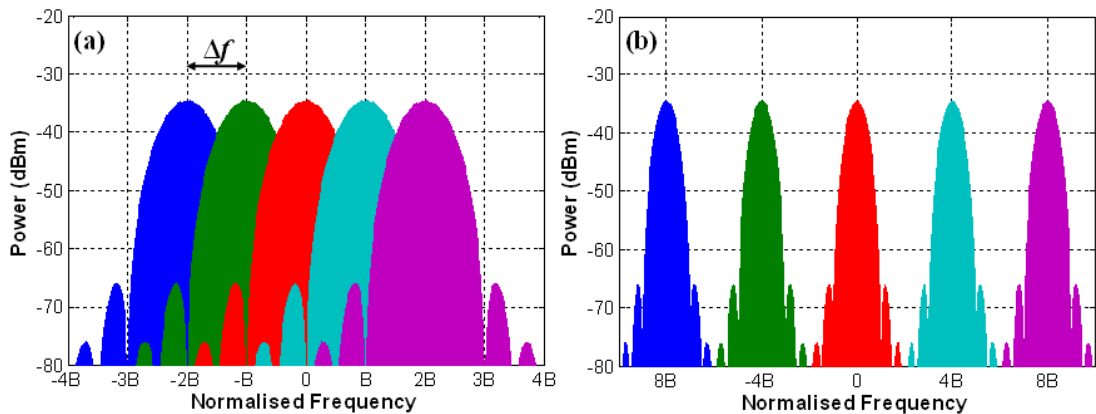
Fig. 6.3 – (a) All-optical OFDM superchannel. (b) Wavelength Division Multiplexing. Frequency axis normalised to the bitrate, *B*

As detailed in Chapter 2, FWM is a well-known non-linear process and has been extensively used in many phase sensitive applications such as phase

sensitive amplification [97] and phase sensitive frequency conversion [13, 14, 93] (described in Chapter 5). This all-optical clock recovery method uses FWM in a SOA, to recover the carrier components from a BPSK signal [103], which in turn may be used to recover the clock. This produces an analogue clock linked to the OFDM signal and has many uses in addition to controlling the decision circuit, including synchronization, phase tracking [121], and regeneration.

The structure of this chapter is as follows: Section 6.2 discusses the principle of operation of this clock recovery technique before Section 6.3 details the experimental setup used and the results obtained. Section 6.4 provides simulation results verifying correct operation of this all-optical technique. Finally, the results of this chapter are then summarised in Section 6.5.

6.2 Principle of Operation

The all-optical clock recovery approach used in this experiment is shown in Fig. 6.4. Two adjacent subcarriers filtered from an optical OFDM superchannel with channel spacing of Δf and modulated with BPSK data at Δf are injected into a SOA along with a continuous wave (CW) pump. FWM between the CW pump and the filtered superchannel gives rise to two idlers located at $2fs_1 - f_P$ and $2fs_2 - f_P$, where fs_1 and fs_2 are the carrier frequencies of each subcarrier and f_P is the carrier frequency of the CW pump. These idlers will have double the frequency spacing ($2\Delta f$) and double the phase modulation (0 and 2π) of the original subcarriers [103]. Since this is an identical phase relationship ($e^{i0} = e^{i2\pi}$) these idlers will be stripped of any phase modulation. Beating these two idlers together in a photodiode will give a clock at their frequency spacing of $2\Delta f$. This is double the original clock frequency used to produce the OFDM superchannel but can be easily down-converted in the electrical domain to the original clock frequency, Δf.
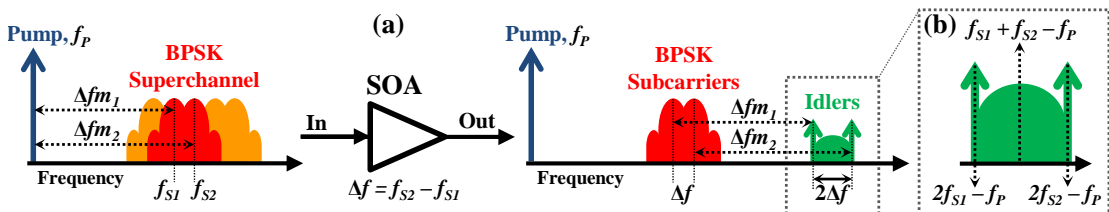
Fig. 6.4 - Principle of operation. (a) Superchannel (orange + red), two filtered subcarriers (red), and idlers (green). (b) Expanded idler view.

As mentioned in Chapter 2, it is possible to view FWM in a SOA as a two-stage process, in which beating between the subcarriers and the CW pump modulates the carrier density in the SOA at frequency differences *Δfm₁* and *Δfm₂*, shown in Fig. 6.4(a). This carrier density fluctuation then in turn modulates the amplitude and phase of all signals passing through the SOA. The two subcarriers, *fs₁* and *fs₂*, are thus modulated by *Δfm₁* and *Δfm₂* respectively to produce sidebands at *fs₁ + Δfm₁ (= 2fs₁ – fₚ)* and *fs₂ + Δfm₂ (= 2fs₂ – fₚ)*. This can be seen in the expanded idler view in Fig. 6.4(b). If the injected subcarrier at *fs₁* carries a phase modulation Δφ₁ and the injected subcarrier at *fs₂* carries a phase modulation Δφ₂, then *Δfm₁* will similarly contain the phase modulation Δφ₁ and *Δfm₂* will contain Δφ₂. As a result, the idlers produced are wavelength converted subcarriers each of which has been further phase modulated with the exact same phase information already encoded onto the subcarriers, i.e. *fs₁ + Δfm₁* will carry the phase modulation 2Δφ₁, as shown in Fig. 6.5(c) and (d).
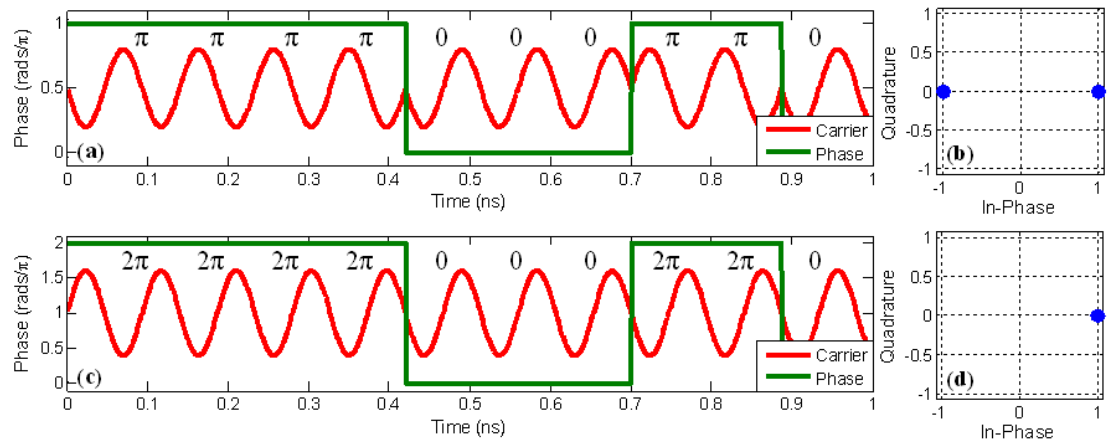
Fig. 6.5 - (a) Subcarrier. (b) Subcarrier constellation. (c) Idler. (d) Idler constellation.

Since both subcarriers, *fs₁* and *fs₂*, will be modulated by beat components, *Δfm₁* and *Δfm₂*, an idler is also produced at *fs₁ + fs₂ – fₚ*. This idler is the combination of the subcarrier at *fs₁* modulated by *Δfm₂* and the subcarrier at *fs₂* modulated by *Δfm₁*. Its power is dependent on the relative polarisation and phase between subcarriers at the input to the SOA. The phase modulation of this idler is the sum of Δφ₁ and Δφ₂. In a real system the two data streams on subcarriers *fs₁* and *fs₂* will be decorrelated, which means that this component will not be stripped of its phase modulation (see Fig. 6.4(b)), and hence it is not possible to use it to recover the clock.

6.3 Experiments

This section details the experimental setup used as well as the results obtained, including optical spectra, RF spectra and time domain traces. Various aspects of this clock recovery system were also investigated, such as its performance over various fibre transmission lengths and its tolerance to degradations in OSNR.
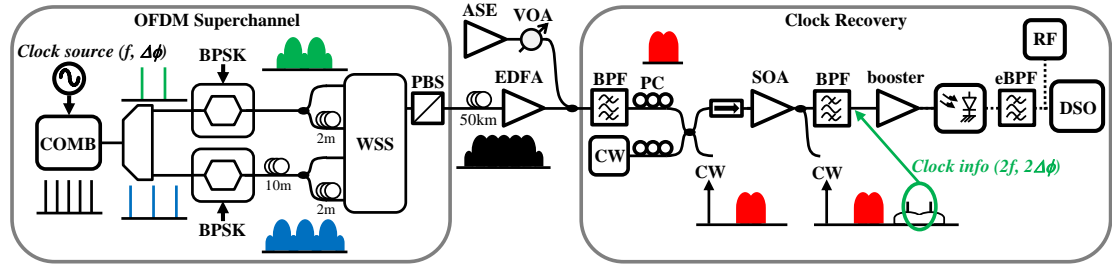
Fig. 6.6 - Experimental setup. (WSS = wavelength selective switch, PC = polarisation controller, RF = RF spectrum analyser, eBPF = electronic bandpass filter, VOA = variable optical attenuator).

The experimental setup is shown Fig. 6.6. A distributed feedback laser (DFB), with a wavelength of ~1552.8 nm, was used in conjunction with two Mach-Zehnder modulators (MZMs) in series, each driven by a sinusoidal 10.7089 GHz clock signal from an oscillator. Both MZMs were driven by $2V_\pi$ and the bias of each was optimised as well as the phase difference between each drive signal to produce a five channel comb with a flatness smaller than 0.3 dB and a side-mode suppression ratio (SMSR) of >16 dB, as shown in Fig. 6.7(a). A delay interferometer, with a free spectral range (FSR) of 21.3 GHz, was used as a disinterleaver to separate the odd and even channels of the comb to separate output ports, the spectra of which is shown in Fig. 6.7(b).
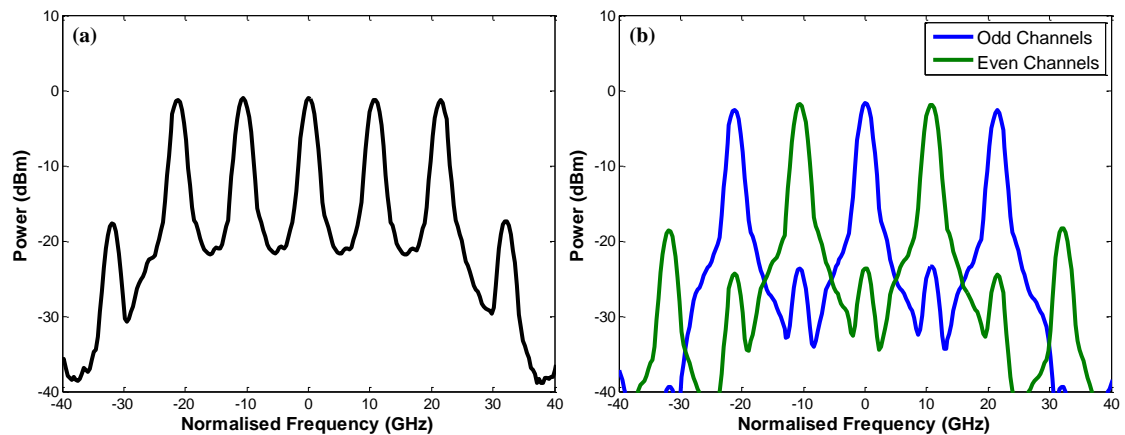
Fig. 6.7 - (a) Comb. (b) Odd and even channels. Figures normalised to the central carrier frequency.

To properly mimic a real system several steps were taken to decorrelate all the subcarriers. Firstly, the odd and even channels were independently modulated using two MZMs. A pseudo-random binary sequence (PRBS) pattern generator with two output ports and synchronised to the same 10.7089 GHz clock oscillator that produced the comb, was used to generate two PRBS data streams. A 10.7089 Gbit/s 2^{31}-1 PRBS signal was generated at one port and a 10.7089 Gbit/s 2^{31}-1 inverse PRBS signal at the other. Both of these data streams were amplified, using RF amplifiers, before driving the odd and even channel MZMs. Both MZMs were biased at the null and were driven by $2V_\pi$, resulting in the odd and even channels being independently modulated with BPSK data, both of which can be seen in Fig. 6.8(a).
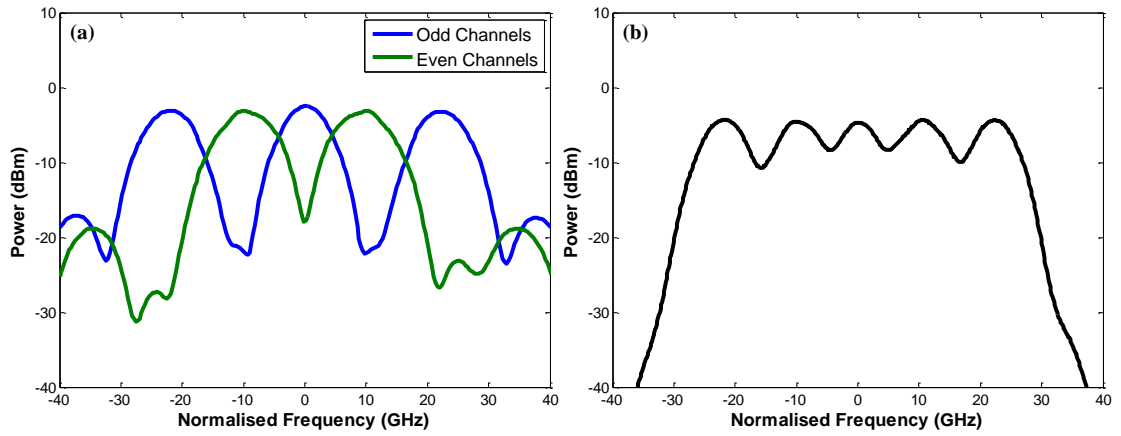
Fig. 6.8 - (a) Odd & even BPSK channels. (b) 53.54 Gbit/s BPSK OFDM superchannel.

To achieve further decorrelation between the odd and even channels, 10 m of SMF was added to the optical path of the odd channels. Both paths were then split using 50:50 couplers. Subsequently one path of each split was then delayed using 2m of SMF before all four optical paths were injected into a wavelength selective switch (WSS), as shown in Fig. 6.6. The WSS is a four port programmable filter which was used to select a different channel from each of the four input ports except port 4 where channel 1 and 5 were selected, as shown in Fig. 6.9. Since each of the four optical paths have different lengths, all channels except the 1st and 5th were decorrelated with respect to each other [89]. The variation in loss between the MZMs, between the fibre lengths, and between the splitters resulted in a power difference between the five channels at the input to the WSS. The WSS could correct for this by adjusting the attenuation in the pass band of each of the four filters such that the power in

each channel at the output of the WSS was equal, also shown in Fig. 6.9. The recombination of the five channels produced a decorrelated 53.54 Gbit/s BPSK OFDM superchannel at the output of the WSS, as shown in Fig. 6.8(b) and Fig. 6.10(a) (black trace).
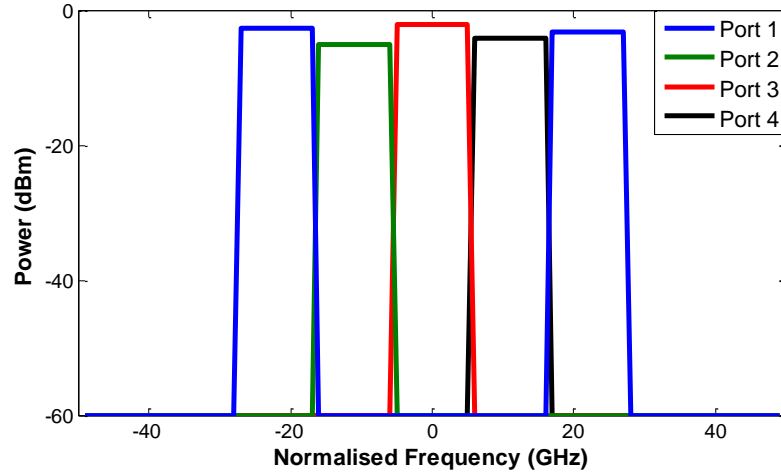
Fig. 6.9 – Input filter of each port of the WSS.

A polarisation beam splitter (PBS) was used to ensure that all subcarriers of the superchannel were co-polarised before transmission over a 50 km span of SMF followed by an erbium-doped fibre amplifier (EDFA). Another EDFA with no input was used to produce broadband amplified spontaneous emission (ASE), the power of which was controlled using a variable optical attenuator (VOA). This ASE was combined with the received superchannel in a 90:10 coupler before both were injected into a band-pass filter (BPF), as in Fig. 6.6. This method provided control over the optical OSNR of the received superchannel. In principle any two adjacent subcarriers may be filtered out using the BPF. Using two subcarriers at the edge of the superchannel will ease the filter bandwidth requirement, however, in this experiment we extracted the second and third subcarrier, shown in Fig. 6.10(a) (red trace), to demonstrate that any can be used. The pump (+3 dBm) was combined with the subcarriers (-8.2 dBm), (spectra are shown in the red trace of Fig. 6.10(b)) and passed through an isolator before injection into the SOA. The SOA used in this experiment was an InGaAsP/InP buried heterostructure multiple quantum well (MQW) SOA with a confinement factor of 0.18, an effective length of 1.7 mm and a small signal gain peak at 1558 nm. It had a -3 dB bandwidth of 36 nm, a small signal fibre-to-fibre gain of ~32 dB, and a fibre-to-fibre saturated gain of ~17

dB. These gain values include input and output coupling losses of 2.95 dB and 2.56 dB respectively. A 400 mA drive current was used for all results recorded in this experiment. Since both the output power and FWM efficiency of the SOA are polarisation dependent, polarisation controllers (PC) were used to maximize the output idler components.
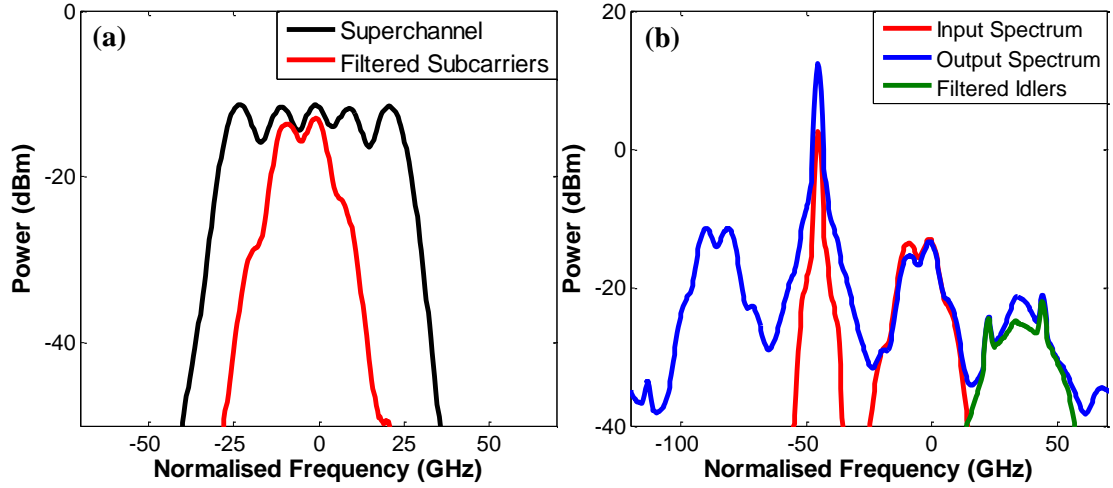
Fig. 6.10 - (a) Superchannel and filtered subcarriers. (b) Input and output optical spectrum (Resolution = 4 GHz).

At the output of the SOA, shown in Fig. 6.10(b) (blue trace), the two modulation-stripped idlers located at $2f_{S1} - f_P$ and $2f_{S2} - f_P$ were filtered out (green trace) using a square BPF, with a pass band of ~30 GHz, combined with a square notch filter, with a stop band of ~ 10 GHz, both of which were generated using a single WSS. The phase modulated idler due to the $f_{S1} + f_{S2} - f_P$ relationship is also visible, located between the two modulation-stripped idlers. Even though the SOA used in this experiment had saturated output power of ~13 dBm, the total combined power in the idlers is only -17.1 dBm after filtering. To accurately detect the signal on the photodiode, the idlers' power was amplified to ~0 dBm, using an EDFA. A linear SOA could be used instead of an EDFA, since they can provide small signal gains of 10-20dB and the clock recovery system could then be integrated into a single package. Due to the larger noise figures associated with SOAs (>6 dB) compared to EDFAs (>3 dB) the signal detected at the clock will be degraded. However, as the measured recovered clock SNR, described later in this chapter, is >36 dB, 3 dB of additional noise at the photodiode would be negligible. The power envelope of the beating between the idlers in the photodiode occurs at their frequency separation and produces a sinusoidal clock signal at 21.4178 GHz. The output signal from the photodiode

was amplified using a narrowband electrical amplifier, with a 3 dB bandwidth of ~5 GHz before it was passed through a narrowband electrical BPF, with a 1 dB pass band of ~4 GHz, to reduce noise. The output of the electrical BPF was captured on a RF spectrum analyser (Fig. 6.11(a)) and on a digital sampling oscilloscope (DSO) (Fig. 6.11(b)). The recovered clock (21.4178 GHz) had twice the original clock frequency (10.7089 GHz) but can be easily electrically down converted. The raw clock data measured on the RF spectrum analyser had a root mean square (RMS) phase noise of 0.072 radians (between 100 Hz – 10 MHz) and a signal-to-noise ratio (SNR) of 36.6 dB Compared with an input clock SNR of 63 dB and a RMS phase noise of 0.0074 radians, this shows some degradation but this is expected due to the noise figure associated with SOAs and EDFAs.
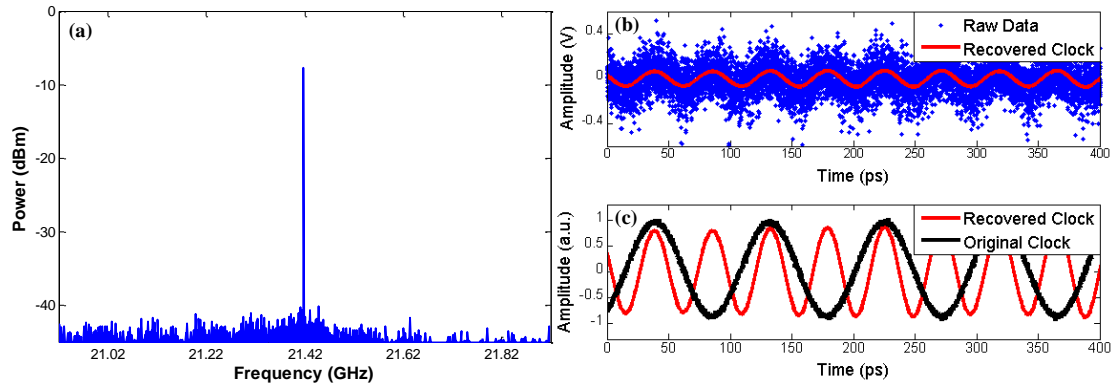
Fig. 6.11 - (a) RF spectrum (Bandwidth = 30 kHz) (b) Raw data vs. Recovered clock.
(c) Recovered clock vs. Original Clock

The DSO image of the clock is shown in Fig. 6.11(b) (blue data), where it is evident that a large amount of broadband noise is falling on the detector. A narrowband analogue bandpass filter, with a 3 dB bandwidth of 3 GHz, was applied in post-processing to the raw clock data to extract the clean 21.4178 GHz sinusoidal clock shown as the red solid curve of Fig. 6.11(a). A time domain comparison of the original clock with the recovered filtered clock signal is shown in Fig. 6.11(b). A plot of the recovered clock vs. the original clock can be seen in the Lissajous figure in Fig. 6.12, demonstrating the 2:1 relationship between them.
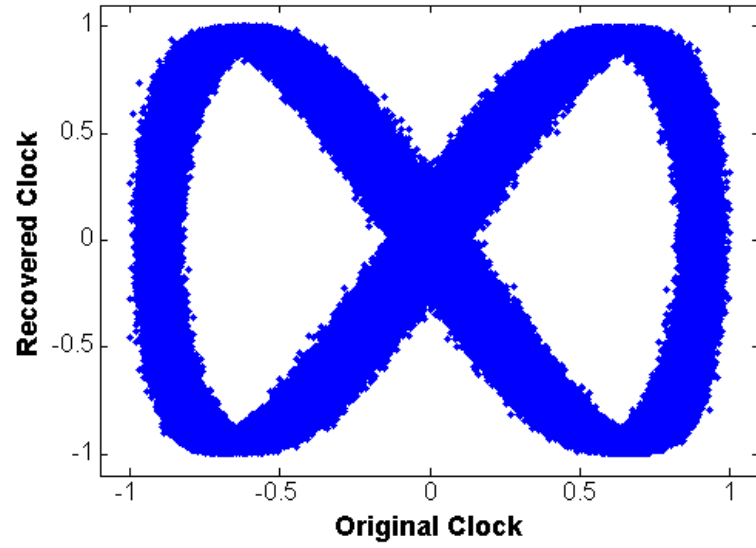
Fig. 6.12 – Lissajous plot of the recovered clock vs. the original clock.

The polarisation sensitivity of the phase modulated idler produced at $f_{S1} + f_{S2}$ – f_P is shown Fig. 6.13. In Fig. 6.13(a) (blue trace), the superchannel was co-polarised before transmission and only the combined polarisation of the two filtered subcarriers, at the receiver, which were injected into the SOA was optimised, along with the CW pump. In Fig. 6.13(b) (blue trace), however, the superchannel was not co-polarised before transmission and the relative polarisation between the two filtered subcarriers injected into the SOA was optimised, along with the CW pump. The first method requires a notch filter to help suppress the phase modulated component located between the two modulation stripped idlers, Fig. 6.13(a) (green trace), whereas the second method does not, Fig. 6.13(b) (green trace). The disadvantage of the second method is that control over the individual polarisation of each subcarrier is required, meaning that each of the subcarriers has to be individually filtered from the received superchannel and adjusted using separate polarisation controllers, before recombination and injection into the SOA. This added complexity reduces the value of this method and as such using a notch filter at the output of the SOA is preferred. It is important to note that in this comparison the input powers of the pump and subcarriers to the SOA were different as well as the frequency spacing between the pump and subcarriers. However, neither will affect the size of the phase modulated component without altering the modulation-stripped idler power also.
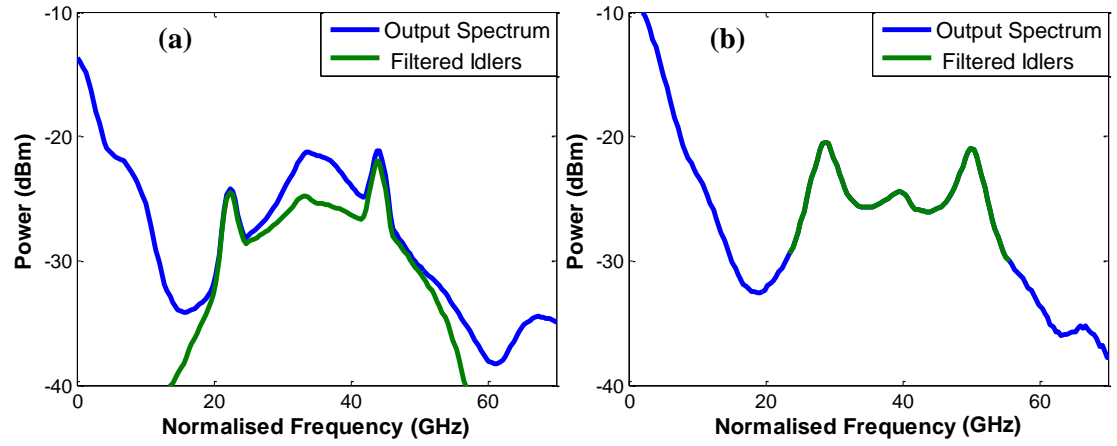
Fig. 6.13 – SOA output spectrum; (a) Relative polarisation between subcarriers not optimised. (b) Relative polarisation between subcarriers optimised.

The input OSNR (0.1 nm bandwidth) of the entire BPSK superchannel was swept and the resulting SNR measured on the RF spectrum analyser was recorded. The OSNR here is defined as the ratio between the integrated power of the superchannel to the integrated power of the ASE for the superchannel's optical bandwidth. A plot of the input OSNR vs. measured clock SNR is shown in Fig. 6.14(a) below. This clock recovery system was clearly tolerant to degradations in the received OSNR, which varied from 27 dB to 7.5 dB with less than 1 dB degradation in the clock SNR. Larger degradations were only observed for severely impaired OSNRs.
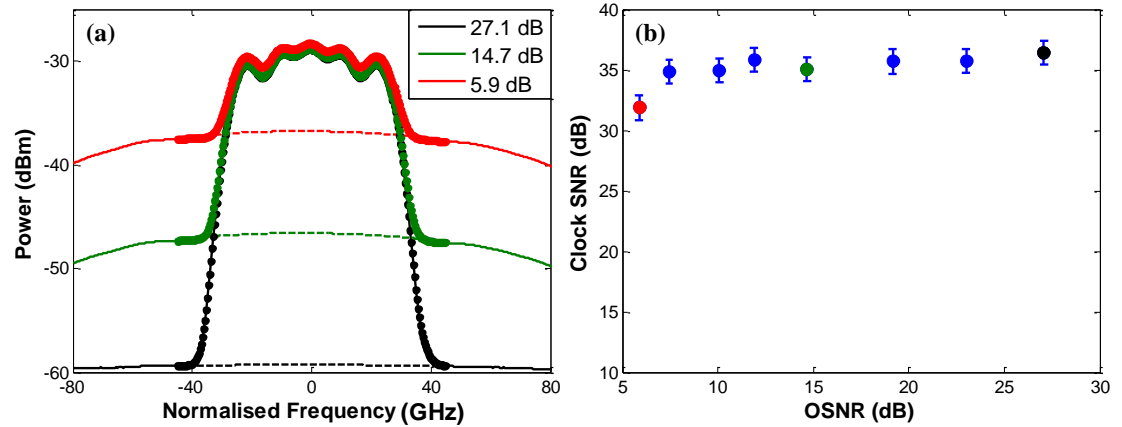
Fig. 6.14 - (a) Various superchannel OSNR spectrum; Dashed lines = projected ASE. (b) OSNR vs. recovered clock SNR.

As two subcarriers are extracted using a BPF after the addition of ASE to the superchannel, any broadband ASE outside the bandwidth of this filter is suppressed. The total power into the SOA does not change with the addition of ASE; only the OSNR of the subcarriers is degraded. This means the FWM conditions in the SOA are unaffected, until a sufficiently small OSNR is injected.

Since in a real system the required OSNR to detect a BPSK signal is >11 dBm [8], the OSNR, in this scenario, will never be low enough to significantly degrade the recovered clock SNR.
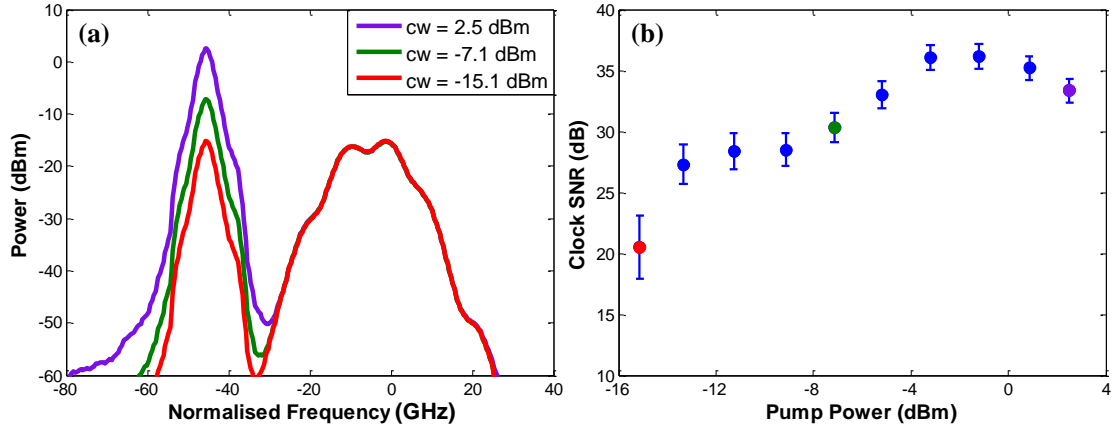
Fig. 6.15 - (a) Input spectrum for various CW pump powers. (b) Pump power vs. clock SNR.

The performance of the clock recovery system as a function of FWM efficiency was also investigated by analysing the recovered clock SNR for various CW pump input powers, changing the pump-signal ratio. Fig. 6.15(b) shows the overall results, where an optimum CW pump power between -3.5 dBm and -1 dBm was observed for an input signal power to the SOA of -9.8 dBm.

The recovered clock SNR for transmission of the superchannel over various lengths of SMF was measured whilst maintaining constant CW pump and input signal powers to the SOA. The results for back-to-back, 20 km, and 50 km of SMF is recorded in **Table 6.1** below. The pump and signal input powers to the SOA were kept constant for each measurement.

Table 6.1 - Fibre length vs. recovered clock SNR

Fibre Length	Clock SNR
Back-to-back	39.9
20 km	38.6
50 km	36.6

6.4 Simulations

The all-optical superchannel clock recovery scheme was simulated using a numerical model developed by my colleague Dr. Roderick P. Webb [13, 93] and described in detail in the appendix. An OFDM superchannel was generated with

five subcarriers spaced 10 GHz apart, each modulated with independent 2^{10} De Bruijn (DBS) BPSK patterns at 10 Gbit/s, to produce a 50 Gbit/s BPSK OFDM superchannel. A 2^{10} pattern was used instead of a 2^{31} to reduce the complexity and computation time of the simulations. A DBS pattern was used instead of a PRBS pattern to help improve the decorrelation between the subcarriers and the reason for this is explained in more detail in Section 8.2 of the appendix.

Further decorrelation between subcarriers was achieved by inverting and delaying the DBS pattern of each subcarrier with respect to the previous one. Due to the use of a DBS pattern the optical spectrum differs slightly from that of PRBS BPSK signal, producing a slight dip where the carrier is suppressed, shown in the superchannel spectrum in Fig. 6.16(a). A dispersion of 1ns/nm was also applied to the superchannel, representing transmission through ~59 km of SMF for a fibre dispersion of 17 ps/nm.km. The effects of dispersion on the subcarriers can be seen in the time domain trace of the five subcarriers shown in Fig. 6.16(b), where the rising and falling edges of the do not align and the signal has been distorted.
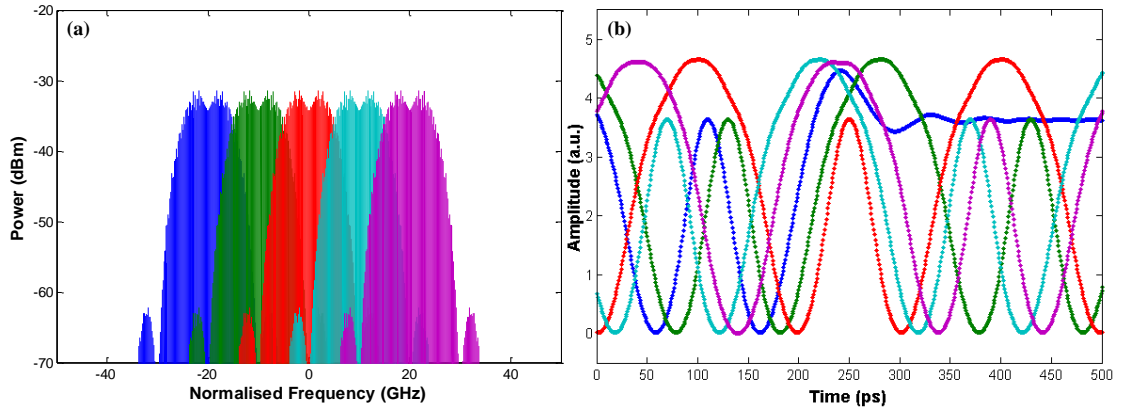
Fig. 6.16 - (a) Superchannel spectrum. (b) Dispersed time domain subcarriers. Colours represent each individual subcarrier in both (a) and (b).

Two of the subcarriers were filtered out (green and red traces in Fig. 6.16(a) and Fig. 6.17(a)) using an analogue BPF and combined with a CW signal located at -80 GHz from the centre of the superchannel, as shown in Fig. 6.17(a).
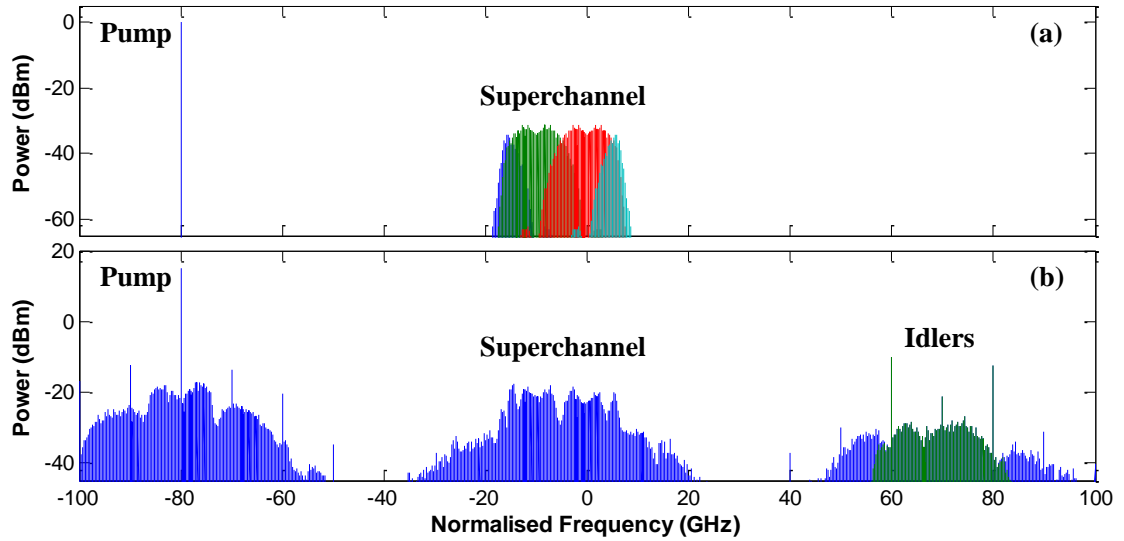
Fig. 6.17 - (a) SOA input spectrum - Pump and two filtered subcarriers. (b) SOA output spectrum (blue), Filtered idlers (green)

The simulated output spectrum of the SOA can be seen in Fig. 6.17(b), where the produced idlers are clearly stripped of phase modulation, indicated by the spikes in the spectra. The two idlers produced from the *2fs – f$_P$* relationship, located at +60 GHz and +80 GHz, are extracted using an analogue BPF (highlighted in green in Fig. 6.17(b)) before they are combined and thereby beat to recover a clock at 20 GHz. An idler is also produced due to the *fs$_1$ + fs$_2$ – f$_P$* relationship and is located at +70 GHz. As mentioned previously this idler is dependent on the relative data streams of both subcarriers as well as their relative phases. The RF spectrum of the beating between these filtered idlers can be seen in Fig. 6.18(a) where a strong clock signal is observed with a SNR of ~25 dB. A time domain comparison between the recovered clock signal and the original clock signal is shown in Fig. 6.18(b).
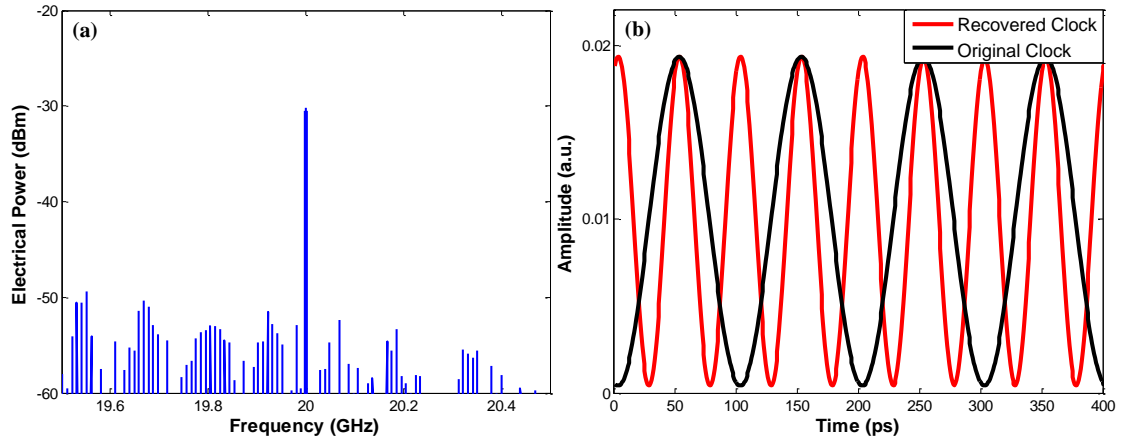
Fig. 6.18 - (a) RF spectrum of extracted idlers. (b) Recovered clock (20 GHz) vs. original clock (10 GHz)

It is also possible to recover the clock without filtering just two subcarriers from the superchannel. Injecting the entire superchannel into the SOA along with a CW pump located at -140 GHz, as shown in Fig. 6.19(a), will modulation strip every subcarrier, as with the two channel case. The simulated output spectrum of the SOA can be seen in Fig. 6.19(b). Two of the modulation-stripped idlers are filtered out (highlighted in green) and the 20 GHz clock is recovered from them. There are two drawbacks to this approach. Firstly, a larger pump spacing (140 GHz) is required to ensure full separation between the superchannel and idlers at the output of the SOA. This will result in lower power idlers (∼-4.5 dB), due to the dependence of the FWM efficiency in SOAs on the pump-signal frequency spacing [93]. This is clearly seen when comparing the powers of the idlers in Fig. 6.17(b) and Fig. 6.19(b). Secondly, the presence of extra subcarriers will produce more phase modulated idlers, similar to the fs_1 + fs_2 – f_P component mentioned in section 2, which will overlap with the modulation-stripped idlers and will be seen as additional noise on the recovered clock. For example, the second idler, located at +120 GHz in Fig. 6.4(b), will have noise added from the beating between the CW pump and the central subcarrier (located at 0 GHz) modulating the first subcarrier (located at -20GHz). However, when only two subcarriers are used for the FWM process only one idler with phase modulation is produced. This is equidistant between the two modulation-stripped idlers, a condition which minimises the additional noise at the photodetector. These disadvantages result in a reduced recovered clock SNR of ∼18 dB.
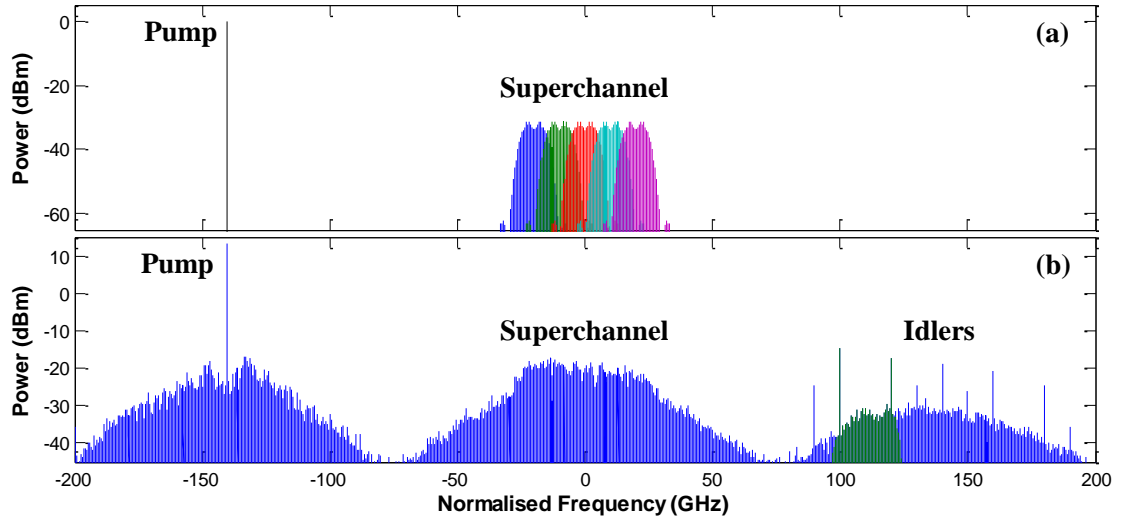
Fig. 6.19 - (a) Input Spectrum - CW pump and BPSK superchannel. (b) Output spectrum - filtered idlers highlighted in green.

The effect of phase noise present in the superchannel on the clock recovery was also investigated through simulations of the two filtered subcarrier case. Phase noise added to the entire superchannel will not have any effect on the recovered clock SNR since the same phase noise will be added to each subcarrier and, hence, the relative phase noise between subcarriers will be zero. Since we recover the clock from beating two of the modulation-stripped idlers together, both of which are dependent on the two injected subcarriers, only phase noise that alters the relative phase between subcarriers should have an effect on the system. Varying degrees of phase noise was added to the central subcarrier, located at 0 GHz, and the recovered clock SNR was recorded, as shown in Fig. 6.20(a).
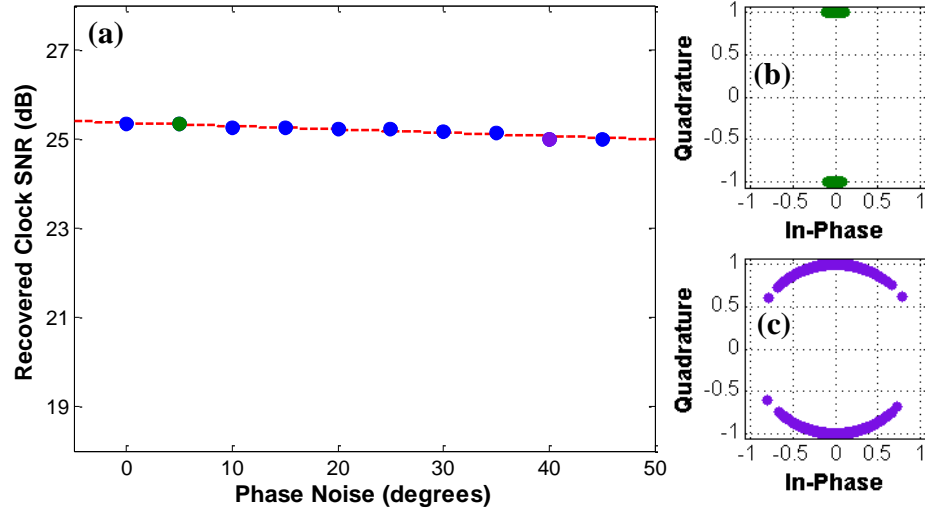
Fig. 6.20 – (a) Recovered clock SNR vs. phase noise . (b) Constellation diagram of central subcarrier with 5 degrees of phase noise. (c) Constellation diagram of central subcarrier 40 degrees phase noise.

As can be seen from Fig. 6.20(a), the addition of phase noise to the central subcarrier had very little effect on the recovered clock SNR. Sweeping from 0 to 45 degrees of phase noise degraded the clock SNR by less than 0.5 dB.

6.5 Summary

In this chapter we have experimentally demonstrated and simulated a novel all-optical clock recovery scheme for phase modulated superchannels. This system is capable of recovering a clock with twice the frequency from a BPSK modulated optical OFDM superchannel using FWM in SOAs. A 53.54 Gbit/s BPSK superchannel, with 10.7089 GHz spacing between subcarriers, was transmitted over 50 km of SMF before extracting a clock signal at 21.4178 GHz, with a SNR of 36.6 dB and a RMS phase noise of 0.072 radians. This system was shown to be very tolerant to degradation of the input superchannel OSNR, as sweeping the OSNR from 27 dB to 7.5 dB reduced the recovered clock SNR by less than 1 dB. Transmission over various lengths of SMF did not degrade the quality of the recovered clock greatly, with only a 3.3 dB difference measured in the clock SNR between back-to-back and 50 km of SMF. In simulation the effect of phase noise on the clock recovery system was tested. Sweeping the phase noise, on one of the subcarriers used to recover the clock, from 0 to 45 degrees produced less than a 0.5 dB drop in recovered clock SNR. This all-optical clock recovery system has the potential for integration and if used in conjunction

with a coherent receiver would reduce the complexity of the DSP required in addition to providing advantages such as synchronization, phase tracking [121], and regeneration of phase modulated OFDM superchannels.

7.

Conclusion

This thesis experimentally demonstrated multiple all-optical signal processing techniques for next generation networks. Initially the wavelength dependent nature of the gain and phase recovery curves in a long nonlinear SOA was investigated using a pump-probe setup. The gain and phase recovery times can limit the usage of semiconductor optical amplifiers (SOA) for optical switching applications. It was found that the recovery rates of this device demonstrated different recovery profiles depending on whether the pump was to the blue or to the red of the CW probe wavelength. Gain recovery times (10/90) of between 6 and 9 ps were recorded for at when pumping to the blue and at an optimum pump-probe separation (20-30 nm) [36]. The phase recovery curves showed a similar trend although they had considerably slower recovery times. In contrast, when the pump was red-shifted the gain (>30 ps) and phase recovery rates were substantially slower. Comparing the results with an experimentally verified numerical model demonstrated the Turbo-switch like behaviour of the device where the pump was effectively filtered out within the SOA. This is the first demonstration of such fast gain recovery times from a single SOA without the use of a filter or second SOA.

Chapter 4 detailed an experimental demonstration of an all-optical modulation converter capable of converting a 42.6 Gbit/s return-to-zero on-off keying (RZ-OOK) to either RZ-AMI (alternate mark inversion) or RZ-DB (duobinary) [11, 12]. This system used of two hybrid-integrated SOA-based Mach-Zehnder interferometer (MZI) gates to achieve conversion: a Dual-Output MZI and an XOR gate. The DB and AMI formats were theoretically predicted at the output of the XOR gate using a transfer function analysis as well as a comprehensive computer-based SOA model. Experimental results demonstrated open eyes for both modulation conversions and the optical

spectrums recorded matched those predicted. The importance of the carrier density recovery time and the effect of patterning on the quality of the output eye were observed by comparing 42.6 Gbit/s and 10.65 Gbit/s results for both conversions. The possibility of 3R (reshaping, retiming, and reamplification) regeneration, the ability to easily change between AMI and DB, and the advantage of outputting to any arbitrary wavelength arises from the dual active-gate approach used. Further photonic integration could improve the power consumption of this system and the use of SOAs with faster carrier recovery lifetimes could permit operation in excess of the 42.6 Gbit/s demonstrated here. This all-optical approach to DB and AMI generation could impact implementations of both high-speed transmitters and modulation converters.

In Chapter 5 the four-wave mixing (FWM) in SOAs was shown to be efficient over a broad wavelength range and that these devices can provide frequency conversion gain for signal-pump difference frequencies that are sufficiently large for most telecommunications requirements. Simulations were performed using a experimentally verified numerical model demonstrating that SOAs can provide phase-sensitive frequency conversion at 40 Gbaud [13, 93]. This scheme was then experimentally demonstrated for the first time at 10.65 Gbaud splitting a quadrature phase shift keyed (QPSK) signal into two 10.65 Gbit/s binary phase shift keyed (BPSK) signals at different frequencies. These BPSK signals were then demodulated using a delay interferometer (DI) and clear and open eye diagrams were observed for both channels. Extinction ratios of ~20 dB and ~14 dB were measured for the I and Q channels with conversion gains of 9.3 and 9.1 dB respectively [14]. Since this scheme separates the I and Q channels of a QPSK signal it could be used to demultiplex data in an optical node separating the data to different frequencies and routing it down different optical paths. This technique could also be used as part of an all-optical QPSK regenerator and could also be advantageous in resolving higher order quadrature modulated amplitude (QAM) formats into their in-phase and quadrature components.

Chapter 6 detailed the experimental demonstration and simulation of a novel all-optical clock recovery scheme for phase modulated superchannels. A clock with twice the original clock frequency was recovered from a 53.54 Gbit/s BPSK all-optical orthogonal frequency division multiplexed (OFDM) superchannel, with 10.7089 GHz channel spacing, which had been transmitted over 50 km of SMF. A clock signal with a frequency of 21.4178 GHz, a signal-to-noise ratio (SNR) of 36.6 dB and a root-mean-square (RMS) phase noise of 0.072 radians was recovered [15, 16]. This system was shown to be very tolerant to degradation of the input superchannel optical signal-to-noise ratio (OSNR), as sweeping the OSNR from 27 dB to 7.5 dB reduced the recovered clock SNR by less than 1 dB. Transmission over various lengths of single mode fibre (SMF) did not degrade the quality of the recovered clock greatly, with only a 3.3 dB difference measured in the clock SNR between back-to-back and 50 km of SMF. This all-optical clock recovery system has the potential for integration and could provide advantages such as synchronization, phase tracking [121], and regeneration of phase modulated OFDM superchannels.

7.1 Practical Limitations

When experimentally investigating any novel optical systems it is important to realise ultimate practicality of the system. The experiments detailed in this thesis are of a proof-of-principles nature, demonstrating that these techniques work. However, both the OOK to AMI/DB conversion technique, discussed in Chapter 4, and the phase sensitive frequency conversion method, discussed in Chapter 5 require relatively complex setups which would prohibit their implementation in a real optical network.

With regards to the modulation converter, further integration would help reduce loss between the two gates and negate the need for the linear SOAs reducing the complexity, but the need for both a local clocked probe as well as a CW probe is not very attractive. Even eliminating the two linear SOAs will leave four SOAs integrated in the gates which is not ideal as these devices can be quite power hungry. In recent years optical communications systems have been migrating away from RZ modulation formats due to their increased modulation complexity and bandwidth requirements when compared to NRZ signals which

further reduce the practical application of this system. Finally requiring four SOAs will be relatively power hungry as each SOA will draw ~300 mA.

The phase discriminator discussed in Chapter 5 requires a four tooth comb perfectly aligned to the optical carrier frequency of the QPSK signal. If this is not achieved the multiple idlers produced due to FWM will not be at the same frequencies and consequently not interfere correctly. A carrier recovery scheme would be required in conjunction with a local comb generator to produce the four tooth comb with perfect frequency spacing around the QPSK signal under test. This limits any practical implementations of this scheme in an optical network.

The clock recovery scheme demonstrated in Chapter 6, however, is relatively simple to implement making it a viable clock recovery option for BPSK all-optical superchannels. It only requires two active components; a SOA and a CW laser making it easy to integrate and could easily be implemented alongside the tradition coherent receiver or as a standalone clock recovery unit. The greatest area of interest for this technique, in the author's opinion, is in the optical nodes where coherent receivers with digital signal processing (DSP) can be prohibitively expensive. This clock recovery scheme has very few drawbacks preventing it being implemented in a real world optical network.

7.2 Power Consumption

SMF has a much larger bandwidth than any conceivable electronic device and a much greater bandwidth than any optical-to-electronic converter (O/E) or electronic-to-optical (E/O) converter required to interface between the optical and electronic domains. This has created an "electronic bottleneck" where the electronic equipment is limiting the available bitrate of the optical signal [58]. From this perspective, nonlinear all-optical devices look attractive as they don't have the bandwidth limitations of electronics, and can operate at higher bitrates. Scaling the electronic devices to work at higher bitrates is expensive and power consuming and schemes such as wavelength division multiplexing (WDM) and OFDM are often used to overcome these limitations by creating multiple channels each of which is modulated with a relatively low bitrate (<40

Gbaud [77]), well within the capabilities of modern electronic devices. This parallelises the processing in the electronic domain, easing the computation requirements of each component but requires more devices. Increasing the number of parallel devices will increase the power consumption even though the "electronic bottleneck" has been mitigated.

Power consumption is a crucial cost when designing any optical network and is an important factor to consider when comparing optical and electronic signal processing techniques. Tucker *et. al* [76] performed a detailed investigation into the trade-off between optical and electronic processing particularly looking at the power consumption of SOAs and highly nonlinear fibre (HNLF) when compared to complementary metal–oxide–semiconductor (CMOS) circuits. At higher bitrates, it was found that there is an advantage in using optical signal processing techniques as long the application is relatively simple, i.e. only a few operations per bit (number of SOAs) [76]. Both the phase discrimination technique and the clock recovery technique described in this thesis used only one operation (SOA) per bit whereas the modulation conversion required four operations per bit (ignoring linear SOAs).

In conclusion, as bitrates continue to grow due to the increased capacity demand optical signal processing is becoming an increasingly attractive choice for simple applications such as wavelength conversion, modulation conversion, and clock recovery. The all-optical techniques demonstrated in this thesis are proof-of-principles and could easily be scaled to higher bitrates where they may provide some benefits over traditional electronic processing (DSP).

7.3 Future Work

Initial future work could involve performing bit error rate (BER) measurements on both the OOK to AMI/DB modulation conversion technique and the phase sensitive frequency conversion technique to provide a better indication of the performance on these systems. By performing BER measurement on both the input and output signals of a system and comparing, the number of errors a system introduces can be measured. As mentioned previously, both systems have issues preventing BER measurements from being performed. In the case of

the OOK to AMI/DB modulation conversion, the clocked laser source needs to be changed for a device that does not have an error floor. The phase sensitive frequency conversion scheme requires a more complex solution, as a method of tracking the QPSK signal carrier phase with respect to the four pumps is required. A simple method of tracking the carrier phase has been achieved for BPSK modulation formats and this technique should be applicable for QPSK data as well [122].

Other possible future work includes using these all-optical techniques for higher order modulation formats, in particular QAM for the phase sensitive frequency conversion technique and QPSK/QAM for the clock recovery technique. Optical networks are continuously moving to higher order modulation formats to increase their spectral efficiency and these all-optical techniques will only remain useful if they can process such modulation formats.

A technique to recover the original carrier frequency from phase modulated superchannels would be an excellent continuation of the work covered in Chapter 6. By recovering the carrier as well as the clock, the original comb source of the OFDM superchannel could be reproduced. This would be extremely useful for optical networks particularly in the optical nodes where optical channels are add/dropped or re-routed down different optical paths.

8.

Appendix

8.1 Numerical Model of the SOA

The numerical model used to obtain the simulation results presented in this thesis was developed by Dr. Roderick Webb and is based on a time-domain model similar to those widely used to model cross-phase and cross-gain modulation in SOAs [70, 123-125]. With the semiconductor optical amplifier (SOA) divided into a number of length elements, rate equations for the carrier density and carrier temperature were solved and a polynomial approximation to the gain spectrum was evaluated for each length element and time step. In order to model the nonlinear mixing between inputs which is of interest here, the input fields were summed and represented by a single equivalent-baseband optical field:

$$E_{in} = \sum_k E_k(t) \exp i(\omega_k - \omega_c)t \tag{8-1}$$

where the E_k are the complex amplitudes and the ω_k are the frequencies of the component fields, and ω_c is a common carrier frequency. The mixing products generated by the nonlinear response of the SOA are obtained by taking the Fourier transform of the output field.

The growth in forward travelling optical power, P ($P = EE^*/2$), is given by:

$$\frac{\delta P}{\delta z} + \frac{\delta P}{v_g \delta t} = (\Gamma g_m - \alpha_L)P \tag{8-2}$$

where v_g is the group velocity, Γ is the proportion of the power in the active region and α_L is the waveguide loss (measured with the net material gain set to zero). g_m is the material gain, which varies with time, t, and position, z, and depends on wavelength, λ, according to:

$$g_m = g_p \left[3 \left(\frac{\lambda_z - \lambda}{\lambda_z - \lambda_p} \right)^2 - 2 \left(\frac{\lambda_z - \lambda}{\lambda_z - \lambda_p} \right)^3 \right] \qquad (8\text{-}3)$$

where λ_z is the band gap wavelength. In a simplification of the expression introduced by Leuthold et al. [71], λ_z is assumed to be constant to facilitate calculation of concatenated gain spectra and the amplified spontaneous emission (ASE). (In this work, the effects of ASE were negligible.) g_p and λ_p are the gain and wavelength at the peak of the gain spectrum, given by:

$$g_p = a_0 \left(N_{eff} - N_0 \right) \qquad (8\text{-}4)$$

and

$$\lambda_p = \lambda_0 - b_0 \left(N_{eff} - N_0 \right) - b_1 \left(N_{eff} - N_0 \right)^2 \qquad (8\text{-}5)$$

where a_0 is the differential gain, N_0 is the transparency carrier density and λ_0, b_0 and b_1 are constants.

Band modelling has shown that the effects of carrier heating in the centre of the gain region can be approximated by a reduction in carrier density to an effective density, N_{eff}, given by:

$$N_{eff} = N - \frac{\delta N_{eff}}{\delta T} (T - T_0) \qquad (8\text{-}6)$$

where T is the temperature of the conduction band carriers and T_0 is the carrier temperature in the absence of optical power. The actual carrier density, N, evolves according to the standard rate equation:

$$\frac{\delta N}{\delta t} = I_e - a_s N - b_s N^2 - c_s N^3 - \frac{g_m \Gamma P}{A \hbar \omega} \qquad (8\text{-}7)$$

where I_e is the electron injection rate per unit volume; a_s, b_s and c_s are the spontaneous recombination coefficients; A is the cross-sectional area of the active region and $\hbar \omega$ is the photon energy.

T is assumed to rise in proportion to the number of carriers removed by stimulated recombination and to decay exponentially:

$$\frac{\delta T}{\delta t} = \frac{\varepsilon_T g_m \Gamma P}{\sqrt{N} A \hbar \omega} - \frac{T - T_0}{\tau_{CH}} \qquad (8\text{-}8)$$

where ε_T is a constant and τ_{CH} is the cooling time constant. The $\sqrt{N}$ term is introduced as an approximation to band modelling results.

The rate equations are solved using uniform length elements and time steps, with the interval between time samples equal to the optical transit time of a length element. When modelling nonlinear mixing, step sizes must be chosen that are short enough to sample all the important beat frequencies in the optical field. The phase changes induced on the optical field are related to the carrier density and temperature by:

$$\frac{\delta \phi}{\delta z} + \frac{\delta \phi}{v_g \delta t} = \frac{\Gamma a_0}{2} \left[(N - N_0) \alpha_{BF} - (T - T_0) \frac{\delta N_{eff}}{\delta T} \alpha_{CH} \right]$$

where α_{BF} and α_{CH} are the alpha factors for the band filling and carrier heating processes, respectively [105, 126].

The unknown model parameters were obtained by comparing the outputs with experimental data from a CIP XN-OEC-1550, a SOA similar to the one used in this work. All measurements were made at the same bias current in order to avoid changes in junction temperature, which is not included in this model. Accurate fits were obtained both to a set of gain and ASE spectra measured with the device saturated by different levels of continuous-wave (CW) optical power and also to a set of pump-probe amplitude and phase responses measured in the region of the gain peak. The values for a, α_{BF}, ε_T, τ_{CH} and α_{CH} were further optimised to improve the fit to the experimental results presented in Fig. 5.2. Results for difference frequencies above 700GHz were not included because the measured and modelled slopes diverged significantly in this region. The final set of parameter values used for the simulations in Section 5.4 is shown in **Table 8.1**.

Table 8.1 - SOA model parameters.

Bias current	I	400mA
Active area	A	1.95e-13 m^2
Effective length	L	2.2 mm
Transparency density	N_0	5.34e23 m^{-3}
Defect recombination coefficient	a_s	2.15e8 s^{-1}
Radiative recombination coefficient	b_s	1.98e-16 m^{3}s^{-1}
Auger recombination coefficient	c_s	6.34e-40 m^{6}s^{-1}
Gain coefficient	a	4.56e-20 m^{-2}
Waveguide loss	α_L	2.26e3 m^{-1}
Band filling alpha factor	α_{BF}	6.03
Carrier heating alpha factor	α_{CH}	2.26
Carrier heating parameter	ε_T	1.33e-9 m$^{3/2}$K
Carrier cooling time constant	τ_{CH}	8.76e-13 s
Effective density change/degree	$\partial N_{eff} / \partial T$	3.30e21 m^{-3}K^{-1}
Confinement factor	Γ	0.18
Reference wavelength	λ_0	1638 nm
Bandgap wavelength	λ_z	1709 nm
Gain spectrum parameter	b_0	7.56e-32 m^4
Gain spectrum parameter	b_1	1.23e-58 m^7

8.2 De Bruijn Pattern for All-Optical Clock Recovery

In optical communication networks, long random bit streams containing the real data are uncorrelated. When the optical orthogonal frequency division multiplexed (OFDM) superchannel is modulated with a carrier-suppressed modulation format, such as binary phase shift keying (BPSK), the mean product of the two filtered waveforms, injected into the SOA, will be zero and no nonlinear mixing term that depends on that product will be generated. However, the nonlinear mixing between the CW pump and the BPSK signals will still produce the modulation stripped idlers required for clock recovery. Only nonlinear mixing due to the product of the BPSK waveforms is suppressed. The finite-length repeated patterns used for simulation or experiment must be chosen carefully to avoid generating spurious mixing terms that are data-dependent and would not appear in a system carrying real data.

8. Appendix
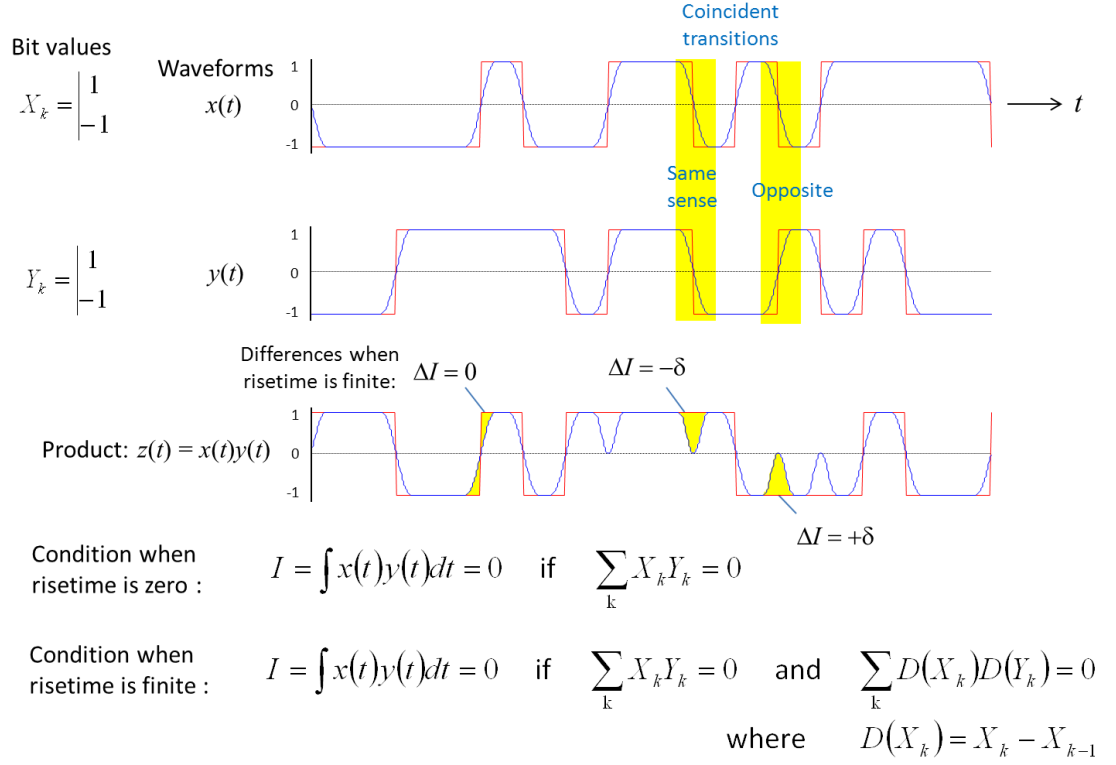
Fig. 8.1 – Bit transitions, k = bit number.

Consider the two phase modulated waveforms, x(t) and y(t) shown in Fig. 8.1, which have the same clock phase. If the transitions are instantaneous (red trace), the waveforms will be uncorrelated as long as the two bit sequences are uncorrelated. However, if the transition times are finite, then the integral of the product of the waveforms is reduced wherever there are simultaneous transitions in the same sense and increased where they are in the opposite sense. This means that the transitions, or bit-difference sequences, must also be uncorrelated for the waveforms to remain uncorrelated.

This means that to ensure no nonlinear mixing term is produced from two BPSK modulated waveforms injected into the SOA; the bit values must be uncorrelated:

$$\sum_k X_k Y_k = 0 \tag{8-9}$$

and also the bit transitions must be uncorrelated:

$$\sum_k D(X_k)D(Y_k) = 0 \tag{8-10}$$

Two copies of the same pseudo-random binary sequence (PRBS) with a relative delay greater than one bit period have perfectly decorrelated transitions. However, a PRBS pattern has an odd number of bits (2^n-1), so if used for BPSK modulation with exactly equal amplitudes, precise carrier suppression is not possible. Consequently, two waveforms modulated by copies of the same PRBS with a relative delay cannot be perfectly decorrelated. This is more significant with short patterns, such as PRBS 2^7-1. Experimentally implementing a long PRBS pattern (2^{31}-1) to reduce this effect was relatively easy, however, simulating long PRBS patterns is computationally intensive and limited the pattern lengths that could be used.

A De Bruijn pattern (DBS) has an extra zero (pattern length 2^n) to obtain parity meaning that when BPSK modulation is used, precise carrier suppression is achievable and perfect bit decorrelation can be obtained between two DBS modulated waveforms. Two DBS modulated waveforms can also achieve uncorrelated transitions for certain relative delays up to n-1 bits and some other delay values. As a result DBS was the pattern of choice for the all-optical clock recovery simulations where, short patterns (2^{10}) were required to reduce the computation complexity and consequently the simulation run time. Experimentally, PRBS patterns were still used since the pattern generators were unable to produce DBS, however, the long pattern lengths (2^{31}-1) reduced the production of any spurious nonlinear mixing terms.

List of References

1. G. P. Agrawal, *Fiber-optic communication systems* (John Wiley & Sons, 2010), Vol. 222.
2. R. J. Mears, L. Reekie, I. M. Jauncey, and D. N. Payne, "Low-noise erbium-doped fibre amplifier operating at 1.54μm" in *Electronics Letters,* (Institution of Engineering and Technology, 1987), pp. 1026-1028.
3. C. E. Shannon, "A mathematical theory of communication" ACM SIGMOBILE Mobile Computing and Communications Review **5**, 3-55 (2001).
4. D. Hillerkuss, R. Schmogrow, T. Schellinger, M. Jordan, M. Winter, G. Huber, T. Vallaitis, R. Bonk, P. Kleinow, and F. Frey, "26 Tbit s-1 line-rate super-channel transmission utilizing all-optical fast Fourier transform processing" Nature Photonics **5**, 364-371 (2011).
5. Cisco, "Global Devices and Connections Growth, http://www.cisco.com/c/en/us/solutions/collateral/service-provider/visual-networking-index-vni/VNI_Hyperconnectivity_WP.html" (2014).
6. A. H. Gnauck and P. J. Winzer, "Optical phase-shift-keyed transmission" Journal of Lightwave Technology **23**, 115 (2005).
7. A. Chiba, T. Sakamoto, T. Kawanishi, K. Higuma, M. Sudo, and J. Ichikawa, "16-level quadrature amplitude modulation by monolithic quad-parallel Mach-Zehnder optical modulator" Electronics Letters **46**, 220-222 (2010).
8. P. J. Winzer and R. J. Essiambre, "Advanced modulation formats for high-capacity optical transport networks" J. Lightwave Technol. **24**, 4711-4728 (2006).
9. S. Michel, "Why complex modulation optical signals?, http://www.lightwaveonline.com/articles/print/volume-30/issue-4/feature/why-complex-modulated-optical-signals.html" (2013).
10. Transmode.com, "Optics and communications, http://www.transmode.com/sv/technologies/wdm-the-transmode-way/wdm-the-transmode-way-html/1-optics-and-communications".
11. J. M. Dailey, M. J. Power, R. P. Webb, and R. J. Manning, "All-optical modulation converter for on-off keying to duobinary and alternate-mark inversion at 42.6 Gbps" in *The European Conference on Lasers and Electro-Optics*, (Optical Society of America, 2011),
12. J. M. Dailey, M. J. Power, R. P. Webb, and R. J. Manning, "High-bandwidth generation of duobinary and alternate-mark-inversion modulation formats using SOA-based signal processing" Opt. Express **19**, 25954-25968 (2011).
13. R. P. Webb, J. M. Dailey, R. J. Manning, and A. D. Ellis, "Phase discrimination and simultaneous frequency conversion of the orthogonal components of an optical signal by four-wave mixing in an SOA" Opt. Express **19**, 20015-20022 (2011).
14. M. J. Power, R. P. Webb, and R. J. Manning, "All-optical phase discrimination using SOA" Opt. Express **21**, 25664-25669 (2013).
15. M. Power, W. Jia, R. P. Webb, R. J. Manning, and F. C. Garcia Gunning, "Clock Recovery of Phase Modulated Optical OFDM Superchannel" in *Optical Fiber Communication Conference*, OSA Technical Digest (online) (Optical Society of America, 2014), W3F.1.
16. M. J. Power, W. Jia, R. P. Webb, R. J. Manning, and F. C. G. Gunning, "Four-wave mixing for clock recovery of phase modulated optical OFDM superchannel" Opt. Express **22**, 7007-7013 (2014).
17. http://wikipremed.com/, "http://wikipremed.com/01physicscards600/405a.gif".
18. W. Shieh and C. Athaudage, "Coherent optical orthogonal frequency division multiplexing" Electronics Letters **42**, 587-589 (2006).
19. X. Liu, "Nonlinear effects in phase shift keyed transmission" in *Optical Fiber Communication Conference*, (Optical Society of America, 2004), ThM4.
20. C. Xu, L. Xiang, and W. Xing, "Differential phase-shift keying for high spectral efficiency optical transmissions" Selected Topics in Quantum Electronics, IEEE Journal of **10**, 281-293 (2004).

List of References

21. D. Ly-Gagnon, S. Tsukamoto, K. Katoh, and K. Kikuchi, "Coherent detection of optical quadrature phase-shift keying signals with carrier phase estimation" Lightwave Technology, Journal of **24**, 12-21 (2006).
22. G. Jacobsen, *Noise in digital optical transmission systems* (Artech House Boston, MA, 1994).
23. P. A. Humblet and M. Azizoglu, "On the bit error rate of lightwave systems with optical amplifiers" Lightwave Technology, Journal of **9**, 1576-1582 (1991).
24. A. Gnauck, S. Chandrasekhar, J. Leuthold, and L. Stulz, "Demonstration of 42.7-Gb/s DPSK receiver with 45 photons/bit sensitivity" Photonics Technology Letters, IEEE **15**, 99-101 (2003).
25. S. Tsukamoto, K. Katoh, and K. Kikuchi, "Coherent demodulation of optical multilevel phase-shift-keying signals using homodyne detection and digital signal processing" Photonics Technology Letters, IEEE **18**, 1131-1133 (2006).
26. M. J. Connelly, *Semiconductor Optical Amplifiers,* 1st ed. (Springer, Boston, 2002), p. 184.
27. C. Zah, J. Osinski, C. Caneau, S. Menocal, L. Reith, J. Salzman, F. Shokoohi, and T. Lee, "Fabrication and performance of 1.5μm GaInAsP travelling-wave laser amplifiers with angled facets" Electronics Letters **23**, 990-992 (1987).
28. C. Vassallo, "Polarisation-independent antireflection coatings for semiconductor optical amplifiers" Electronics Letters **24**, 61-62 (1988).
29. H. Ju, S. Zhang, D. Lenstra, H. De Waardt, E. Tangdiongga, G. Khoe, and H. Dorren, "SOA-based all-optical switch with subpicosecond full recovery" Opt. Express **13**, 942-947 (2005).
30. S. Diez, R. Ludwig, and H. Weber, "All-optical switch for TDM and WDM/TDM systems demonstrated in a 640 Gbit/s demultiplexing experiment" Electronics Letters **34**, 803-805 (1998).
31. M. Osinski and J. Buus, "Linewidth broadening factor in semiconductor lasers--An overview" Quantum Electronics, IEEE Journal of **23**, 9-29 (1987).
32. C. H. Henry, "Theory of the linewidth of semiconductor lasers" Quantum Electronics, IEEE Journal of **18**, 259-264 (1982).
33. S. Diez, C. Schmidt, R. Ludwig, H. G. Weber, K. Obermann, S. Kindt, I. Koltchanov, and K. Petermann, "Four-wave mixing in semiconductor optical amplifiers for frequency conversion and fast optical switching" Selected Topics in Quantum Electronics, IEEE Journal of **3**, 1131-1145 (1997).
34. W. Mathlouthi, F. Vacondio, P. Lemieux, and L. A. Rusch, "SOA gain recovery wavelength dependence: simulation and measurement using a single-color pump-probe technique" Opt. Express **16**, 20656-20665 (2008).
35. L. Occhi, Y. Ito, H. Kawaguchi, L. Schares, J. Eckner, and G. Guekos, "Intraband gain dynamics in bulk semiconductor optical amplifiers: measurements and simulations" Quantum Electronics, IEEE Journal of **38**, 54-60 (2002).
36. C. S. Cleary, M. J. Power, S. Schneider, R. P. Webb, and R. J. Manning, "Fast gain recovery rates with strong wavelength dependence in a non-linear SOA" Opt. Express **18**, 25726-25737 (2010).
37. P. G. Robin, J. M. Robert, and C. David, "Recovery Dynamics of the 'Turbo-Switch'" in OSA Technical Digest Series(CD) (Optical Society of America, 2006), OTuC2.
38. Z. Zheng, L. An, Z. Li, X. Zhao, and X. Liu, "All-optical regeneration of DQPSK/QPSK signals based on phase-sensitive amplification" Optics Communications **281**, 2755-2759 (2008).
39. K. A. Croussore and L. Guifang, "Phase-Regenerative Wavelength Conversion for BPSK and DPSK Signals" Photonics Technology Letters, IEEE **21**, 70-72 (2009).
40. R. P. Webb and T. G. Hodgkinson, "Experimental confirmation of laser amplifier intermodulation model" in *Electronics Letters,* (Institution of Engineering and Technology, 1989), pp. 491-493.
41. T. Healy, F. C. Garcia Gunning, A. D. Ellis, and J. D. Bull, "Multi-wavelength source using low drive-voltage amplitude modulators for optical communications" Opt. Express **15**, 2981-2986 (2007).
42. wikipedia, "http://en.wikipedia.org/wiki/File:Singlemode_fibre_structure.svg".
43. Cisco, "http://www.cisco.com/c/en/us/products/collateral/interfaces-modules/transceiver-modules/white_paper_c11-463661.html".
44. D. Cotter, R. Manning, K. Blow, A. Ellis, A. Kelly, D. Nesset, I. Phillips, A. Poustie, and D. Rogers, "Nonlinear optics for high-speed digital information processing" Science **286**, 1523-1528 (1999).

45. W. Mathlouthi, F. Vacondio, P. Lemieux, and L. A. Rusch, "SOA gain recovery wavelength dependence: simulation and measurement using a single-color pump-probe technique" Opt. Express **16**, 20656-20665 (2008).
46. R. Giller, R. J. Manning, and D. Cotter, "Gain and phase recovery of optically excited semiconductor optical amplifiers" IEEE Photon. Technol. Lett. **18**, 1061-1063 (2006).
47. F. Girardin, G. Guekos, and A. Houbavlis, "Gain recovery of bulk semiconductor optical amplifiers" IEEE Photon. Technol. Lett. **10**, 784-786 (1998).
48. R. Gutiérrez-Castrejón, L. Schares, L. Occhi, and G. Guekos, "Modeling and measurement of longitudinal gain dynamics in saturated semiconductor optical amplifiers of different length" Quantum Electronics, IEEE Journal of **36**, 1476-1484 (2000).
49. L. Schares, C. Schubert, C. Schmidt, H. G. Weber, L. Occhi, and G. Guekos, "Phase dynamics of semiconductor optical amplifiers at 10-40 GHz" Quantum Electronics, IEEE Journal of **39**, 1394-1408 (2003).
50. A. Uskov, J. Mork, and J. Mark, "Theory of short-pulse gain saturation in semiconductor laser amplifiers" IEEE Photon. Technol. Lett. **4**, 443-446 (1992).
51. R. P. Giller, R. J. Manning, and D. Cotter, "Recovery Dynamics of the'Turbo-Switch'" in *Optical Amplifiers and Their Applications*, (Optical Society of America, 2006),
52. J. Leuthold, R. Ryf, D. N. Maywar, S. Cabot, J. Jaques, and S. Patel, "Nonblocking all-optical cross connect based on regenerative all-optical wavelength converter in a transparent demonstration over 42 nodes and 16800 km" J. Lightwave Technol. **21**, 2863 (2003).
53. R. Manning and D. Davies, "Three-wavelength device for all-optical signal processing" Optics letters **19**, 889-991 (1994).
54. R. J. Runser, D. Zhou, C. Coldwell, B. C. Wang, P. Toliver, K.-L. Deng, I. Glesk, and P. R. Prucnal, "Interferometric ultrafast SOA-based optical switches: From devices to applications" Optical and quantum electronics **33**, 841-874 (2001).
55. J. Sokoloff, P. Prucnal, I. Glesk, and M. Kane, "A terahertz optical asymmetric demultiplexer (TOAD)" IEEE Photon. Technol. Lett. **5**, 787-790 (1993).
56. G. Talli and M. Adams, "Gain recovery acceleration in semiconductor optical amplifiers employing a holding beam" Optics communications **245**, 363-370 (2005).
57. H.-Y. Yu, D. Mahgereftheh, P. S. Cho, and J. Goldhar, "Optimization of the frequency response of a semiconductor optical amplifier wavelength converter using a fiber Bragg grating" J. Lightwave Technol. **17**, 308 (1999).
58. K. E. Stubkjaer, "Semiconductor optical amplifier-based all-optical gates for high-speed optical processing" Selected Topics in Quantum Electronics, IEEE Journal of **6**, 1428-1435 (2000).
59. J. M. Wiesenfeld, B. Glance, J. Perino, and A. Gnauck, "Wavelength conversion at 10 Gb/s using a semiconductor optical amplifier" IEEE Photon. Technol. Lett. **5**, 1300-1303 (1993).
60. R. Manning, D. Davies, S. Cotter, and J. Lucek, "Enhanced recovery rates in semiconductor laser amplifiers using optical pumping" Electronics Letters **30**, 787-788 (1994).
61. R. J. Manning, X. Yang, R. P. Webb, R. Giller, F. C. Garcia Gunning, and A. D. Ellis, "The turbo-switch-a novel technique to increase the high-speed response of SOAs for wavelength conversion" in *Optical Fiber Communication Conference, 2006 and the 2006 National Fiber Optic Engineers Conference. OFC 2006*, (IEEE, 2006), 3 pp.
62. K. Kang, T. Chang, I. Glesk, and P. Prucnal, "Comparison of Sagnac and Mach-Zehnder ultrafast all-optical interferometric switches based on a semiconductor resonant optical nonlinearity" Applied Optics **35**, 417-426 (1996).
63. D.-H. Kim and J. Kang, "Sagnac loop interferometer based on polarization maintaining photonic crystal fiber with reduced temperature sensitivity" Opt. Express **12**, 4490-4495 (2004).
64. N. S. Patel, K. L. Hall, and K. A. Rauschenbach, "Interferometric all-optical switches for ultrafast signal processing" Applied Optics **37**, 2831-2842 (1998).
65. K. Hall, J. Mark, E. Ippen, and G. Eisenstein, "Femtosecond gain dynamics in InGaAsP optical amplifiers" Applied physics letters **56**, 1740-1742 (1990).
66. J. Mark and J. Mørk, "Subpicosecond gain dynamics in InGaAsP optical amplifiers: Experiment and theory" Applied physics letters **61**, 2281-2283 (1992).
67. M. Eiselt, W. Pieper, and H. G. Weber, "SLALOM: Semiconductor laser amplifier in a loop mirror" J. Lightwave Technol. **13**, 2099-2112 (1995).

68. J. Dong, X. Zhang, J. Xu, and D. Huang, "Filter-free ultrawideband generation based on semiconductor optical amplifier nonlinearities" Optics communications **281**, 808-813 (2008).
69. G. Talli and M. Adams, "Gain dynamics of semiconductor optical amplifiers and three-wavelength devices" Quantum Electronics, IEEE Journal of **39**, 1305-1313 (2003).
70. G. Talli and M. Adams, "Amplified spontaneous emission in semiconductor optical amplifiers: modelling and experiments" Optics communications **218**, 161-166 (2003).
71. J. Leuthold, M. Mayer, J. Eckner, G. Guekos, H. Melchior, and C. Zellweger, "Material gain of bulk 1.55 μm InGaAsP/InP semiconductor optical amplifiers approximated by a polynomial model" Journal of Applied Physics **87**, 618-620 (2000).
72. A. Gnauck, X. Liu, X. Wei, D. Gill, and E. Burrows, "Comparison of modulation formats for 42.7-Gb/s single-channel transmission through 1980 km of SSMF" IEEE Photon. Technol. Lett. **16**, 909-911 (2004).
73. P. J. Winzer, A. H. Gnauck, G. Raybon, S. Chandrasekhar, Y. Su, and J. Leuthold, "40-Gb/s return-to-zero alternate-mark-inversion (RZ-AMI) transmission over 2000 km" IEEE Photon. Technol. Lett. **15**, 766-768 (2003).
74. K. Cheng and J. Conradi, "Reduction of pulse-to-pulse interaction using alternative RZ formats in 40-Gb/s systems" IEEE Photon. Technol. Lett. **14**, 98-100 (2002).
75. A. Price and N. Le Mercier, "Reduced bandwidth optical digital intensity modulation with improved chromatic dispersion tolerance" Electronics Letters **31**, 58-59 (1995).
76. R. Tucker, K. Hinton, and G. Raskutti, "Energy consumption limits in high-speed optical and electronic signal processing" Electronics Letters **43**, 906-908 (2007).
77. I. Kang, M. S. Rasras, L. L. Buhl, M. Dinu, G. Raybon, S. Cabot, M. A. Cappuzzo, L. Gomez, Y. Chen, and S. S. Patel, "High-speed all-optical generation of advanced modulation formats using photonic-integrated all-optical format converter" Selected Topics in Quantum Electronics, IEEE Journal of **18**, 765-771 (2012).
78. P. J. Winzer and J. Leuthold, "Return-to-zero modulator using a single NRZ drive signal and an optical delay interferometer" IEEE Photon. Technol. Lett. **13**, 1298-1300 (2001).
79. O. Leclerc, B. Lavigne, E. Balmefrezol, P. Brindel, L. Pierre, D. Rouvillain, and F. Seguineau, "Optical Regeneration at 40 Gb/s and Beyond" J. Lightwave Technol. **21**, 2779 (2003).
80. J. F. Hayes and S. B. Weinstein, *Data communications principles* (Springer, 1992).
81. E. Jahn, N. Agrawal, M. Arbert, H.-J. Ehrke, D. Franke, R. Ludwig, W. Pieper, H. Weber, and C. Weinert, "40 Gbit/s all-optical demultiplexing using a monolithically integrated Mach-Zehnder interferometer with semiconductor laser amplifiers" Electronics Letters **31**, 1857-1858 (1995).
82. J. M. Dailey, R. P. Webb, and R. J. Manning, "All-optical technique for modulation format conversion from on-off-keying to alternate-mark-inversion" (2010).
83. R. P. Webb, J. M. Dailey, and R. J. Manning, "Pattern compensation in SOA-based gates" (2010).
84. X. Qianfan, Y. Minyu, D. Yi, C. Wenshan, and Z. Jianfeng, "Experimental demonstration of pattern effect compensation using an asymmetrical Mach-Zehnder interferometer with SOAs" Photonics Technology Letters, IEEE **13**, 1325-1327 (2001).
85. L. Billes, J. Simon, B. Kowalski, M. Henry, G. Michaud, P. Lamouler, and F. Alard, "20 Gbit/s optical 3R regenerator using SOA based Mach-Zehnder interferometer gate" in *Integrated Optics and Optical Fibre Communications, 11th International Conference on, and 23rd European Conference on Optical Communications (Conf. Publ. No.: 448)*, (IET, 1997), 269-272.
86. J. M. Dailey and T. L. Koch, "Simple rules for optimizing asymmetries in SOA-based Mach–Zehnder wavelength converters" J. Lightwave Technol. **27**, 1480-1488 (2009).
87. W. Kaiser, T. Wuth, M. Wichers, and W. Rosenkranz, "Reduced complexity optical duobinary 10-Gb/s transmitter setup resulting in an increased transmission distance" IEEE Photonics Technology Letters **13**, 884-886 (2001).
88. T. Durhuus, B. Mikkelsen, C. Joergensen, S. Lykke Danielsen, and K. E. Stubkjaer, "All-optical wavelength conversion by semiconductor optical amplifiers" J. Lightwave Technol. **14**, 942-954 (1996).
89. G. P. Agrawal, "Optical Communication Systems (OPT428)" (2007), retrieved http://www.optics.rochester.edu/users/gpa/opt428c.pdf.
90. G. Contestabile, A. Maruta, and K. Kitayama, "Gain dynamics in quantum-dot semiconductor optical amplifiers at 1550 nm" IEEE Photon. Technol. Lett. **22**, 987-989 (2010).

91. Y. Liu, E. Tangdiongga, Z. Li, H. de Waardt, A. Koonen, G. Khoe, X. Shu, I. Bennion, and H. Dorren, "Error-free 320-Gb/s all-optical wavelength conversion using a single semiconductor optical amplifier" J. Lightwave Technol. **25**, 103-108 (2007).

92. M. Nielsen, "Bandwidth enhancement of SOA-based switches using optical filtering: theory and experimental verification" Opt. Express **14**, 1260-1265 (2006).

93. R. P. Webb, M. Power, and R. J. Manning, "Phase-sensitive frequency conversion of quadrature modulated signals" Opt. Express **21**, 12713-12727 (2013).

94. W. Imajuku, A. Takada, and Y. Yamabayashi, "Low-noise amplification under the 3 dB noise figure in high-gain phase-sensitive fibre amplifier" Electronics Letters **35**, 1954-1955 (1999).

95. R. Tang, J. Lasri, P. S. Devgan, V. Grigoryan, P. Kumar, and M. Vasilyev, "Gain characteristics of a frequency nondegenerate phase-sensitive fiber-optic parametric amplifier with phase self-stabilized input" Opt. Express **13**, 10483-10493 (2005).

96. Y. Leng, C. J. K. Richardson, and J. Goldhar, "Phase-sensitive amplification using gain saturation in a nonlinear Sagnac interferometer" Opt. Express **16**, 21446-21455 (2008).

97. R. Slavik, F. Parmigiani, J. Kakande, C. Lundstrom, M. Sjodin, P. A. Andrekson, R. Weerasuriya, S. Sygletos, A. D. Ellis, L. Gruner-Nielsen, D. Jakobsen, S. Herstrom, R. Phelan, J. O'Gorman, A. Bogris, D. Syvridis, S. Dasgupta, P. Petropoulos, and D. J. Richardson, "All-optical phase and amplitude regenerator for next-generation telecommunications systems" Nat Photon **4**, 690-695 (2010).

98. J. Kakande, A. Bogris, R. Slavik, F. Parmigiani, D. Syvridis, P. Petropoulos, D. Richardson, M. Westlund, and M. Sköld, "QPSK Phase and Amplitude Regeneration at 56 Gbaud in a Novel Idler-Free Non-Degenerate Phase Sensitive Amplifier" in OSA Technical Digest (CD) (Optical Society of America, 2011), OMT4.

99. J. Kakande, R. Slavik, F. Parmigiani, A. Bogris, D. Syvridis, L. Gruner-Nielsen, R. Phelan, P. Petropoulos, and D. J. Richardson, "Multilevel quantization of optical phase in a novel coherent parametric mixer architecture" Nat Photon **5**, 748-752 (2011).

100. L. F. Tiemeijer, "Effects of nonlinear gain on four-wave mixing and asymmetric gain saturation in a semiconductor laser amplifier" Applied Physics Letters **59**, 499-501 (1991).

101. K. Kikuchi, M. Kakui, C. E. Zah, and T. P. Lee, "Observation of highly nondegenerate four-wave mixing in 1.5 um traveling-wave semiconductor optical amplifiers and estimation of nonlinear gain coefficient" Quantum Electronics, IEEE Journal of **28**, 151-156 (1992).

102. A. Uskov, J. Mork, J. Mark, M. C. Tatham, and G. Sherlock, "Terahertz four-wave mixing in semiconductor optical amplifiers: Experiment and theory" Applied Physics Letters **65**, 944-946 (1994).

103. R. Weerasuriya, S. Sygletos, S. K. Ibrahim, F. C. G. Gunning, R. J. Manning, R. Phelan, J. O'Carroll, B. Kelly, J. O'Gorman, and A. D. Ellis, "Comparison of Frequency Symmetric Signal Generation From a BPSK Input Using Fiber and Semiconductor-Based Nonlinear Elements" Photonics Technology Letters, IEEE **23**, 651-653 (2011).

104. T. G. Hodgkinson and R. P. Webb, "Application of communications theory to analyse carrier density modulation effects in travelling-wave semiconductor laser amplifiers" Electronics Letters **24**, 1550-1552 (1988).

105. R. Giller, R. J. Manning, and D. Cotter, "Gain and phase recovery of optically excited semiconductor optical amplifiers" Photonics Technology Letters, IEEE **18**, 1061-1063 (2006).

106. G. Maxwell, A. Poustie, C. Ford, M. Harlow, P. Townley, M. Nield, I. Lealman, S. Oliver, L. Rivers, and R. Waller, "Hybrid integration of monolithic semiconductor optical amplifier arrays using passive assembly" in *Electronic Components and Technology Conference, 2005. Proceedings. 55th*, 2005), 1349-1352 Vol. 1342.

107. R. Noé, "Phase Noise-Tolerant Synchronous QPSK/BPSK Baseband-Type Intradyne Receiver Concept With Feedforward Carrier Recovery" J. Lightwave Technol. **23**, 802 (2005).

108. S. Diez, R. Ludwig, E. Patzak, H. G. Weber, G. Eisenstein, and R. Schimpe, "Four-wave mixing in semiconductor laser amplifiers: phase matching in configurations with three input waves" in *Lasers and Electro-Optics, 1996. CLEO '96., Summaries of papers presented at the Conference on*, 1996), 505-506.

109. P. S. Cho, V. S. Grigoryan, Y. A. Godin, A. Salamon, and Y. Achiam, "Transmission of 25-Gb/s RZ-DQPSK signals with 25-GHz channel spacing over 1000 km of SMF-28 fiber" Photonics Technology Letters, IEEE **15**, 473-475 (2003).

110. H. J. Lee, H. G. Kim, J. Y. Choi, and H. K. Lee, "All-optical clock recovery from NRZ data with simple NRZ-to-PRZ converter based on self-phase modulation of semiconductor optical amplifier" Electronics Letters **35**, 989-990 (1999).

111. M. Yao, H. Tang, M. Fukazawa, J. Zhou, K. Vahala, M. Newkirk, and B. Miller, "All-optical clock recovery from NRZ data using a nonlinear loop clock generator" in *Optical Fiber Communications, 1996. OFC'96*, (IEEE, 1996), 177-178.

112. H. Lee, J. Ahn, M.-Y. Jeon, K. Kim, D. Lim, and C.-H. Lee, "All-optical clock recovery from NRZ data of 10 Gb/s" IEEE Photon. Technol. Lett. **11**, 730-732 (1999).

113. H. Kurita, T. Shimizu, and H. Yokoyama, "All-optical clock extraction at bit rates up to 80 Gbit/s with monolithic modeIocked laser diodes" in *Lasers and Electro-Optics, 1997. CLEO'97., Summaries of Papers Presented at the Conference on*, (IEEE, 1997), 96-96.

114. C. Kim, I. Kim, X. Li, and G. Li, "All-optical clock recovery of NRZ data at 40 Gbit/s using Fabry-Perot filter and two-section gain-coupled DFB laser" Electronics Letters **39**, 1456-1458 (2003).

115. O. Kamatani and S. Kawanishi, "Ultrahigh-speed clock recovery with phase lock loop based on four-wave mixing in a traveling-wave laser diode amplifier" J. Lightwave Technol. **14**, 1757-1767 (1996).

116. Y.-K. Huang, E. Ip, Z. Wang, M.-F. Huang, Y. Shao, and T. Wang, "Transmission of spectral efficient super-channels using all-optical OFDM and digital coherent receiver technologies" Lightwave Technology, Journal of **29**, 3838-3844 (2011).

117. F. G. Gunning, T. Healy, and A. D. Ellis, "Dispersion tolerance of coherent WDM" Photonics Technology Letters, IEEE **18**, 1338-1340 (2006).

118. P. Frascella, S. Sygletos, and A. Ellis, "A Novel Phase Stabilization Scheme for DPSK CoWDM Signals using High Order Four Wave Mixing" in *European Conference and Exposition on Optical Communications*, (Optical Society of America, 2011),

119. P. J. Winzer, "An Opto-Electronic Interferometer and Its Use in Subcarrier Add/Drop Multiplexing" Journal of Lightwave Technology **31**, 1775-1782 (2013).

120. X. Liu, S. Chandrasekhar, X. Chen, P. Winzer, Y. Pan, B. Zhu, T. Taunay, M. Fishteyn, M. Yan, and J. M. Fini, "1.12-Tb/s 32-QAM-OFDM superchannel with 8.6-b/s/Hz intrachannel spectral efficiency and space-division multiplexing with 60-b/s/Hz aggregate spectral efficiency" in *Optical Communication (ECOC), 2011 37th European Conference and Exhibition on*, (IEEE, 2011), 1-3.

121. M. J. Power, W. Jia, R. P. Webb, R. J. Manning, and F. C. Garcia Gunning, "Clock Recovery of Phase Modulated Optical OFDM Superchannel" in *OFC*, 2014),

122. E. Soodi, "Private Communication, 15th October" (2014).

123. G. Talli and M. J. Adams, "Gain dynamics of semiconductor optical amplifiers and three-wavelength devices" Quantum Electronics, IEEE Journal of **39**, 1305-1313 (2003).

124. F. Ginovart, J. Simon, and I. Valiente, "Gain recovery dynamics in semiconductor optical amplifier" Optics communications **199**, 111-115 (2001).

125. G. Toptchiyski, S. Kindt, K. Petermann, E. Hilliger, S. Diez, and H. G. Weber, "Time-Domain Modeling of Semiconductor Optical Amplifiers for OTDM Applications" J. Lightwave Technol. **17**, 2577 (1999).

126. C. Henry, "Theory of the linewidth of semiconductor lasers" Quantum Electronics, IEEE Journal of **18**, 259-264 (1982).

List of Figures

List of Tables

List of Publications

Journal Publications

C. S. Cleary, **M. J. Power**, S. Schneider, R. P. Webb, and R. J. Manning, "Fast gain recovery rates with strong wavelength dependence in a non-linear SOA" Opt. Express **18**, 25726-25737 (2010).

J. M. Dailey, **M. J. Power**, R. P. Webb, and R. J. Manning, "High-bandwidth generation of duobinary and alternate-mark-inversion modulation formats using SOA-based signal processing" Opt. Express **19**, 25954-25968 (2011).

R. P. Webb, **M. Power**, and R. J. Manning, "Phase-sensitive frequency conversion of quadrature modulated signals" Opt. Express **21**, 12713-12727 (2013).

M. J. Power, R. P. Webb, and R. J. Manning, "All-optical phase discrimination using SOA" Opt. Express **21**, 25664-25669 (2013).

M. J. Power, W. Jia, R. P. Webb, R. J. Manning, and F. C. G. Gunning, "Four-wave mixing for clock recovery of phase modulated optical OFDM superchannel", Opt. Express **22**, 7007-7013 (2014).

R. J. Manning, R. P. Webb, F. C. Garcia Gunning, and **M. J. Power**, "SOAs for Phase-Based Optical Signal Processing," in *Photonics Society Summer Topical Meeting Series, 2014 IEEE* (2014), pp. 110-111.

Conference Proceedings

J. M. Dailey, **M. J. Power**, R. P. Webb, and R. J. Manning, "All-optical modulation converter for on-off keying to duobinary and alternate-mark inversion at 42.6 Gbps" in The European Conference on Lasers and Electro-Optics, (Optical Society of America, 2011),

M.J. Power, J.M. Dailey, R.P. Webb, R.J. Manning, "All-Optical Modulation Conversion at 42.6 Gbit/s", Photonics Ireland, (2011)

S. Sygletos, **M. Power**, F. Garcia Gunning, R. Webb, R. Manning, and A. Ellis, "Simultaneous Dual Channel Phase Regeneration in SOAs," in European Conference and Exhibition on Optical Communication, OSA Technical Digest (online) (Optical Society of America, 2012), paper Tu.1.A.2.

M. J. Power, R. P. Webb and R. J. Manning, "All-Optical Phase Discriminator", Photonics Ireland, (2013)

M. Power, W. Jia, R. Webb, R. Manning, and F. Garcia Gunning, "Clock Recovery of Phase Modulated Optical OFDM Superchannel," in Optical Fiber Communication Conference, OSA Technical Digest (online) (Optical Society of America, 2014), paper W3F.1.

Mark J. Power, W. Jia, R. P. Webb, R. J. Manning, and F. C. Garcia Gunning, "Four-wave mixing for clock recovery of phase modulated optical OFDM superchannel", *Opt. Express*, publication pending, 2014.